METHODS FOR IMPROVING STABILITY AND POWER QUALITY IN NETWORKS WITH HIGH LEVELS OF POWER ELECTRONICS

by

Viet Phong Tran

A dissertation submitted to the faculty of
The University of North Carolina at Charlotte
in partial fulfillment of the requirements
for the degree of Doctor of Philosophy in
Electrical Engineering

Charlotte

2011

Approved by:

_____
Dr. Robert Cox

_____
Dr. Yogendra Kakad

_____
Dr. Mehdi Miri

_____
Dr. Gloria Elliott

ABSTRACT

VIET PHONG TRAN. Methods for improving stability and power quality in networks with high levels of power electronics. (Under the direction of DR. ROBERT COX)

Advanced power electronics are essential to the development of fully active electric power systems. There are, however, potential problems that can arise when high levels of power-electronic systems are distributed throughout a network. Most importantly, power electronics can degrade the quality of the power that is delivered by utility companies; furthermore, they can cause instabilities that lead to complete failures. New "smart" power systems are highly dynamic, meaning that a regulated converter thought to be stable under ideal conditions could easily become unstable for reasons well outside of the designer's control.

This thesis addresses the issue of improving power quality in networks with high levels of power electronics. The core concept presented here is an effective on-line approach for the estimation of network impedance, a time-varying quantity that plays a key role in reducing power quality. Real-time information about the network impedance at the Point of Common Coupling (PCC) can produce more stable power converters and pave the way for new measurement techniques that help to monitor power quality. This thesis also examines the application of network impedance measurements for producing model-based adaptive controllers that allow power-electronic systems to remain stable when connected to "non-stiff" networks. This work can be applied in any system that is heavily dependent on power electronics, including terrestrial "Smart Grids," all-electric ships, aircraft, and spacecraft.

DEDICATION

This thesis is dedicated to my Parents.

ACKNOWLEDGMENTS

I would like to express my deepest gratitude to my advisor, Professor Robert Cox, for providing me with interesting research topics and supervising me throughout the duration of this research. Professor Cox is a very gifted and dedicated person, and I always consider myself very fortunate to work under his guidance.

The research has been carried out at the UNCC Laboratory for Energy Efficient Systems, where I have developed friendships and fruitful conversations with my colleagues for many years. I would like to thank Jason Anderson for his technical helps during my research. Also, many thanks to Jason Anderson and Arun Shrestha for their valuable contribution to make this document completed.

I would like to thank other Professors at the Department of Electrical and Computer Engineering, especially Dr. Yogendra Kakad for his thoughtful advice about the research and also about life. I would like to acknowledge and thank Dr. Asis Nasipuri, Ms. Pat Winter and Mr. Eddie Hill for their helps during my graduate study.

The financial support from the Vietnam International Education Development scholarship program is also much appreciated. I must say that without this support, I could never have conducted this work.

Nothing in the life is more precious than one's family. I am grateful to my parents with their lifetime of supports in many different ways. I also thank my siblings, who always love me. Last but not least, I would like to express my gratitude to my loving wife Diep for her encouragement, patience, and sacrifices.

TABLE OF CONTENTS

LIST OF TABLES

LIST OF FIGURES

CHAPTER 1: INTRODUCTION

"To retrofit America for a global economy . . . means updating the way we get our electricity by starting to build a new smart grid that will save us money, protect our power sources from blackout or attack, and deliver clean, alternative forms of energy to every corner of our nation."

- President Barack Obama

Various forces are interacting to produce significant changes in the generation, delivery, and use of electric power. Most importantly, society has become increasingly concerned about the future availability of non-renewable resources, such as coal and petroleum, as well as the deleterious environmental effects that they may cause. Additionally, there is growing concern about the capability of our existing power infrastructure. Many power plants are nearing the end of their design lifetimes, and many transmission lines often operate near their capacity. Furthermore, concerns over global terrorism have led to increased interest in protecting the world's power infrastructure. To meet these challenges, nations throughout the world are looking to new technologies that help to improve and modernize the generation, delivery, and use of electric power. Numerous enabling technologies have been developed, including information technology for real-time monitoring, analysis, and control. Equally as important, however, are power electronic systems that enable several critical functions. Power electronics, for instance, are necessary to interface most distributed renewable sources with the grid. Furthermore, power electronics are now used to optimize power flows throughout the transmission system. These components are known as Flexible AC Transmission Systems (FACTS). Additionally, the need for improved efficiency and advanced functionality has led to a tremendous dependence on loads that contain

sophisticated power electronic interfaces.

Despite the tremendous benefits derived from using power electronics, they can cause problems when deployed in high levels throughout a network. Most importantly, power electronic systems can degrade the quality of the power that is delivered by utility companies. One source of this degradation are the harmonic currents produced by the converters. Power electronics can also cause instabilities that lead to complete component failures. For example, a data server connected via a converter with an active power-factor correcting (PFC) converter can become unstable when connected to an AC system through a real cable with parasitic impedances. Furthermore, new "smart" power grids are highly dynamic, meaning that converters thought to be stable under ideal conditions could easily become unstable as network conditions change. For instance, a sudden change in network impedance resulting from the islanding of a microgrid could potentially cause otherwise stable converters to become unstable. These issues and others must be addressed before making the transition to fully active power systems.

This thesis addresses the issue of improving power quality in networks with high levels of power electronic devices. The core concept presented here is an effective on-line approach for estimating network impedance, a time-varying quantity that plays a key role in reducing power quality. Real-time information about network impedance can help to stabilize the interaction between power converters and the grid. It can also pave the way for new monitoring and measurement techniques. This thesis also examines the application of network impedance measurements in model-based adaptive controllers that provide stability when power electronic systems are connected to "non-stiff" networks. This work can be applied in any system that is heavily dependent on power electronics, including terrestrial "Smart Grids," all-electric ships, aircraft, and spacecraft.

1.1. Applications of Power Electronics in Smart Grids

Advanced power electronics are considered to be essential for the development of fully active electric power systems [3, 4, 5, 6, 7]. Power electronic devices are need to integrate distributed generation resources, to control power flows, and to increase the efficiency and controllability of loads. Such fully active power systems are termed "Smart Grids". This section describes key power electronic applications in these networks. Although the focus here is on terrestrial power systems, it is important to note that similar concepts are also common in vehicles. Further details are provided in a later section.

1.1.1. Power Electronics in Generation

The use of decentralized generation in the form of gas turbines, hydroelectric generators, tidal energy devices, photovoltaic (PV) arrays, and wind farms is expected to increase over the coming decades as concerns grow over fossil fuel consumption and as conventional power plants near the end of their design lifetimes. Power electronic devices are needed to connect these distributed resources into the host grid [8, 9, 10, 11, 12]. Connecting significant non-conventional generation units throughout the grid will have a significant impact on the overall operation of the power system. Intelligent interfaces are required in order to achieve efficient power transfer as well as to maintain grid stability and to protect the distributed generators from disturbances and faults. Depending upon the source and the application, various power electronic circuits may be included in the overall power train. In many applications, for instance, a PV array might include a DC-to-DC converter and a DC-to-AC inverter designed to maximize power transfer. Wind turbines or high-speed gas turbines might include appropriate AC-to-AC converters designed to ensure a proper connection to the 50/60Hz grid. In all cases, the power electronics must provide high quality AC power, with frequency fluctuations limited to ± 1.2Hz and total harmonic distortion (THD) in the voltage limited to less than 5% [13].

1.1.2. Power Electronics for Controlling Power Flow

Power electronic devices are also used to control power flows in the modern grid, and the dependence upon these elements is expected to increase in the coming decades. Several applications can be considered. First, there is a need to address the limited margin between peak generation and peak demand. This issue consistently arises when demand surges during the summer months. The most obvious solution is to build new power plants and transmission infrastructure. The process of authorizing, locating, and constructing new transmission lines, however, is expensive, time-consuming, and fraught with political challenges. Power electronic systems can help in this situation. For example, they can dynamically compensate reactive power flows, thus providing an opportunity to increase real power flows. Such solutions help to increase margins without requiring massive investments in new infrastructure.

Power electronics in control applications are generally known as Flexible AC Transmission Systems (FACTS). Example include active filters that can dynamically compensate for harmonics injected into the system, Unified Power Factor Compensators (UPFCs) that can improve transient stability limits.

Power electronics are also proposed and used to improve High Voltage DC transmission, which is efficient and highly flexible.

1.1.3. Power Electronics for Efficient End-Use Conversion

Power electronics enable loads to become highly controllable and efficient; thus, the use of advanced power electronics is expected to increase significantly in the coming decade. According to research by the Natural Resources Defense Council (NRDC), for instance, the total amount of electricity that flows through power supplies is more than 207 billion kWh/year, or about 6% of the national electric bill. More efficient designs could save an expected 15 to 20% of that energy. The resulting savings of 32 billion kWh/year would

cut the annual national energy bill by $2.5 billion, displace the power output of seven large power plants, and reduce carbon dioxide emissions by more than 24 million tons per year [14].

The national consciousness over energy costs is driving the development of highly efficient end-use energy conversion. Electric motors and lighting, which were once the primary loads connected to the power system, are becoming increasingly likely to be connected through a power electronic interface [3, 4, 10, 15, 16, 17, 18]. It is well known that motor drives can drastically improve overall efficiency and controllability [9]. Motor drives are even becoming common in relatively low-cost residential applications such as air conditioning, washing machines, and refrigerators. Lighting, which represents about 20% of energy consumption, is slowly becoming a power-electronic application. New legislation in the United States, for instance, calls for the end of the incandescent bulb, which is likely to usher in the use of compact fluorescent and LEDs. In both cases, power electronic interfaces are required.

1.2. Research Context

Although power electronics offer a number of benefits, they introduce new problems and complications. These issues primarily arise from the interaction between power converters and the equivalent impedance of the power system. For instance, many grid-interfaced power electronic loads tend to have rectifiers that introduce harmonic currents. When these currents flow through the non-zero impedance of the network, the resulting voltage distortion can affect other loads. This phenomenon can be corrected with active rectifiers, but the interaction between the grid and the converter can become unstable depending upon the network impedance values. All of these issues are particularly important in next-generation power electronic based power-distribution systems (PEBDS). In these systems, most sources and loads are connected to the distribution network through active power electronic devices. Figure 1.1 shows an example system with a DC bus. Such

systems are becoming increasingly common in aircraft, spacecraft, and next-generation all-electric ships. Such systems are fully active and thus highly dynamic. The equivalent network impedance seen at any point in the network can vary significantly over time, thus leading to instability. Microgrids, which consist of medium and/or low voltage distribution systems with distributed energy sources, controllable loads, and energy-storage devices, are a terrestrial incarnation that approaches a PEBDS. Figure 1.2 shows an example. Note that these microgrids can be connected and disconnected from the wider power system as needed, meaning that individual loads and sources are connected to a highly dynamic system. This section provides a direct context for the work presented in this thesis. It introduces several of the motivating issues, both for the existing terrestrial power system and for future PEBDS and microgrids.
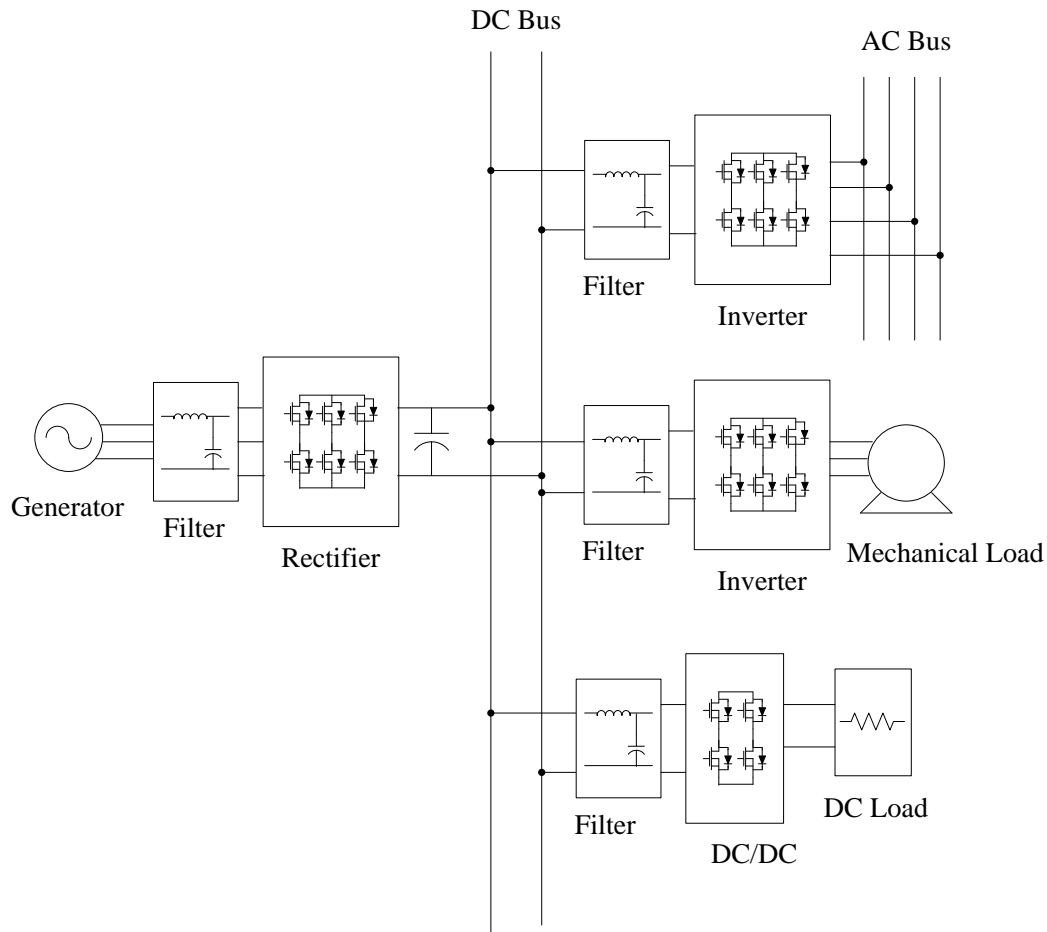
Figure 1.1: A representative of power electronics based distributed system.
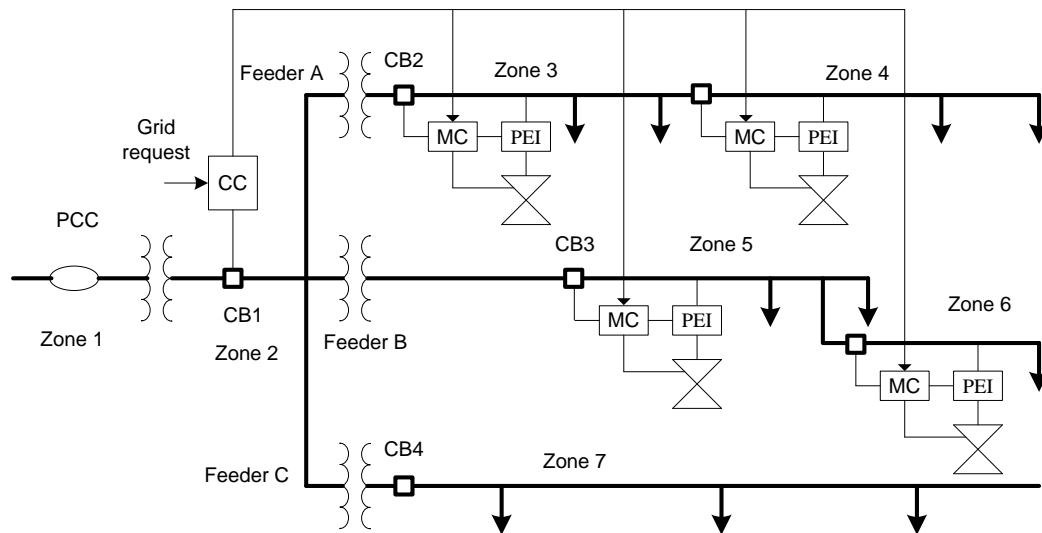
Figure 1.2: A typical microgrid configuration.

1.2.1. Power Electronics and Power Quality

The prolific growth of power electronic equipment in power systems has raised the need to study power quality. In traditional power systems, customers expect utilities to provide non-distorted and voltage waveforms with a single frequency component. In modern power systems, power electronic loads with rectifiers are widely used and draw non-sinusoidal currents. These disturbances can impact the operation of other loads connected to the same portion of the power system. Therefore, electric power quality is a serious consideration. Low power quality can impact electrical quantities such as current, voltage, and frequency. In the majority of cases, equipment failures or misoperations are caused by significant deviations in the voltage wave shape. For this reason, it is the quality of the voltage waveform that is typically being addressed in most cases involving low power quality.For this reason, Fuchs [19] defines power quality as: "the measure, analysis, and improvement of the bus voltage to maintain a sinusoidal waveform at rated voltage and frequency." The definition includes both long term (i.e. steady state) and short term (i.e. transient) phenomena.

Network impedance plays a key role in power quality problems. Figure 1.3 shows a

simple circuit that illustrates the problems. The equivalent impedance of the system is represented by $Z_s = R + jX$. Note that a rectifier is connected in parallel with several other loads. The utility is assumed to generate a 60 Hz sinusoidal voltage as indicated by the ideal source. Since the rectifier is nonlinear, it will generate harmonic currents. If the currents at the h-th harmonic has an amplitude I_h, then the voltage at the secondary side bus at the same frequency will be

$$V_h = RI_h + jhXI_h. \tag{1.1}$$

This voltage causes other linear loads to draw harmonic currents as well. The resulting feedback loop further modified the value of V_h. The voltage drop in wiring impedance can have very serious consequences on nearby loads. The resulting distortion can shutdown or damage equipments, causing losses in productivity and materials. Some modern manufacturing and service industries require highly automated processes which are more complex and more sensitive to supply disturbances. For example, semiconductor plants are probably exposed to the highest risk of potential financial losses due to power quality disturbances, as they concentrate enormously expensive facilities and equipment in a small area. Liquid crystal industries, and data centers are particular sensitive to service interruptions since they can cause information loss. Mission-critical customers such as hospitals, and air traffic control must also be protected from power quality disturbances. Unfortunately, harmonic-related disturbances are one of the more frequent and expensive power quality problems [11, 20, 21]. In addition to impacting customers, these harmonics currents also increase line losses thermal and stress throughout the network.

1.2.2. Active Power Electronic Interfaces and Instability

Harmonic current introduced by rectifiers can be reduced using various passive filter, but the corresponding components tend to be bulky and expensive. In portable systems (i.e. ships) the weight may be prohibited. Controlled AC/DC converters with active power factor
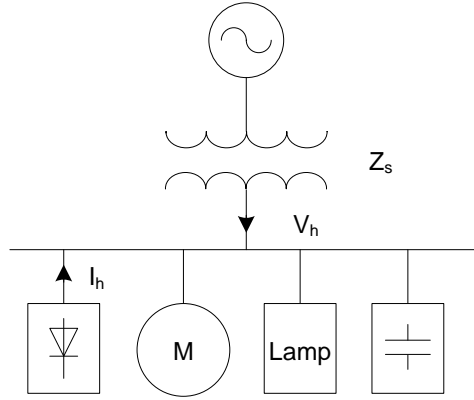
Figure 1.3: A simple circuit representing the propagation of disturbances.

correction (PFC) are now widely used as a solution [11, 22, 23, 24]. In these circuits, the input current is actively shaped to be sinusoidal using a boost-mode DC-to-DC converter or another common DC-to-DC converter topology [25]. Active PFC converters can operate over a wide range of input voltage, reduce THD to very low levels, increase efficiency, and decrease weight.

Whenever active power electronic systems are connected to the network, dynamic stability problems can result from the interaction with the equivalent impedance. For example, when a power electronic converter is tightly regulated so that it draws a constant power, it will have an incrementally negative impedance characteristic at low frequency [26]. Thus, if the input voltage changes by some amount, the input current will rise in order to keep the power constant. This incremental negative impedance characteristic interacts with source impedance and/or the input EMI filter stage to cause instability result in unstable possibility of the power system [27, 28]. Instability is common in both DC and AC power systems. The resulting oscillations degrade system performance, reduce power quality, increase lo asses and potentially stress all devices sharing the same power path. Low frequency oscillations have been observed in many applications such as those involving uninterruptible power supplies (UPS), small controlled generators, and regulating transformers with high internal impedance. Oscillations are increasingly likely in higher frequency microgrid systems (i.e. those with 400/800Hz voltage) such as those found in

airplane and warships [23, 29, 30, 31, 32, 33, 34, 35, 36].

Approaches have been developed to counteract the effects of instability. Typical approaches involve the use of conservative design criteria based on certain assumptions about the line impedance. Other solutions involve the use of appropriate filter stages [37, 23]. These solutions can be limited in highly dynamic systems in which line impedance can change. Consider for example a microgrid that is suddenly islanded. This will cause a change in the equivalent impedance seen by various loads and sources, making it possible for certain converters to become unstable. The resulting voltage instability can affect the performance of other loads. It is thus wise to consider approaches that can dynamically compensate for instability. The instability issues described above are not limited to active PFC converters.

1.3. Thesis Contributions

The ultimate goal of this thesis is to improve power quality and stability in power systems with high levels of power electronics. To that end, a number of different topics have been considered. The primary contributions are summarized here.

1.3.1. Network Impedance Estimation

The the most valuable contribution of this thesis is the development of a minimally intrusive on-line technique for grid impedance estimation. It is essential to all of the other contributions described herein. The proposed technique estimates the network impedance using very small disturbances in the power network. These disturbances can be either actively or passively injected. The proposed approach has benefits over traditional active measurement methods, which are generally the most popular in practice [38, 39, 40, 41, 42, 43, 44]. These methods are generally preferred because they allow for injections at appropriate interharmonic frequencies at which negligible harmonic content is present. Furthermore, the use of an active approach means that the impedance can be measured

across a broad frequency spectrum [43, 40]. Traditional active methods suffer from several limitations, however. The biggest issue is the need to supply disturbances large enough to obtain accurate measurements. This requires the injection of relatively large disturbances and thus causes power quality to be degraded. Depending upon the application, a dedicated source may be needed, and this source can be both expensive and complicated, especially at high voltage levels [43]. The proposed method, on the other hand, does not require a separate signal generator, and it can rely on disturbances that are several orders of magnitude smaller than those required by existing methods. The proposed approach can be integrated into existing power-electronic loads such as active PFC converters, and it can be applied across a wide range of frequencies without any need for special test sources.

The impedance estimation procedure shown here can also be applied passively using existing disturbances. Grid impedance is estimated at various interharmonic frequencies already present in the power system. Such signals are common and are produced by loads such as induction machines and power supplies. The proposed method can be integrated into any existing power quality diagnostic instruments. In such cases, the passive approach is extremely attractive.

It should be noted that the proposed method is developed and verified in single-phase AC systems. In general, it could also be applied in DC systems, or to each phase in three phase systems.

1.3.2. Adaptive Power Converter Control

Modern power systems feature active AC/DC converters that increase power quality and improve overall energy efficiency. These active power factor correcting (PFC) converters are common in data servers and motor drives. The drawback is that the interaction between the PFC converter and the rest of power system potentially result in instability. Most existing research attempts to alleviate this instability by testing the system under all potential load conditions or by quantitatively calculating the relative stability margins based on

knowledge of system parameters and expected loading conditions. These parameters and conditions, however, continually change in practice, making it possible that instability can result.

This research proposes a new adaptive control method to addresses the issue of instability when converters are connected to the system. First, we model a PFC stage based on a boost converter operating in the Continuous Conduction Mode (CCM). The focus is on the interaction between the power system and the PFC stage. Second, the possibilities of instability as a result of a time varying system impedance is analyzed. Third, a new control method is proposed that adapt to changes in network conditions. This method is based on the impedance measurement technique described above. This adaptive controller is demonstrated using a 350W single-phase boost-mode.

The proposed analysis and control method is general and topologically independent. It can be implemented in many other grid-tied converter and inverter circuits (i.e. those based on Cuk, SEPIC, etc.). The proposed method is also unlimited by the input filter stage, as long as bandwidth limitations imposed by computations in the feedforward loop do not affect overall stability.

1.3.3. Monitoring of Low Power Quality Sources

The need to precisely identify the source of harmonic disturbances is growing because the damaging effects of harmonics can no longer be ignored. Assessment of low power quality sources therefore increase accredits and responsibilities of all parts in power system networks. In practical grid measurements, it is mostly difficult to assign the measured disturbances values clearly from utilities or from loads due to the complicate and messy networks. This research proposes a promising method to address such measurement of the existing disturbances level in the grid without interruption load's operation.

The main advantage of the proposed method is that only waveforms of voltages and currents are required and they are applicable to both single and three phase systems. The

conventional methods aimed at distinguishing between load harmonics and source harmonics assume a radial feeder supplying a single load through a known feeder impedance, or multiple loads connected to a point of common coupling which has a sinusoidal voltage and with zero impedance in the supply feeder. Such assumptions are not correct in many current and future of power systems, since the varying characteristics of network impedance. The assumptions, however, are not required here since grid impedance can be measured at any point of interest as described in

1.3.4. Monitoring of Low Power Quality Sources

Many researchers have addressed the desire to identify the source of harmonic disturbances in power systems, and thus charge tariffs based on this information. In practical applications, it is difficult to determine the cause of harmonic disturbances since even linear loads will draw harmonic currents if other non-linear loads are drawing harmonic currents that distort the voltage at the point of common coupling. This research proposes a promising method to address the measurement of existing disturbances levels without interrupting load operation.

The main advantage of the proposed method is that only voltage and current waveforms are required. Conventional methods aimed at distinguishing between load harmonics and source harmonics assume a radial feeder supplying a single load through a known feeder impedance, or multiple loads connected to a point of common coupling which has a sinusoidal voltage and with zero impedance in the supply feeder [45]. Such assumptions are not correct in many cases because of the time varying characteristics of network impedance. These assumptions, however, are not required here since grid impedance can be measured at any point of interest as described previously. The primary benefit of the proposed method is that it can be used to obtain results and draw conclusions about a customer's harmonic profile from a Thevenin equivalent circuit, without any a priori information about the network structure. This method could be integrated into power measurement instruments.

1.4. Thesis Outline

The remaining chapters of this thesis provide appropriate background and details about the key contributions described above. Chapter 2 provides the fundamental information needed to model network impedance and the interaction between power electronics and the system. It describes the power quality degradation caused by power electronics, and it analyzes instability phenomena in converters with active front ends. It is followed by review of power quality and effects of the network impedance to the power quality of the power systems.

Chapter 3 presents the proposed method for online estimation of network impedance. The chapter begins with review of previous work. The remainder of this chapter is dedicated to present theoretical development, simulation, and experimental verification.

Chapter 4 presents the first application of the proposed impedance estimation method, which is an adaptive controller that prevents instability when active power electronic converters are connected to the power network. A grid-connected boost-stage PFC converter is modeled and the instability interaction is investigated via Matlab simulation. Two new control methods are proposed to help the PFC converter to adapt to time-varying network conditions. A 380 Watt PFC converter is used to verify the methods experimentally in the laboratory.

Chapter 5 describes how the proposed impedance estimation method can be used to detect the source of power quality disturbances. This chapter first reviews previous work and describes deficiencies in practical applications. A new method for disturbance monitoring is developed, and simulation results are provided.

Finally, Chapter 6 provides conclusions and recommendations for future work.

CHAPTER 2: RELEVANT MODELS FOR POWER DISTRIBUTION
SYSTEMS AND POWER ELECTRONIC LOADS

Equivalent grid impedance has a significant impact on the overall power quality in modern electric power systems. It plays a key role in various transient events such as short-term voltage sags and short circuits. It is also the conduit through which load-generated harmonic currents impact the entire network. Grid impedance also has a major impact in many outage scenarios, as it can allow large current oscillations to propagate throughout a network, especially in so-called weak systems in which the impedance value is high [5, 46]. When power electronic loads are connected to a source through this grid impedance, various undesirable phenomena can occur, including harmonic generation and load instability. A complete understanding of these effects requires an understanding of the equivalent impedance model of the distribution system, as well as an understanding of the equivalent input model for a power converter.

This chapter presents models for both the power system and the power electronic circuits connected to it. It begins by presenting an approximate model for the impedance of a traditional power distribution network. The results of this modeling procedure are essential to the development of the impedance estimation procedure described in Chapter 3. In addition, this chapter also describes how power electronic circuits affect the AC network. It thus describes how passive power electronics (i.e. rectifier-type loads) generate harmonic currents, and it also addresses the stability issues that arise when active wave shaping circuits are connected to the network. These discussions provide the necessary background for understanding the work in Chapters 4 and 5. Given that the latter chapters focus on a single-phase connections to the utility, the models presented here are generally focused on

such systems.

2.1. A Model for the Impedance of the Electric Power Distribution System

Figure 2.1 shows a typical distribution circuit. Notice that most residential and commercial customers are served from radial feeders and secondary distribution networks. In the context of this thesis, the question of interest is the impedance seen by a load connected at any one of the industrial, commercial, or residential load centers present in this network. The development of a model for this impedance requires a detailed analysis of each of the various elements that impact it. These include cables, transformers, and loads. Models for these elements are presented here. Ultimately, they are synthesized to develop a suitable lumped-element approximation for the impedance seen by any load connected to the network. In this thesis, the primary focus is on single-phase connections to the utility such as those that would be seen from one of the loads connected to the secondary of a distribution transformer on one of the residential or commercial laterals shown in Figure 2.1.

2.1.1. The Equivalent Impedance of Power Distribution Lines

Power lines are typically characterized using four parameters, namely series resistance, series inductance, shunt capacitance, and shunt conductance [47, 48, 49]. Since loads are connected to the network through various cables, it is important to review the fundamental phenomena giving rise to these parameters. Models for each are given below. Ultimately, these are combined to create a complete power-line model.

2.1.1.1. Conductor Resistance

Resistive losses in a conductor are impacted by various phenomena, including temperature and frequency. The equivalent DC resistance of a line is proportional to its length and
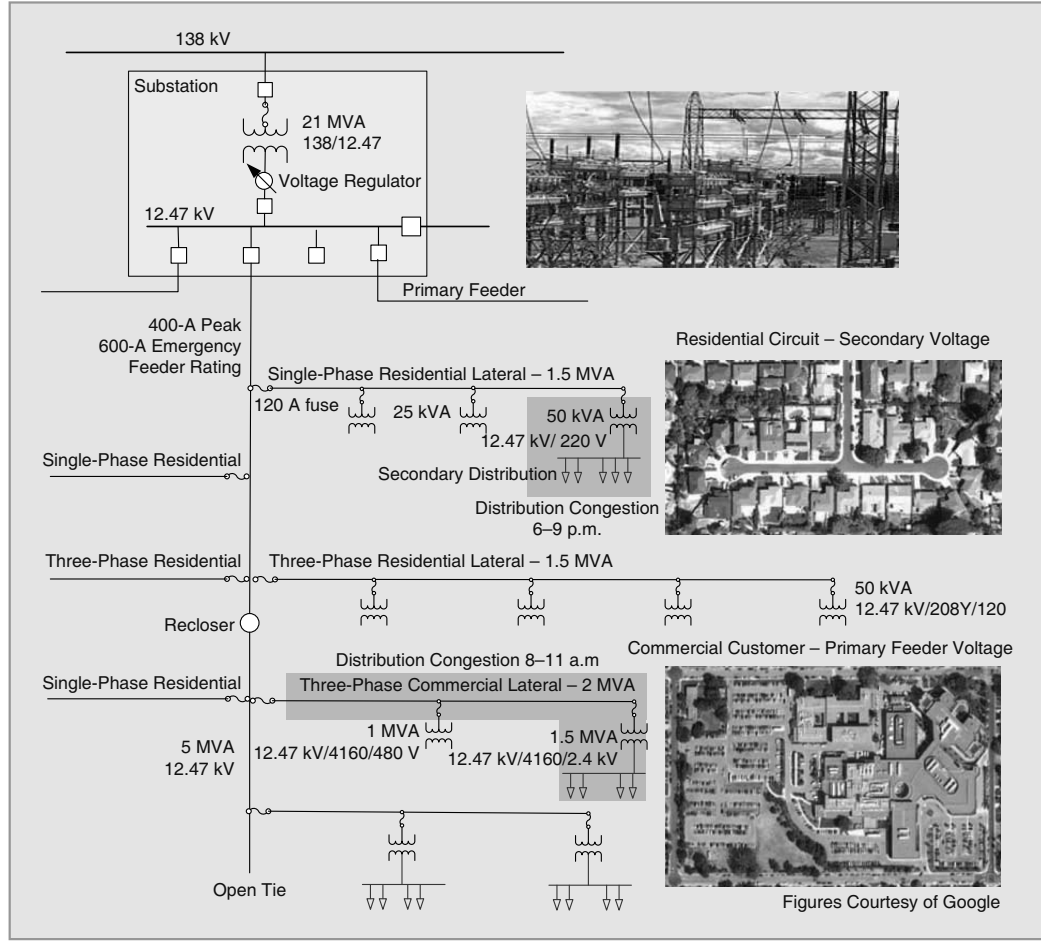
Figure 2.1: A typical distribution circuit [1].

inversely proportional to its cross-sectional area. By definition, this resistance is

$$R_{DC} = \frac{\rho l}{A}, \tag{2.1}$$

where ρ is the resistivity of the conductor at a given temperature, l is its length, and A is its cross-sectional area. This effective resistance is proportional to the power loss in the line at DC. This model assumes that the distribution of current throughout the conductor is uniform, which is the case at DC [25]. In AC systems, currents become concentrated near the surface of the conductor. This phenomenon, which is known as the skin effect, reduces the effective cross-sectional area used by the current. As a result, the effective resistance increases. The AC resistance of any conductor including skin effect can be calulated directly

from Maxwell's Equations [50]. For frequencies above 1 kHz, this effective resistance is approximated as

$$\frac{R_{ac}}{R_{dc}} = 0.009786\sqrt{\frac{f\mu}{R_{dc}}} + 0.25, \tag{2.2}$$

where f is frequency, μ is the relative permeability of the conductor, and R_{dc} is the DC resistance of the conductor in Ω per 1000 ft (Ω/1000ft).

The resistivity of any conductive material varies linearly with respect to temperature over the normal range of operation. In general, a hotter conductor provides more resistance to the flow of current. Over normal operating temperatures, the dependence is

$$R_2 = R_1 \left(\frac{T + t_2}{T + t_1} \right). \tag{2.3}$$

In this equation, R_2 is the resistance at temperature t_2, R_1 is the resistance at temperature t_1, and T is a material-specific temperature coefficient. Resistivity and temperature coefficient values depend upon the conductor material. Table 2.1 lists the resistivity and temperature coefficients of some typical conductors [48].

Table 2.1: Resistivity and temperature coefficients of some typical conductor materials.

Material	Resistivity at 20°C ($\Omega - m$)	Temp. Coefficient (°C)
Silver	1.59×10^{-8}	243.0
Annealed copper	1.72×10^{-8}	234.5
Hard-drawn copper	1.77×10^{-8}	241.5
Aluminum	$2.83. \times 10^{-8}$	228.1

2.1.1.2. The Series Impedance of Power Distribution Lines

The series impedance of any set of distribution lines consists of the resistance and the self and mutual inductans resulting from the magnetic fields surrounding the conductors. In general, distribution systems consist of single-phase, two-phase, and three-phase lines

serving unbalanced loads. The actual models for the series impedance depend upon where the cables are placed, either above ground or below. For illustrative purposes, this thesis considers overhead lines, although both types of cables are likely to be observed in many distribution systems. The results are generally similar [48].

Analysis of the impedance on an overhead distribution line requires one to include the self and mutual impedance terms of the conductors and the ground return path. In his classic paper [51], Carson developed a technique to determine the self and mutual impedances of overhead conductors with a ground return path. The technique uses image conductors; that is, every conductor at a given distance above ground has an image conductor the same distance below ground. The earth return path is assumed to be an infinite, uniform solid with a flat uniform upper surface and a constant resistivity [48].

As an example, Figure 2.2 shows a two-wire overhead line with solid cylindrical conductors i and j separated by a distance D_{ij}. The conductors are made of a nonmagnetic material, and the current is assumed to be uniformly distributed (i.e. skin effect is negleged).
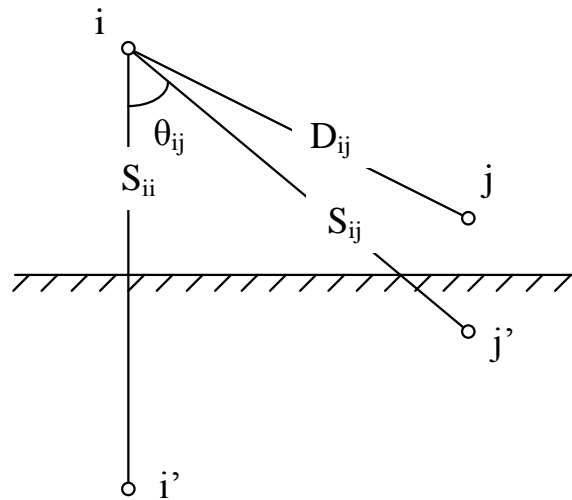
Figure 2.2: Conductors and images.

Carson's formula for the self impedance per unit length of an overhead conductor is

$$\hat{z}_{ii} = r_i + 4\omega P_{ii}G + j2\omega G \left(\ln \frac{S_{ii}}{GMR_i} + 2Q_{ii} \right). \tag{2.4}$$

Similarly, the mutual impedance per unit length is

$$\hat{z}_{ij} = 4\omega P_{ij}G + j2\omega G \left(\ln \frac{S_{ij}}{D_{ij}} + 2Q_{ij} \right) \tag{2.5}$$

In Equation 2.4 and Equation 2.5, the following definitions have been used:

$G = 0.1609344x10^{-3}$ Ω/mile

$\omega = 2\pi f$ is the system angular frequency in radians per second

f = system frequency in Hertz

D_{ij} = distance between conductors i and j in feet

S_{ij} = distance between conductor i and image j in feet

In addition, we have used GMR_i, which is the effective radius or geometric mean radius of conductor i in feet. The P and Q terms in the preceding equations are often approximated as

$$P_{ij} = \frac{\pi}{8} \tag{2.6}$$

$$Q_{ij} = 0.30797 - \frac{1}{2} \ln \left(8.565.10^{-4} S_{ij} \sqrt{\frac{f}{\rho}} \right). \tag{2.7}$$

Note that the resistivity ρ in Equation 2.7 represents the resistivity of the Earth.

Equations 2.4 and 2.5 can be used to calculate the complete impedance matrix for a line with *ncond* conductors and *mcond* neutrals. This first requires the calculation of the so-called primitive impedance matrix, which represents the combined effects of the conductors, the neutrals, and the ground paths. For most three-phase, four-wire applications the primitive impedance matrix needs to be reduced to a 3x3 matrix consisting of the self and mutual impedances for the three phases and the multi-grounded neutral *n*. The flux linkage of each phase conductor depends on the three currents, and therefore, three differ-

ent inductances (i.e. one self and two mutuals) exist for each. Calculating the values from the equations above and arranging the equations in matrix form, we obtain the primitive impedance matrix

$$\hat{\mathbf{z}}_{\mathbf{primitive}} = \begin{bmatrix} \hat{\mathbf{z}}_{\mathbf{ij}} & \hat{\mathbf{z}}_{\mathbf{in}} \\ \hat{\mathbf{z}}_{\mathbf{nj}} & \hat{\mathbf{z}}_{\mathbf{nn}} \end{bmatrix}, \tag{2.8}$$

where

$$\hat{\mathbf{z}}_{\mathbf{ij}} = \begin{bmatrix} \hat{z}_{aa} & \hat{z}_{ab} & \hat{z}_{ac} \\ \hat{z}_{ba} & \hat{z}_{bb} & \hat{z}_{bc} \\ \hat{z}_{ca} & \hat{z}_{cb} & \hat{z}_{cc} \end{bmatrix}, \hat{\mathbf{z}}_{\mathbf{nj}} = \begin{bmatrix} \hat{z}_{na} & \hat{z}_{nb} & \hat{z}_{nc} \end{bmatrix}, \hat{\mathbf{z}}_{\mathbf{in}} = \begin{bmatrix} \hat{z}_{an} \\ \hat{z}_{bn} \\ \hat{z}_{cn} \end{bmatrix}, \hat{\mathbf{z}}_{\mathbf{nn}} = \hat{z}_{nn}.$$

If the neutral is grounded, the impedance can be solved by Kron's reduction [48], i.e.

$$\mathbf{z}_{abc} = \mathbf{z}_{ij} - \mathbf{z}_{in}(\mathbf{z}_{nn})^{-1}\mathbf{z}_{nj}. \tag{2.9}$$

The impedance matrix of a 3 phase line with a common grounded neutral is thus

$$\mathbf{z}_{abc} = \begin{bmatrix} z_{aa} & z_{ab} & z_{ac} \\ z_{ba} & z_{bb} & z_{bc} \\ z_{ca} & z_{cb} & z_{cc} \end{bmatrix} (\Omega/mile). \tag{2.10}$$

In the applications considered in this thesis, we are focused on single phase connections to the utility. For two-phase and single-phase lines in grounded wye systems, the modified Carson's equations can be applied, but they lead to simpler results. Kron reduction is again applied to the primitive matrices in order to reduce them to either 2x2 or 1x1. These matrices are expanded to 3x3 by the addition of rows and columns consisting of zero elements

for the missing phases. The phase impedance matrix for a single-phase line would thus be

$$
\mathbf{z}_{abc} = \begin{bmatrix} 0 & 0 & 0 \\ 0 & z_{bb} & 0 \\ 0 & 0 & 0 \end{bmatrix} (\Omega/mile).
\tag{2.11}
$$

2.1.1.3. Capacitance and Capacitive Reactance

Since power lines are conducting bodies separated by a dielectric medium, there is a shunt admittance between them. In a distribution line, the shunt admittance exists in the form of conductance and capacitive susceptance among the phases, neutral lines, and ground. The conductance, which represents leakage current, is usually ignored because it is very small compared to the capacitive susceptance [48]. The capacitance of a line results from the potential difference between conductors. To evaluate it, one computes the electric field strength using Gauss's Law [47]. In the calculation of capacitance for an overhead distribution line, the earth effect is accounted for by the method of images as described for the inductance. When the conductor has a positive charge, an equal quantity of negative charge is induced on the image conductor under the earth. Again only overhead lines are considered here, but the development is similar for underground cables.

Consider two conductors i and j carrying charges q_i and q_j and the image conductors i' and j' that carry charges $-q_i$ and $-q_j$. The potential difference between conductor i and ground thus includes both a self and mutual potential. This voltage is defined as

$$
V_{ig} = \hat{P}_{ii} q_i + \hat{P}_{ij} q_j,
\tag{2.12}
$$

where $\hat{P}_{ii}$ and $\hat{P}_{ij}$ are the self and mutual potential coefficients. These are defined as

$$
\hat{P}_{ii} = \frac{1}{2\pi\varepsilon} \ln \frac{S_{ii}}{RD_i}, \quad \hat{P}_{ij} = \frac{1}{2\pi\varepsilon} \ln \frac{S_{ij}}{D_{ij}}.
\tag{2.13}
$$

where ε is the permittivity of the medium between the cables, S_{ii} is the distance between conductor i and its image, S_{ij} is the distance between conductor i and the image of conductor j, RD_i is the effective radius of conductor i, and D_{ij} is the distance between conductor i and j.

To determine the complete capacitance matrix, we begin again with a set of primitive matricies. For an overhead line consisting of *ncond* conductors, the primitive potential coefficient matrix can be constructed. The primitive potential coefficient matrix will be an *ncond* x *ncond* matrix. For a four-wire grounded wye line, the primitive coefficient matrix will be of the form

$$\hat{\mathbf{P}}_{\textbf{primitive}}=\begin{bmatrix} \hat{\mathbf{P}}_{\textbf{ij}} & \hat{\mathbf{P}}_{\textbf{in}} \\ \hat{\mathbf{P}}_{\textbf{nj}} & \hat{\mathbf{P}}_{\textbf{nn}} \end{bmatrix}, \tag{2.14}$$

where

$$\hat{\mathbf{P}}_{\textbf{ij}} = \begin{bmatrix} \hat{P}_{aa} & \hat{P}_{ab} & \hat{P}_{ac} \\ \hat{P}_{ba} & \hat{P}_{bb} & \hat{P}_{bc} \\ \hat{P}_{ca} & \hat{P}_{cb} & \hat{P}_{cc} \end{bmatrix}, \hat{\mathbf{P}}_{\textbf{nj}}=\begin{bmatrix} \hat{P}_{na} & \hat{P}_{nb} & \hat{P}_{nc} \end{bmatrix}, \hat{\mathbf{P}}_{\textbf{in}}=\begin{bmatrix} \hat{P}_{an} \\ \hat{P}_{bn} \\ \hat{P}_{cn} \end{bmatrix}, \hat{\mathbf{P}}_{\textbf{nn}} = \hat{P}_{nn}. \tag{2.15}$$

This primitive matrix is once again reduced using the Kron reduction method to a n phase x n phase matrix, i.e.

$$\mathbf{P}_{abc} = \hat{\mathbf{P}}_{ij} - \hat{\mathbf{P}}_{in}(\hat{\mathbf{P}}_{nn})^{-1}\hat{\mathbf{P}}_{nj} \tag{2.16}$$

The inverse of this potential coefficient matrix gives the *nphase* x *nphase* capacitance matrix, i.e.

$$\mathbf{C}_{abc} = \mathbf{P}_{abc}{}^{-1}. \tag{2.17}$$

This a three-phase system, this is

$$\mathbf{C_{abc}} = \begin{bmatrix} C_{aa} & C_{ab} & C_{ac} \\ C_{ba} & C_{bb} & C_{bc} \\ C_{ca} & C_{cb} & C_{cc} \end{bmatrix}. \tag{2.18}$$

Neglecting the shunt conductance, the overall phase shunt admittance matrix is

$$\mathbf{Y_{abc}} = \mathbf{0} + \mathbf{j}\omega\mathbf{C_{abc}}(\mathbf{S/mile}). \tag{2.19}$$

In systems with three phase conductors and one or two ground wires, $\mathbf{C_{abc}}$ may be very complicated. In balanced situations, this matrix can be simplified. For a single-phase line, $\mathbf{C_{abc}}$ has only a single element.

Distribution line capacitance is negligible in most applications, particularly those with short lines. In some cases, however the capacitance should not be ignored. To see this, carefully consider the capacitance relationship. The equations show that the capacitance per unit length depends on the space between conductors and also on the permitivity of the dielectric separating them. Thus, the capacitance per unit length of underground cables may be much greater than the capacitance per unit length of overhead lines [48]. The effect of such capacitance in terms of this thesis is addressed below.

2.1.2. The Complete Distribution Line Model

From the analysis above, we note that distribution line impedance mainly depends on conductor size, conductor spacing, network configuration (i.e. with or without a neutral line), the method of grounding, and earth resistivity. In general, all such lines are most appropriately represented as distributed (i.e. non-lumped) systems. The use of lumped-element impedances has been found to be accurate over line segments of appropriate length [48]. The equivalent circuit model for a line sigment, which is known as the pi-line repre-

sentation, is shown in Figure 2.3. In this thesis, we are focused on single phase connections. The line to neutral representation of the single-phase equivalent circuit is shown in Figure 2.3. This model has been found to be quire accurate for short lines and for lines of medium length. Here, R represents the complete resistance and L the complete series inductance. The appropriate capacitance is placed at each end of the line.
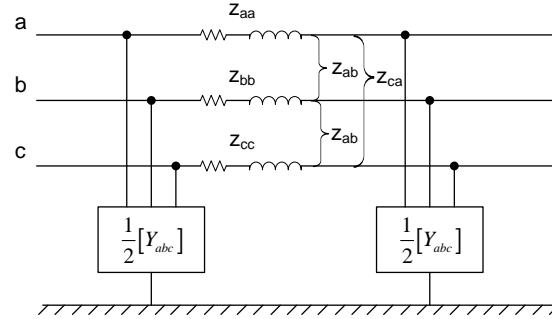
Figure 2.3: Three-phase line segment model.

The focus in this thesis is on short-distance lines, such as those connecting loads to distribution transformers. If a distribution line is classifed as short (li.e ess than about 80 km or 50 mi), the shunt capacitance is so small that it is often omitted entirely with little loss of accuracy, even in underground cables wi[47]. Figure 2.4(b) shows the simplified model in which the series resistance R and the series inductance L apply to the total length of the line.

(a)   (b)
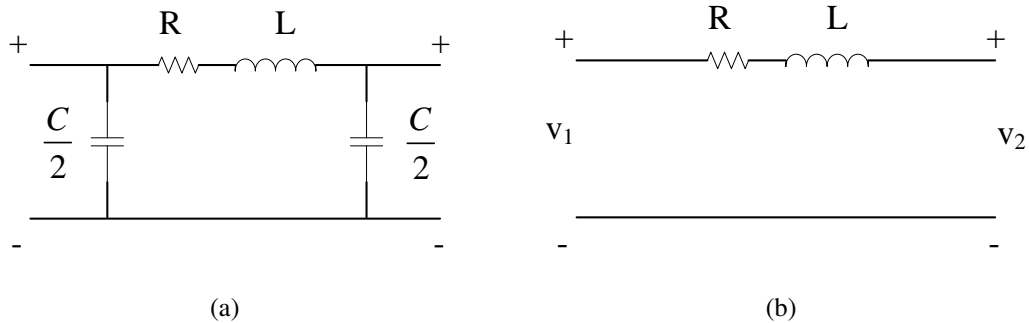
Figure 2.4: (a) Single-phase equivalent of transmission line.
(b) Single-phase equivalent of short-length transmission line.

Note that the models derived here assume operation at a constant temperature and nominal line frequency. In general, the series inductance and resistance are frequency dependent due to the earth return effect and the conductor skin effect [48, 47]. Experience shows that such frequency dependence is generally small for low-order harmonics of the fundamental. A common analytical approach is thus to use the inductance and resistance parameters calculated at the fundamental frequency over much of the frequency spectrum. An improved approach is to use the parameters calculated at the key harmonic frequencies of interest. In this case, it may be important to include the shunt element because the shunt admittance can become quite significant at higher frequencies. The increased admittance could interact with the series impedance of the line, thus causing harmonic resonance. This can be easily modeled by returning to the more accurate equivalent pi-circuit.

2.1.3. Transformers Models

Transformers are used for various purposes in distribution systems, such as to convert AC voltage from one level to another. Single-phase distribution transformers typically have one high-voltage primary winding and two low-voltage secondary windings [50]. This thesis focuses on networks with such transformers, and thus it is instructive to review the equivalent model.

Figure 2.5 shows the single-phase equivalent circuit for a transformer. The main element is the ideal transformer with transformation ratio $n = N_2/N_1$. Reactances X_p and X_s account for leakage fluxes. Similarly, ohmic losses are expressed using the resistances R_p and R_s. The effects of magnetization and core loss are represented by the elements X_m and G_c, respectively.

In power system analysis, an equivalent circuit is achieved by reflecting parameters from one side to the other and by making certain simplifying assumptions. Figure 2.6 shows an approximate equivalent circuit including primary side and reflected secondary side impedances. In practical distribution transformers, typical values of magnetizing re-
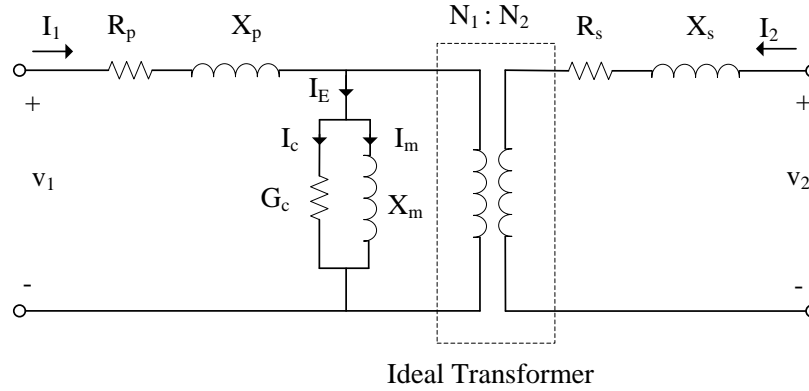
Figure 2.5: Single phase equivalent circuit of transformer.

actance are several orders of magnitude greater than typical values of leakage reactance. As a result, the magnetizing current and the core loss component in a loaded transformer tend to be very small with respect to I_2/n. These components are thus often ignored. The equivalent impedance of the transformer referred to the primary thus becomes

$$Z_{eq} = (R_p + jX_p) + n^2(R_s + jX_s) = R_{eq} + jX_{eq}. \tag{2.20}$$

Figure 2.7 shows this equivalent circuit. Using similar techniques, the primary side components can be refered to the secondary side. This issue is relevant in this thesis and is considered later when the complete system impedance is considered.
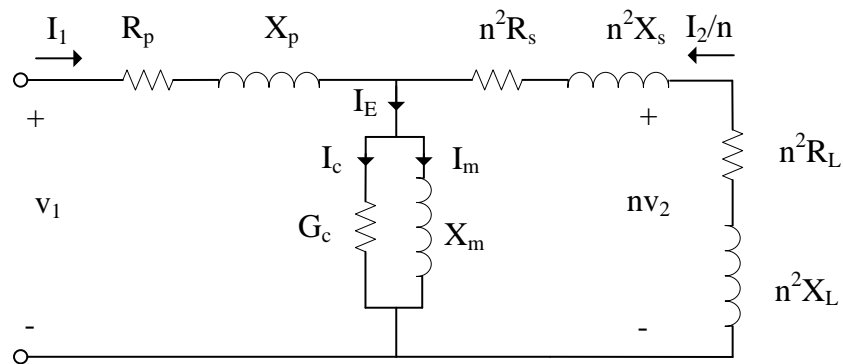
Figure 2.6: Single-phase equivalent circuit of a loaded transformer with the secondary parameters are referred to primary side.

The simplified transformer model shown in Figure 2.7 is used in most power system cal-
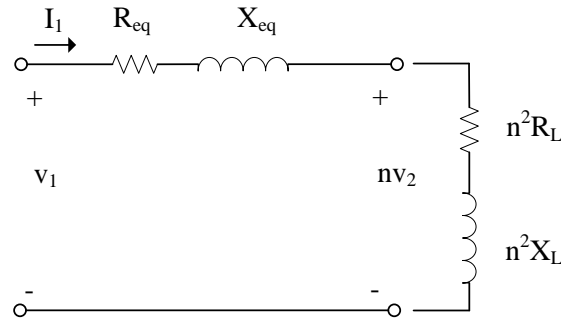
Figure 2.7: Simplified single-phase equivalent circuit of a transformer with magnetizing current neglected.

culations including load flows, short-circuit calculations, and motor starting. The primary-referred equivalent reactance is normally given in percent of transformer rating [50] using the following emprical formula

$$X_\% = \frac{126 f (NI)^2 rw}{10^{11} h S_{kVA}},$$

(2.21)

where f is system frequency, N is the number of turns on the primary, I_d is the full load primary current, r is the radius of the windings in inches, w is the width between windings in inches, h is the height of the windings in inches, and S_{kVA} is the transformer rating.

Note that the size and rating of a transformer have a significant impact on its reactance. Large power transformers used in distribution substations tend to have a reactance to resistance ratio (i.e. X/R) on the order of 10 to 40. Additional, series reactance is often added to limit fault currents.

In this thesis, the primary focus is generally on the smaller distribution transformers that are closer to the loads. These transformers tend to have lower X/R ratios because of their lower rating and size. In general, these X/R ratios are on the order of 0.5 to 5, which is consistent with laboratory measurements made in this thesis.

It is important to note that all parameters in the transformer model vary with temperature, frequency, and aging. In pacticular, the core loss term can become significant as frequency rises because of the dependence of hysteresis loss on frequency [48]. As with

cables, an equivalent impedance can be measured at each relevant frequency.

2.1.4. Load Model

Parallel-connected electrical loads also have an impact on the equivalent upstream impedance seen from any connection to the distribution system. In general, all loads are non-linear, as they draw a current that depends upon voltage, operating temperature, age, and the specifics of their particular power supply. Thus, it is difficult to represent loads via equivalent impedances, and they are often represented in system studies using their real and reactive power demands. In the context of this thesis, it is important to understand these models as they can impact the measured grid impedance. For instance, a large capacitor bank connected to a transformer secondary impacts the measured reactance. In this thesis, impedance measurements are made at single point in time, when it is assumed that most loads are in steady-state. In that instance, static load models are the most appropriate.

Static load models express the characteristics of the load as functions of the bus voltage magnitude and frequency. Table 2.2 presents static load models and their dependence on variations of voltage and temperature. These component models express per-unit real power and reactive power as a function of per-unit incremental voltage and/or incremental temperature. Looking at the models, the reactive power from some of loads, e.g. fluorescent lamps and mercury lamps, vary between inductive and capacitive based on the operating conditions.

In common model, the per unit real and reactive power are expressed as

$$
\begin{aligned}
P_u &= \frac{P}{P_0} = \left[\frac{V}{V_0}\right]^{\alpha_v} \left[\frac{f}{f_0}\right]^{\alpha_f}, \\
Q_u &= \frac{Q}{P_0} = \frac{Q_0}{P_0} \left[\frac{V}{V_0}\right]^{\beta_v} \left[\frac{f}{f_0}\right]^{\beta_f}.
\end{aligned}
\tag{2.22}
$$

Other static load models have been proposed use the following polynominals [48]

$$P_u = \frac{P}{P_0} = \left[Z_p + I_p \left(\frac{V}{V_0} \right) + P_p \left(\frac{V}{V_0} \right)^2 \right] (1 + D_p \Delta f),$$

$$Q_u = \frac{Q}{P_0} = \frac{Q_0}{P_0} \left[Z_q + I_q \left(\frac{V}{V_0} \right) + Q_q \left(\frac{V}{V_0} \right)^2 \right] (1 + D_q \Delta f).$$

$$(2.23)$$

In Equations 2.22 and 2.23, $[(\alpha_v,\ \alpha_f),\ (\beta_v,\ \beta_f\ )]$ are empricially derived exponents,Δf is per unit frequency deviation from nominal, V is the per unit voltage magnitude at the bus, V_0 is the initial per unit voltage magnitude before any variation, P_0 is the initial per unit active power, and Q_0 is the initial per unit reactive power. In the polynominal model, $Z_p + I_p + P_p = 1.$, and $Z_q + I_q + Q_q = 1$. D_p and D_q are damping coefficients. Values of these coefficientsfor typical residential loads relevant to this thesis are presented in Table 2.3

Table 2.2 provides nominal damping coeffiency for example residential appliances, which are directly relevant to this topic.

Table 2.2: Load Component Static Component Model.

Component	Equations
1- Central Air Conditioner	$P = 1.0 + 0.4311*\Delta V + 0.9507*\Delta T + 2.070*\Delta V^2 + 2.388*\Delta T^2 - 0.900*\Delta V*\Delta T$ $Q = 0.3152 + 0.6636*\Delta V + 0.543*\Delta V^2 + 5.422*\Delta V^3 + 0.839*\Delta T^2 - 1.455*\Delta V*\Delta T$
3- Central Air Conditioner	$P = 1.0 + 0.2693*\Delta V + 0.4879*\Delta T + 1.005*\Delta V^2 - 0.188*\Delta T^2 - 0.154*\Delta V*\Delta T$ $Q = 0.6957 + 2.3717*\Delta V + 0.0585*\Delta T + 5.81*\Delta V^2 + 0.199*\Delta T^2 - 0.597*\Delta V*\Delta T$
Room Air Conditioner (115V Rating)	$P = 1.0 + 0.2876*\Delta V + 0.6876*\Delta T + 1.241*\Delta V^2 + 0.089*\Delta T^2 - 0.558*\Delta V*\Delta T$ $Q = 0.1485 + 0.3709*\Delta V + 1.5773*\Delta T + 1.286*\Delta V^2 + 0.266*\Delta T^2 - 0.438*\Delta V*\Delta T$
Freezer	$P = 1.0+ 1.3286*\Delta V + 12.616*\Delta V^2 + 133.6*\Delta V^3 + 380*\Delta V^4$ $Q = 1.3810 + 4.6702*\Delta V + 27.276*\Delta V^2 + 293.0*\Delta V^3 + 995*\Delta V^4$
Fluorescent Lamp	$P = 1.0 + 0.6534*\Delta V - 1.65*\Delta V^2$ $Q = - 0.1535 - 0.0403*\Delta V + 2.734*\Delta V^2$
Mercury Vapor Lamp	$P = 1.0 + 0.1309*\Delta V + 0.504*\Delta V^2$ $Q = - 0.2524 + 2.3329*\Delta V + 7.811*\Delta V^2$
Sodium Vapor Lamp	$P = 1.0 + 0.3409*\Delta V -2.389*\Delta V^2$ $Q = 0.060 + 2.2173*\Delta V + 7.620* \Delta V^2$
Incandescent	$P = 1.0 + 1.5209*\Delta V + 0.223*\Delta V^2$ $Q = 0.0$
Water Heater	$P = 1.0 + 0.3769*\Delta V + 2.003*\Delta V^2$ $Q = 0.0$
Resistance Heating	$P = 1.0 + 2*\Delta V + \Delta V^2$ $Q = 0.0$

Table 2.3: Static Load Frequency Damping Characteristics.

Component	Dp	Dq
Three-Phase Central AC	1.09818	-0.663828
Single-Phase Central AC	0.994208	-0.307989
Window AC	0.702912	-1.89188
Duct Heater w/blowers	0.528878	-0.140006
Water Heater, Electric Cooking	0.0	0.0
Clothes Dryer	0.0	-0.311885
Refrigerator, Ice Machine	0.664158	-1.10252
Incandescent Lights	0.0	0.0
Florescent Lights	0.887964	-1.16844
Induction Motor Loads	1.6	-0.6

Steady-state load models can be constructed at various frequencies using static P and Q models. At the fundamental, for instance, one can derive the model shown in Figure 2.8, where

$$R_{load} = \frac{V^2}{P}, X_{load} = \frac{V^2}{Q}.$$ (2.24)

A emperically derived model for the hth harmonic is also shown in Figure 2.8. The parameters in that model are

$$R_{loadh} = \frac{V^2}{P}, \; X_{loadh} = 0.073 R_{loadsh}, \; X_{loadph} = \frac{h R_{loadh}}{6.7 \left(\frac{Q}{P} \right) - 0.74}.$$ (2.25)

where P and Q are the load active and reactive powers, respectively, at the fundamental frequency, and h is harmonic order.

2.1.5. Constructing the Complete Equivalent System Model

in a Time-Varying Environment

The previous sections introduced equivalent circuit models for distribution lines, transformers, and electrical loads. These are the critical elements affecting the equivalent
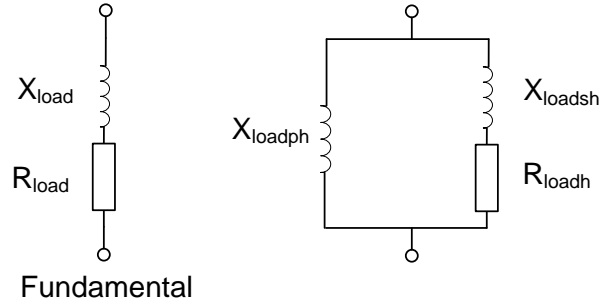
Figure 2.8: Harmonics models of passive load.

impedance seen from a typical single-phase connection to the utility. This section assembles these individual component models into a complete impedance model relevant to the problems considered in this thesis.

Return again to the distribution system shown in Figure 1.1. Consider a single-phase load connected to a transformer on one of the residential laterals. Assume that the voltage on the primary side of the substation transformer is fixed (i.e. the primary side is assumed to be an infinite bus) and that the load on all three phases is balanced. An equivalent single-phase model for the system as seen by the load is of the form shown in Figure 2.9. This model includes the effects of the substation transformer, distribution lines, the local transformer, and the effects of a parallel load impedance. In this case, distribution cabling has been represented using an equivalent pi-model. Furthermore, the model assumes that all loads draw only fundamental frequency currents and that that voltage at the primary side of the feeder is free of any harmonics. The model shown in Figure 2.9 can be simplified
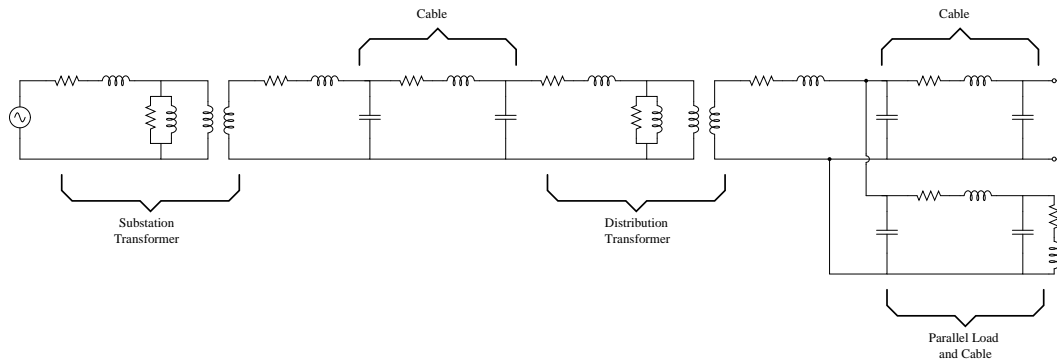
Figure 2.9: An equivalent single-phase model.

significantly if the cabling is considered to be short and has a negligible capacitance. Similarly, the magnetizing and core losse elements can be ignored. The model can thus be simplified as shown in Figure 2.10. If all of the impedances are refered to the secondary of the distribution transformer, the resulting reflections significantly reduce the primary side impedances. The resulting model shown in Figure 2.11 includes only R_{eq} and L_{eq}, which represent the combined series resistance and inductance as seen from the load terminals. Because of the reflections, R_{eq} and L_{eq} may be dominated by the distribution transfer and the secondary side cabling.
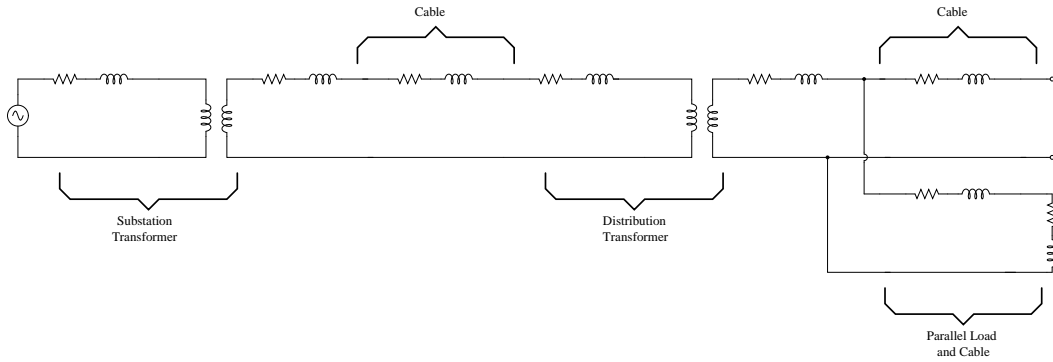
Figure 2.10: Simplified equivalent network model of Figure 2.9.
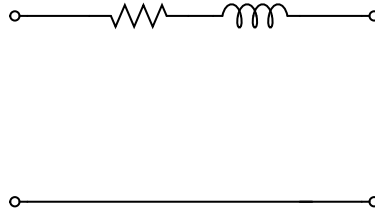
Figure 2.11: Simplified equivalent network model of Figure 2.10.

2.1.5.1. Introducing Non-Idealities into the Model

The model shown in Figure 2.11 is highly idealized. For example, the temperature characteristics of individual components cause the equivalent impedance to change over time. Furthermore, individual loads also connect and disconnect from the network. As this happens, R_{eq} and L_{eq} also change. As discussed previously, the impedances of each of

the components depend upon frequency. Furthermore, many networks have non-negligible stray capacitance at certain frequencies and Power Factor Correcting capacitors.

If we consider only frequency dependence, a more appropriate model for the impedance can be determined emprically from the FFT. Equivalent impedance characteristics could be expressed in terms of a parametric transfer function, or an equivalent network that has a transfer function close to the measured model. If the model contains severval dominant resonant frequencies, then it may be necessary to use a rational transfer function of the form

$$z(s) = \frac{a_n s^n + \ldots + a_2 s^2 + a_1 s + a_0}{b_m s^m + \ldots + b_2 s^2 + b_1 s + b_0}, \tag{2.26}$$

An equivalent network consisting of lumped resistive, inductive, and capacitive elements is shown in Figure 2.12. A simplified ladder network without resistances can also be used. Two possibilities are shown in Figure 2.13. A gain would neet to be included to modify the DC value to account for resistances [52].
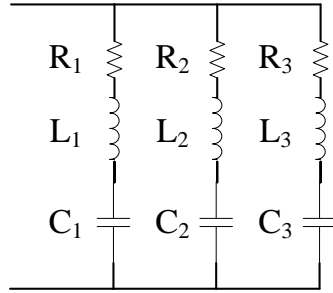
Figure 2.12: Aggregate impedance model in [2]

In general, even the parametric transfer function approach can be a gross simplification. The measured impedance characteristics change with time, and thus any $Z(s)$ is only valid over some short time window. An equivalent short-time model is shown in Figure 2.14. If one desires to determine the impedance over a certain range of frequencies, empirical methods and curve fitting could be used. This is the viewpoint considered in Chapter 3.
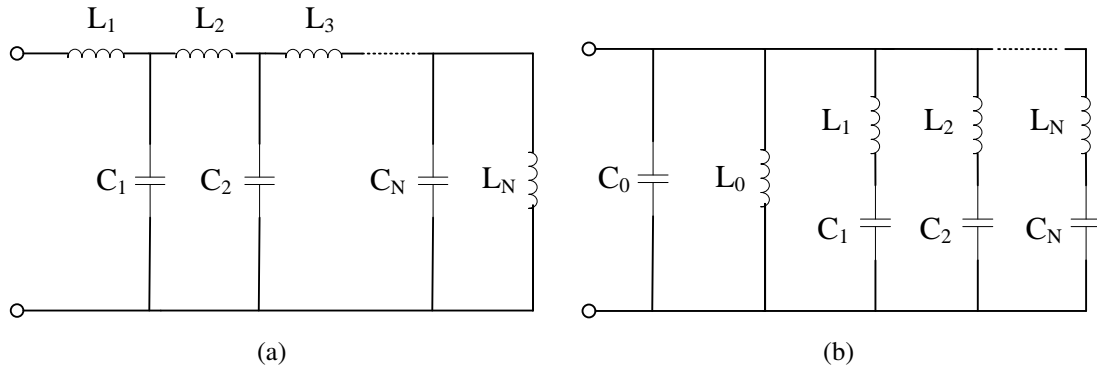
Figure 2.13: Aggregate impedance model. (a) Cauer model. (b) Foster model.
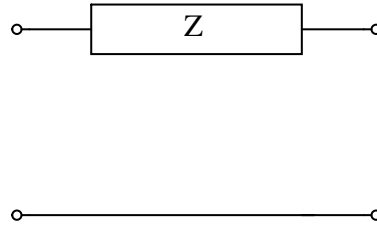
Figure 2.14: Lumped impedance model.

2.2. The Relationship between Power Electronics and Power Quality

In general, customers desire for utilities to provide an undistorted, single-frequency voltage waveform. In practice, however, system voltages become distorted as the result of short-term transient phenomena (i.e. motor starting, lightning, etc.) and steady-state effects (i.e. non-linear loads and system resonances). In the context of this thesis, a key power-quality issue is that of harmonics introduced by power electornic loads. In general, power electronics are non-linear, meaning they will produce harmonic currents. As these currents flow through the equivalent system impedance, a corresponding harmonic voltage drop is produced. This causes distorion in the point of common coupling to which multiple loads are connected. As networks become more dependent on power electronic loads, this is an issue that must be carefully considered and addressed.

This section provides a brief overview relevant to the interaction between power electronics and power systems. If first reviews basic concepts associated with harmonic cur-

rents in power systems. It then describes how power electronics generate these harmonic currents.

2.2.1. Harmonics in Power Systems

IEEE Standard 519-1992 [13] defines a harmonic component in an AC power system as a sinusoidal component of a periodic waveform that has a frequency equal to an integer multiple of the fundamental frequency of the system (i.e. 50/60Hz). In many cases, loads generate other signals with frequencies that are non-integer multiples of the fundamental. Components with frequencies below the fundamental are known as subharmonics. Other non-integer frequency multiples are referred to as interharmonics [21]. In Chapter 3 of this thesis, these interharmonics are used to estimate the system impedance.

Harmonic problems in power systems are generally analyzed using the principal of superposition. Non-linear elements such as power electronics are viewed as current sources at each appropriate harmonic frequency [21, 19]. These currents flow through power lines, transformers, and other components, all of which have associated impedances. The result is that harmonic voltages are produced at various busses throughout the network. The resulting distortion causes even linear loads to draw harmonic currents. A complete analysis of the so-called harmonic pollution problem becomes difficult because the system impedance serves as a mechanism through which a complex feedback system is created.

The susceptibility of a network to harmonic distortion has a significant depenedence upon system impedance. So-called stiff systems with low impedances are far less susceptible to harmonic issues. Power system analysts often use a different term, namely the fault current I_f, to describe the stiffness of a network. This quanity is the ratio of the rated system votlage to the magnitude of the system impedance. It is thus the current that would flow into a short circuit. IEEE Standard 519 provides limits on the allowable harmonic distortion in terms of the ratio of the fault current to the rated load current.

Total harmonic distotion is a typical measure of the power quality reduction caused by

harmonics. The THD for voltage and current waveforms are respectively defined as

$$THD_V = \frac{\sqrt{\sum_{h=2}^{\infty} V_{hrms}^2}}{V_{1rms}} \times 100\%, \tag{2.27}$$

and

$$THD_I = \frac{\sqrt{\sum_{h=2}^{\infty} I_{hrms}^2}}{I_{1rms}} \times 100\%. \tag{2.28}$$

In these equations, the subscript $1rms$ refers to the rms value of the fundamental component and the subscript $hrms$ refers to the rms value of the harmonic component of order h. THD values are an indicator of the total level of harmonic distortion and hence the severity of waveform distortion. These factors are often used to express the lim,its of distortion that a utility is willing to accept from a given customer load. IEEE Standard 519 imposes limits on these quanities. For supplies at 69kV and below, the voltage limit at any individual harmonic is 3% of the fundamental and the THD is limited to 5%.

2.2.2. Power Electronics as a Primary Source of Harmonic Currents

Most power electronic elements connected to the AC power sytstem contain a rectifier. Examples include computer power supplies, motor drives, arc furnaces, arc welders, flourescent ballasts, battery chargers, and cycloconverters. Figure 2.15 shows an example schematic diagram relevant in a single-phase system. A front-end bridge rectifier BR_1 and a DC bus capacitor C_1 supply a switch-mode power supply. The example supply shown in Figure 2.15 includes a forward converter [25], which includes a high-frequency isolation transformer, which thus avoids the need for a bulky power-line transformer at the front end. Such a topology is used in the ubiquitous ATX power supply found in most desktop PCs.

Rectifier circuits such as the one shown in Figure 2.15 are typically analyzed using the method of assumed states [53]. Current will only flow into the rectifier whenever the AC-side voltage is greater than the voltage across C_1 or when the AC-side votlage is more
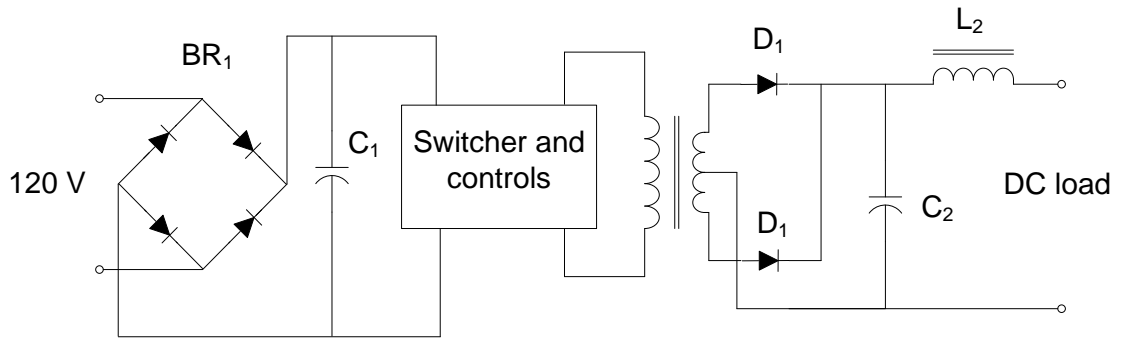
Figure 2.15: Simplified block diagram of a switching mode power supply.

negative than the additive inverse of the voltage across C_1. The resulting current waveform asppears as shown in Figure 2.16. A Fourier analyis shows that this waveform contains all odd harmonics with amplitudes that are inversely proportional to the harmonic number [25]. Similar analyses can be included for phase-controlled rectifiers and various three-phase topologies [25]. In system analyzes, these harmonics are viewed as current sources [25].

(a)

(b)
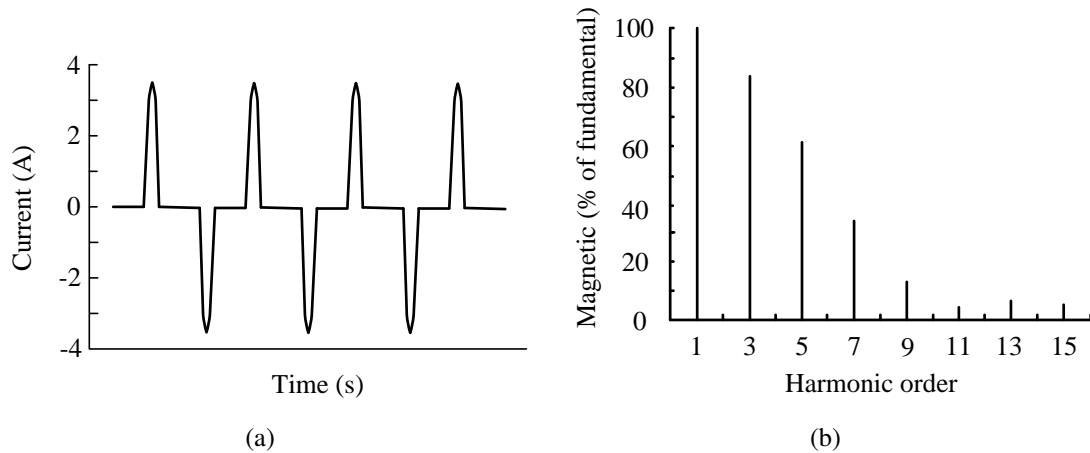
Figure 2.16: (a) Input current to front end rectifier. (b) Harmonics content
of the input current.

Harmonic currents generated by power electronics can be mitigated through the use of either passive or active methods. In many low-cost components, no such strategies are employed. In modern power electronic based power distribution systems, active methods

are extremely common. The effects of these are considered in more detail below.

2.3. Stability Analysis of Grid Connected Converters

The power quality issues identified above led to the development of techniques for mitigating harmonic source injection. Passive filter techniques are simple, but the weight and cost of the components can be high. In modern power supplies, active wave shaping is commonly used to force the input current to be sinusoidal. In microgrids and power electronic based distribution systems, most of the power electronic loads feature such active interfaces. Additionally, these systems also contain actively controlled sources. In such cases, oscillation can result from the interaction between the converter and the equivalent system impedance that it sees. Stability is one of the most fundamental issues in PEBDS [54, 55, 56, 23, 57, 58], and it is thus analyzed in detail here. In the context of this thesis, the emphasis is placed on the dynamic nature of the system. The methods proposed in Chapter 4 for adaptive compensation proceed from the discussions presented here. To understand the stability problem, consider the PEBDS feeder shown in Figure 2.17. Additional modules that are not shown in the figure may be connected to the feeder as time advances. Each module is designed individually based on standalone stability requirements. These loads tend to have tightly regulated output stages and high efficiencies, meaning that they appear to the network as constant power loads (CPLs) at low frequencies. Thus, if the input voltage increase by some factor, the input current will correspondingly decrease by some amount that maintains the overall power throughput. The result is an incrementally negative impedance. The interaction between the system impedance with this negative input impedance can lead to instability [59, 26, 57, 60]. In PEBDS, where many CPLs may connect and disconnect from the system, negative impedance instability can be particularly troubling. This section reviews the corresponding modeling issues deemed relevant to this thesis.
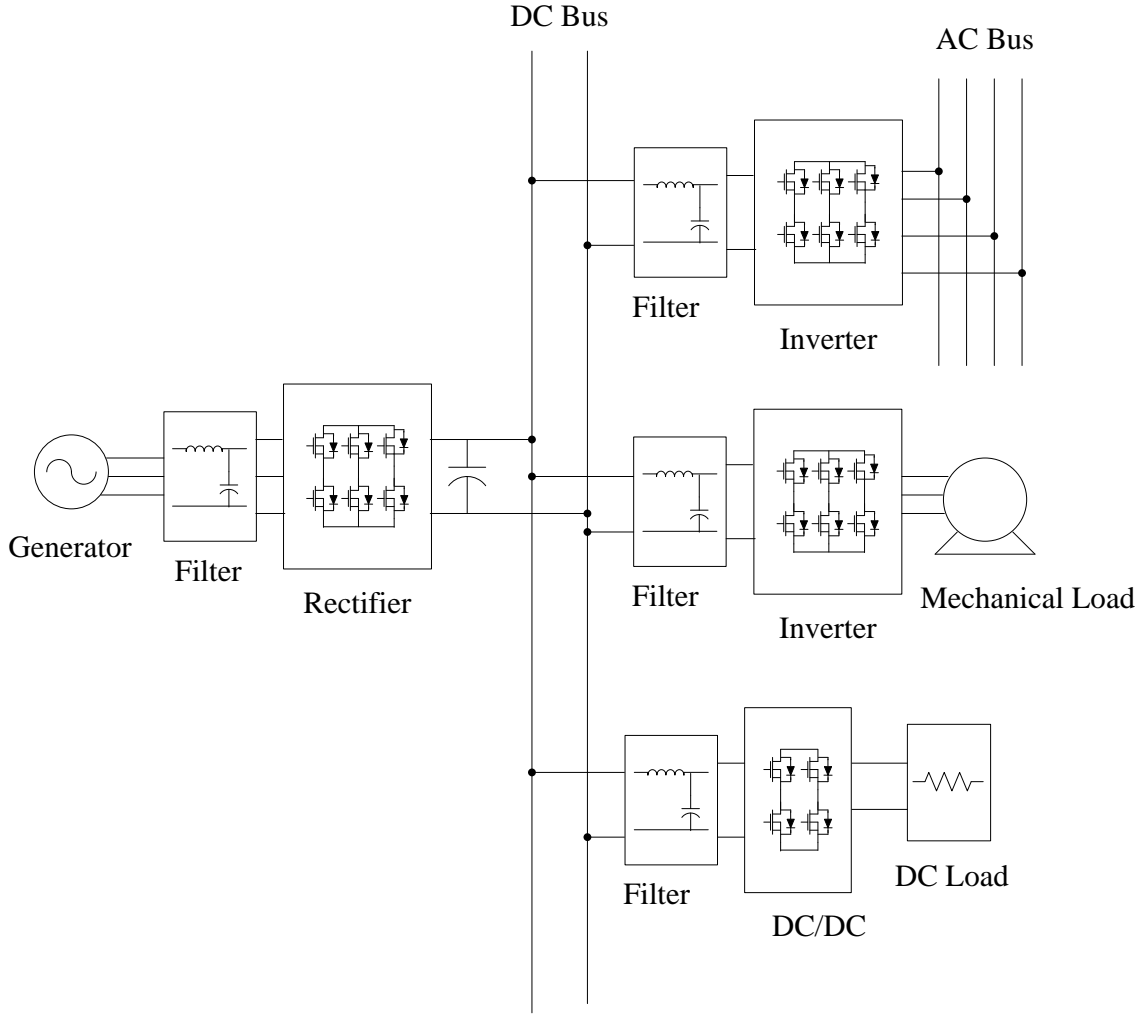
Figure 2.17: A representative of power electronics based distributed system.

2.3.1. Constant Power Loads and Negative Impedance

Figure 2.18(a) shows a DC/DC buck converter. A tight loop regulates the output at high switching frequency so that a constant output voltage is provided. If the converter has unity efficiency and the load current does not change, then P_{in} is constant determined by

$$P_{in} = vi \approx P_{out} = constant. \tag{2.29}$$

At low frequency, the switch-mode converter acts as a 'DC transformer' having some voltage conversion ratio μ. The relationship from input voltage to output voltage and from

(a)

(b)
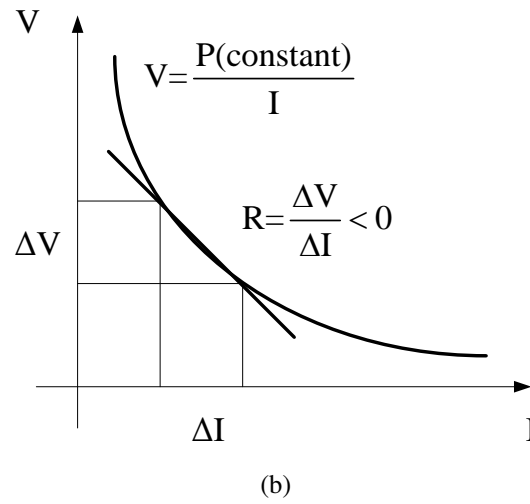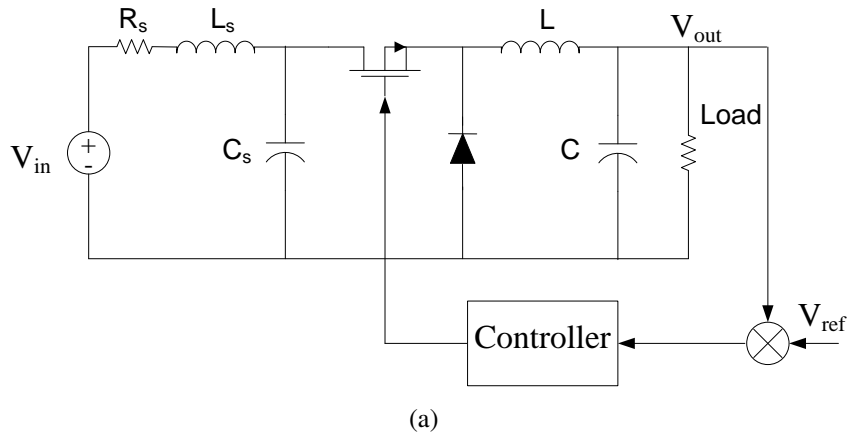
Figure 2.18: (a) DC/DC buck converter schematic with input filter.
(b) Negative incremental impedance.

input current to output current is thus

$$\mu = \frac{V_{in}}{V_{out}} = \frac{I_{out}}{I_{in}}. \tag{2.30}$$

When a small perturbation is applied to the input voltage, the differential change in the input power may be expressed as

$$P + dP = (V_{in} + dv_{in})(I_{in} + di_{in}). \tag{2.31}$$

By neglecting the second order terms we can express the incremental change in power as

$$dP = V_{in}di_{in} + I_{in}dv_{in}. \tag{2.32}$$

Assuming that the converter is tightly regulated, the converter should return to its qperating point; thus, dP should become zero, i.e.

$$V_{in}di_{in} + I_{in}dv_{in} = 0. \tag{2.33}$$

This relationship defines the incremental impedance which is

$$R_{in} = \frac{dv_{in}}{di_{in}} = -\frac{V_{in}}{I_{in}}. \tag{2.34}$$

Similar arguments can be used to show that xonstnat power loads connected to AC systems through rectifiers also have incrementally negative impedances. In both DC and AC systems, this incremental negative impedance only applied in transient conditions at low frequency. In steady state, the impedance is always positive.

2.3.2. Negative Impedance Instability

The negative impedance phenomenon described above can cause problems when connected to a real network with a non-zero impedance. Certain sources and line conditioners may interact with a power electronic component in such a way that instability results. This instability can affect other loads on the network and potentially cause component damage. The standard analytical procedure is the so-called impedance criterion first applied by Middlebrook in 1976 [26] when he considered the interactions between a DC/DC converter and its input-side EMI filter. This approach analyzes stability using the input impedance of each load, and the apparent output impedance of the network as seen from the load terminals. Small signal stability analysis around any operating point proceeds using the simplified
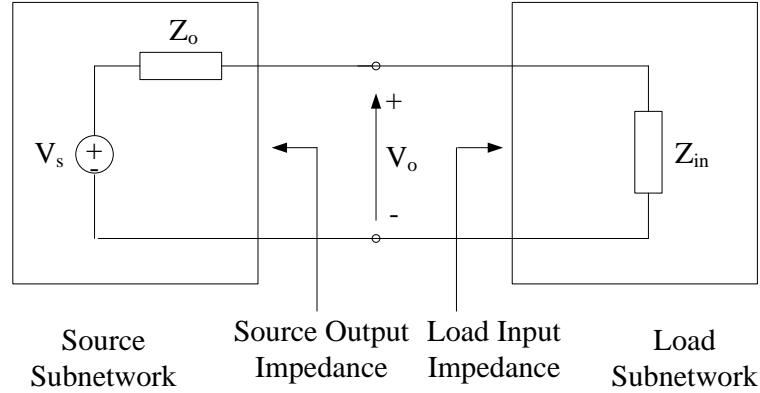
Figure 2.19: Source input and load output impedance defined.

model shown in Fig 2.19. The system is said to have an equivalent output impedance $Z_o(s)$ and the load has an equivalent input impedance $Z_{in}(s)$. The source load interaction is modeled from the voltage divider relationship

$$\frac{V_0}{V_S} = \frac{Z_{in}}{Z_0 + Z_{in}} = \frac{1}{1 + Z_0 Y_{in}}.$$ (2.35)

The stability of this system is governed by the loop gain $T_m(s) = Z_o/Z_{in}$. The simplest approach to assuring stability is to assume that the magnitude of Z_{in} is always much larger than the magnitude of Z_o. This rule is widely known, but it can lead to extremely conservative and costly designs. In general, little is known about the two impedances in question, and both are subject to variations as additional converters are connected in parallel across the bus. This makes it difficult to specify how large $|Z_{in}|$ should be relative to $|Z_o|$ in order to achieve a satisfactory level of stability. In many cases, a large capacitor across the converter input terminals is sufficient to compensate for the destabilizing effects of the negative impedance characteristic.

Other approaches have been considered to avoid the extreme conservatism of setting $|Z_{in}| \gg |Z_o|$. Figure 2.20 shows a situation in which the magnitude of Z_o exceeds that of $Z_i n$ over a certain frequency range. Assuming that the converter is stable prior to connection to the network, then the stability condition at the two overlap frequencies can be defined as
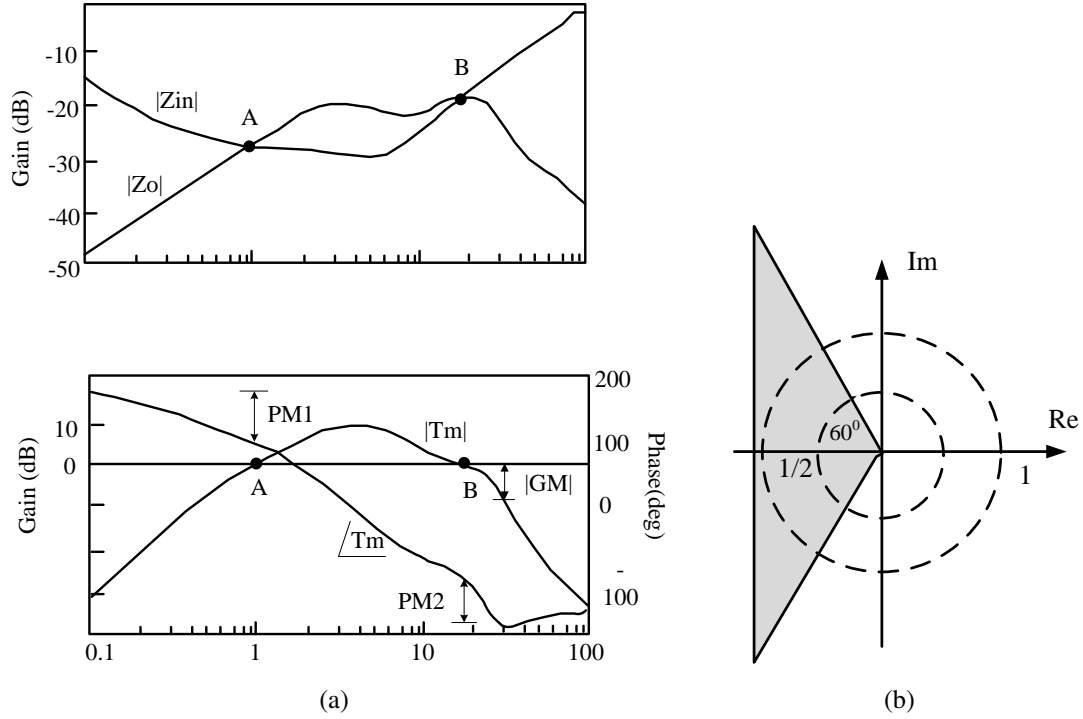
Figure 2.20: Impedance overlap at interface. (a) Impedance comparison.
(b) Bode plot of open loop Tm.

follows

$$|Z_0| - |Z_{in}| > -GM_s(dB), -180^0 + PM_{2s} < \angle Z_0 - \angle Z_{in} < 180^0 - PM_{1s}. \qquad (2.36)$$

Where *GM* is the gain margin and *PM*1 and *PM*2 are the phase margins at frequencies A and B, respectively. Using this information, various stability criteria have been considered. One example is the Wildrick criterion, which assumes that *PM*1 and *PM*2 are to be the same, 60 degrees. In addition, the gain margin is set to 6dB. This selection is less conservative than that proposed by Middlebrook, but it is still relatively robust given the large margins. Figure 2.21 summarizes four common criteria found in the literature. Each defines a so-called forbidden region that includes the (-1,0) point in the complex plane. Avoidance of this region guarantees no encirclements, and thus sufficient margin for stability.
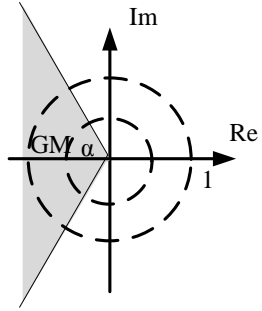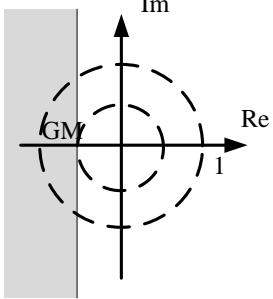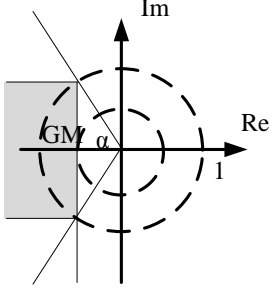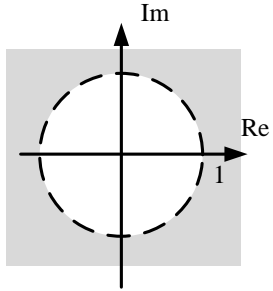
Method 1		$\left\|Z_0\right\| - \|Z_{in}\| > -GM$ $\left\|\angle Z_0 - \angle Z_{in}\right\| < 180^0 - \alpha$
Method 2		$Re\left(\dfrac{\|Z_0\|}{\|Z_{in}\|}\right) > -\dfrac{1}{GM}$
Method 3		$\left\|Im\left(\dfrac{Z_0}{Z_{in}}\right)\right\| > -\dfrac{\tan(\alpha)}{GM}$ or $Re\left(\dfrac{\|Z_0\|}{\|Z_{in}\|}\right) > -\dfrac{1}{GM}$
Method 4		$\dfrac{\|Z_0\|}{\|Z_{in}\|} < 1$

Figure 2.21: Comparison of forbidden region methods.

2.3.3. Complications in Power Electronic Based Distribution Systems

Avoidance of negative impedance instability in PEBDS can be challenging. In these systems, multiple sources and loads are connected to a bus through various power electronic interfaces. Figure 2.22 shows a typical example. In this case, the stability of each individual component-system interaction is governed by its own impedance facing the network and the impedance that it sees looking into the network. From the perspective of the k-th load, for instance, the closed-loop transfer function is

$$\frac{v_{ink}}{v_{0k}} = \frac{1}{1 + Z_{ok}Y_{ink}} = h_k.$$

(2.37)

The challenge is that Z_{ok} consists of the parallel combination of the impedances seen looking into each currently operating component. This impedance is likely to change over time, and is thus highly variable. Various forbidden-region criteria could be used to help achieve stability, but these become difficult to apply if one cannot determine the worst-case scenario for the impedances. It is this problem that motivates consideration of adaptive controllers such as the one presented in Chapter 4 of this thesis.
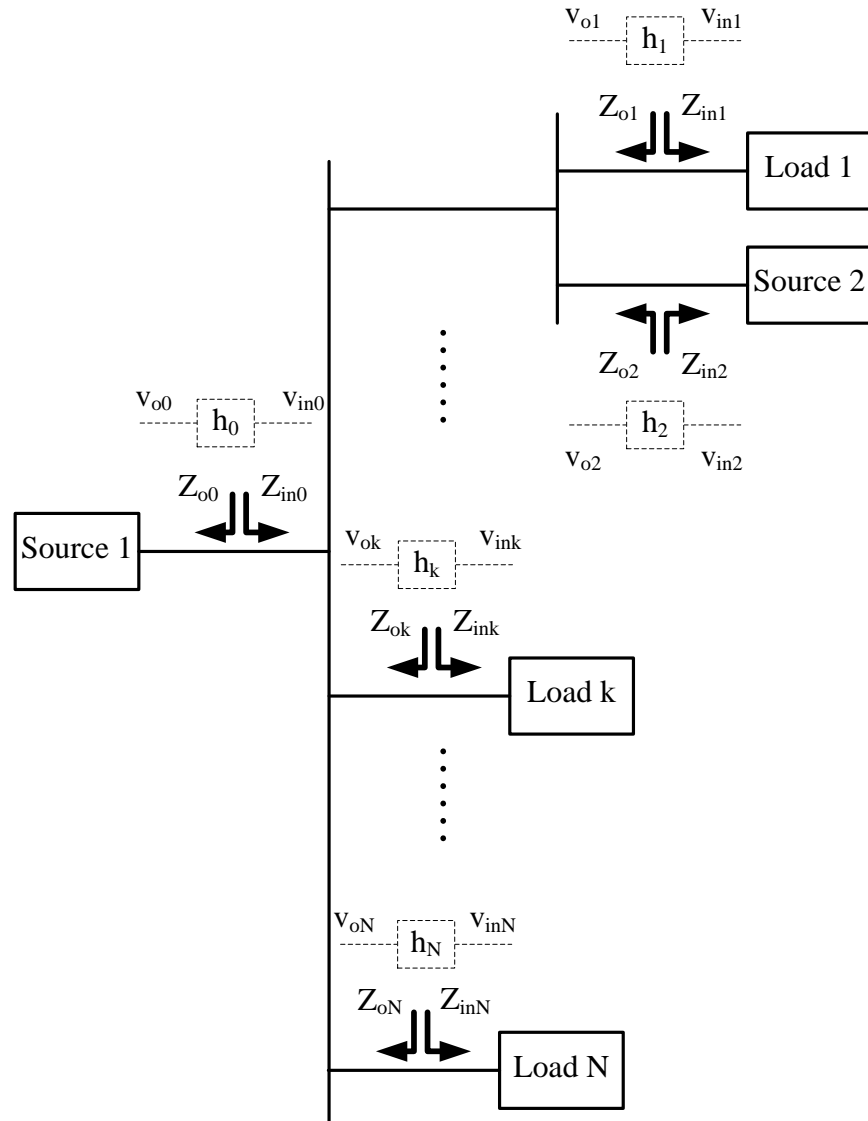
Figure 2.22: Typical power electronics based distributed power system and interactions between components.

CHAPTER 3: A MINIMALLY INTRUSIVE ONLINE GRID IMPEDANCE
ESTIMATION METHOD

This chapter presents a minimally intrusive method for estimating grid impedance in
energized systems. The method uses naturally occurring interharmonic signals generated
by operational loads. Examples include signals produced by motor eccentricities and vi-
brations. These waveforms are, in general, significantly smaller than the fundamental com-
ponent of the current and its principal integer harmonics. Previous research has shown
that traditional approaches such as the Fast Fourier Transform cannot accurately measured
the amplitude and phase of such relatively small signals. These issues are overcome by
viewing the small injected signals as waveforms transmitted over a noisy communications
channel. A detector based on the maximum likelihood principle estimates key parameters
of the injected signals and then computes estimates of the real and imaginary parts of the
impedance. Both simulation and experimental results are presented. The signals used for
measurement in both the laboratory and in the field have an amplitude of approximately
10mA.

3.1. Introduction

The equivalent impedance of the electric power system directly impacts power quality
[61], electrical safety [62], and component performance [38, 63]. Many issues arise when
large or distorted currents are drawn through this impedance. Interactions between the sys-
tem and non-linear loads, for instance, produce steady-state voltage distortion throughout
the network [61, 64]. Short-term events such as faults and load-induced transients cause
voltage sag [61]. All of these activities ultimately affect and potentially degrade the per-
formance of various loads connected throughout the system [61, 64]. In the case of faults,

line impedance limits the magnitude of the current and thus the energy released during any resulting arc flash [62, 39]. Equivalent line impedance also impacts the behavior of grid-connected power converters. Certain impedance values can degrade and even destabilize grid-connected inverters [65, 66] and active power conditioners and regulators [67, 63]. In power-electronic systems used for distributed generation, line impedance measurements are used to detect faults and initiate isolation [68].

In applications requiring knowledge of grid impedance, it can be helpful to have a priori information. Short-circuit ratios at the point of common coupling provide one mechanism for determining fundamental-frequency impedance. In many scenarios, however, such information is unavailable and actual installation details may differ significantly from design specifications. Another issue is that fundamental-frequency values are often insufficient [63, 69]. Impedance is, of course, frequency dependent, and capacitive effects can introduce high-frequency resonances and other phenomena that can be highly detrimental to load performance and power quality [63, 69]. Another challenge is that line impedance varies with time, and the value depends on system configuration, loading, and temperature. Power-electronic systems in microgrids, which are routinely connected and disconnected from the larger power system, are particularly sensitive to these variations [68].

The frequency-dependent and time-varying nature of grid impedance motivates the need for real-time estimation. Various approaches have been proposed, and are generally grouped into two categories. In the first of these, which are termed active methods, a user-generated disturbance systematically perturbs the grid and the impedance is estimated from the resulting measurements [40]. One strategy is to inject specific sinusoidal currents, either at a single frequency near the fundamental or over a broad band [38, 70, 39, 43]. Transient perturbations can also be used [41, 71, 42, 72, 73]. These are introduced by connecting various linear and non-linear loads to the system. Impedance can also be estimated by creating specific variations in active and reactive power [74, 67]. Passive methods for impedance estimation, on the other hand, use existing non-fundamental signals within the

power system [40, 75, 44]. Despite the fact that these approaches are minimally intrusive, they can be difficult to implement because the amplitude of the available distortion tends to be small and the repetition rate is low [40, 68, 38].

This chapter presents a procedure that reliably estimates grid impedance using existing interharmonic signals within the power system. Natural load-generated disturbances are the key sources of distortion in this method. Common examples include the various interharmonic signals generated by induction motors [76] and power converters [77]. In the case of induction motors, for instance, signals are generated by effects such as eccentricities, vibrations, and load imbalances [76]. These signals typically fall at non-integer multiples of the fundamental frequency, and have amplitudes that are significantly smaller than the fundamental component and its principal harmonics. When such small signals are used for impedance estimation, it can be difficult to resolve their amplitude and phase with sufficient accuracy. These limitations are clearly demonstrated in [38]. Measurement difficulties are overcome in this paper by applying concepts used in communications systems. Small load-generated current signals are viewed as waveforms transmitted over a noisy channel. These "transmissions" are then recovered using a detector based on the maximum likelihood principle [78, 79]. Experimental results make use of naturally occurring signals with an amplitude of approximately 10mA, which is just within the rated accuracy of the sensors employed. The proposed approach is minimally intrusive in the sense that it does not degrade power quality or require special injection sources.

The chapter begins with a discussion of the utility model and the measurement procedure. The analytical approach used to implement the measurement technique, which relies on maximum likelihood estimation (MLE) is then described. Simulation results and experimental results from both a laboratory prototype and a field test are also shown.

3.2. System Model and Measurement Approach

To estimate grid impedance using point-of-load power distortion, we consider a single-phase line-to-neutral connection to the electric utility as shown in Figure 3.1. The source $v_s(t)$ might represent the voltage present at the secondary of a distribution transformer. In general, this source contains a fundamental term as well as various harmonics and interharmonics. This source can thus be modeled as

$$v_s(t) = \sum_{k=1}^{\infty} V_k \sin\left(k\omega t + \phi_k^v\right) + v_{int}(t),\tag{3.1}$$

where the fundamental frequency is ω, ϕ_k^v is the phase shift at the kth harmonic, and $v_{int}(t)$ represents the series combination of any interharmonic and subharmonic sources.
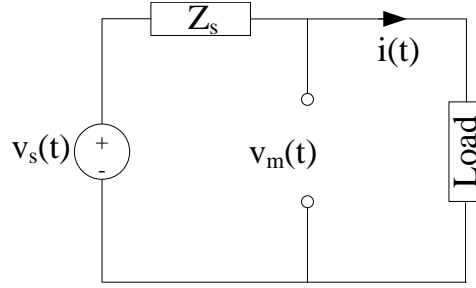
Figure 3.1: A distribution-level model of the electric utility.

Loads are connected to $v_s(t)$ through a complex impedance Z_s representing the combined effects of transformers, cabling, protection devices, and other elements. In distribution networks, the reactive component of this impedance tends to be inductive at low frequencies near the fundamental [38, 68, 42, 63, 43, 69]. In general, however, this impedance will change with frequency and the reactive component may ultimately become capacitive at higher frequencies because of the effects of cabling, power-factor correction, filtering, and other elements. The current drawn through this impedance by the load is of the form

$$i(t) = \sum_{k=1}^{\infty} I_k \sin\left(k\omega t + \phi_k^i\right) + i_{int}(t),\tag{3.2}$$

where ϕ_k^i is the phase shift at the kth harmonic and $i_{int}(t)$ represents any sub or interharmonics.

To estimate the impedance Z_s, we assume that the load draws an interharmonic current of the form

$$i_c(t) = I_c \sin(\omega_c t + \phi_c^i),$$ (3.3)

where ω_c is near but not equal to the fundamental frequency. This signal can be either natural (i.e. an eccentricity-related signal produced by an induction machine) or specially generated (i.e. a specific signal produced by a power-electronic load). Under steady-state conditions, superposition can be applied to simplify the circuit model as shown in Figure 3.2. Note that the load is modeled as a current source with a single sinusoidal component, and that the upstream voltage is

$$v_{s,c}(t) = V_{S,C} \cos(\omega_c t + \phi_c^v).$$ (3.4)

The lumped elements R_c and L_c represent the equivalent real and reactive components of the line impedance at ω_c, and are thus defined as

$$R_c \equiv \mathrm{Re}\{Z_s|_{\omega_c}\}$$ (3.5)

and

$$L_c \equiv \frac{\mathrm{Im}\{Z_s|_{\omega_c}\}}{\omega_c}$$ (3.6)

In general, these definitions remain valid throughout the neighborhood of ω_c; thus, if ω_c is close to the fundamental, R_c and L_c should approximate the impedance of interest. This approach is used in various references, albeit with much larger values of I_c [38, 70]. For impedance estimation to be effective, $v_{s,c}(t)$ should be negligible. This can be determined via spectral analysis prior to the connection of the load, and it is issue that has not been found to be problematic in the field.
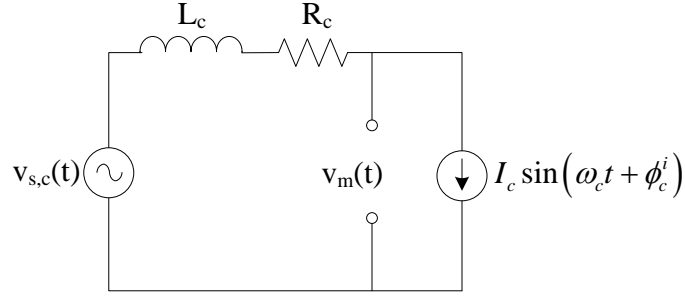
Figure 3.2: A simplified distribution-level model applicable at the frequency ω_c.

If $i_c(t)$ is known and $v_{s,c}(t)$ is negligible, then Figure 3.2 suggests that measurement of R_c and L_c is relatively straightforward. In practice, however, measurement can be difficult because the terminal voltage contains numerous components several orders of magnitude larger than $i_c(t)$. Measurement becomes even more challenging if the user does not have explicit control over $i_c(t)$, which is the case if the signal is naturally generated. Figure 3.3 shows a process that overcomes these problems. This approach is adapted from radar applications in which one seeks to detect a sinusoidal signal transmitted over a noisy channel. Note that the voltage measured at the point-of-load is first mixed with the current $i_c(t)$. For the moment, we assume that $i_c(t)$ is known and that $v_m(t)$ has the form

$$v_m(t) \;=\; \sum_{h=1}^{\infty} V_h \sin\left(h\omega t + \phi_h^v\right) \;+\; \sum_{n=1}^{\infty} V_n \sin\left(\omega_n t + \phi_n^v\right) \;-\; R_c i_c(t) \;-\; L_c \frac{di_c}{dt}. \quad (3.7)$$

Note that the first term in Eq. 3.7 contains components at integer multiples of the fundamental, while the remaining terms represent both source-side distortion and impedance drops at all other frequencies. Only the relevant impedance drops (i.e. those at ω_c) have been written separately. Using Eq. 3.3, $v_m(t)$ expands to become

$$v_m(t) = \sum_{h=1}^{\infty} V_h \sin\left(h\omega t + \phi_h^v\right) + \sum_{n=1}^{\infty} V_n \sin\left(\omega_n t + \phi_n^v\right)$$

$$- R_c I_c \sin(\omega_c t + \phi_c^i) - \omega_c L_c I_c \cos(\omega_c t + \phi_c^i). \quad (3.8)$$

This signal is mixed with $i_c(t)$ and integrated over a measurement window of length T_m to
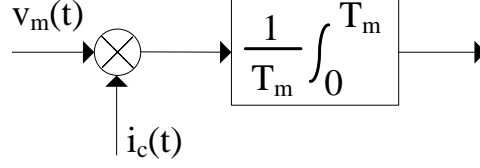
Figure 3.3: Proposed measurement process. $v_m(t)$ is the measured line voltage, and $i_c(t)$ is the interharmonic signal of interest.

yield

$$
\frac{1}{T_m} \int_0^{T_m} v_m(t) i_c(t) dt = \frac{1}{T_m} \int_0^{T_m} \sum_{h=1}^{\infty} V_h I_c \sin(h\omega t + \phi_h^v) \sin(\omega_c t + \phi_c^i) dt
$$

$$
+ \frac{1}{T_m} \int_0^{T_m} \sum_{n=1}^{\infty} I_c V_n \sin(\omega_n t + \phi_n^v) \sin(\omega_c t + \phi_c^i) dt - \frac{R_c I_c}{T_m} \int_0^{T_m} \sin^2(\omega_c t + \phi_c^i) dt
$$

$$
- \frac{\omega_c L_c I_c}{T_m} \int_0^{T_m} \cos(\omega_c t + \phi_c^i) \sin(\omega_c t + \phi_c^i) dt. \quad (3.9)
$$

To simplify the detector output in Eq. 3.9, special consideration must be given to the choice of the measurement window. To see this, consider each of the terms in the two infinite series. Note that each integrand in these summations has the general form $\sin(x)\sin(y)$. Using an appropriate trigonometric identity (i.e. $\sin(x)\sin(y) = \frac{1}{2}[\cos(x-y) - \cos(x+y)]$), each integral expands into two terms of the form

$$
\frac{1}{2T_m} \int_0^{T_m} \cos(\alpha t + \phi) dt, \quad (3.10)
$$

where α is one of the following choices: $h\omega - \omega_c$, $h\omega + \omega_c$, $\omega_n - \omega_c$, or $\omega_n + \omega_c$. When evaluated, this integral becomes

$$
\frac{1}{2T_m} \int_0^{T_m} \cos(\alpha t + \phi) dt = \frac{1}{2\alpha T_m} [\sin(\alpha T_m + \phi) - \sin(\phi)]. \quad (3.11)
$$

Note that this result approaches zero as the measurement window becomes much larger than the period of the waveform (i.e. $T_m \gg 2\pi/\alpha$). By imposing this constraint for all α,

we can thus simplify the correlator output as follows

$$\frac{1}{T_m}\int_0^{T_m} v_m(t)\,i_c(t)dt \approx -\frac{R_cI_c}{T_m}\int_0^{T_m}\sin^2(\omega_c t+\phi_c^i)dt - \frac{\omega_c L_c I_c}{T_m}\int_0^{T_m}\cos(\omega_c t+\phi_c^i)\sin(\omega_c t+\phi_c^i)dt.$$
(3.12)

To further reduce Eq. 3.12, we note that the first integral on the right-hand side becomes

$$\frac{R_cI_c^2}{T_m}\int_0^{T_m}\sin^2(\omega_c t+\phi_c^i)dt = \frac{R_cI_c^2}{2} + \frac{R_cI_c^2}{T_m}\int_0^{T_m}\cos(2\omega_c t+2\phi_c^i)dt \qquad (3.13)$$

and that the second integral on the left-hand side becomes

$$\frac{\omega_c L_c I_c^2}{T_m}\int_0^{T_m}\cos(\omega_c t + \phi_c^i)\sin(\omega_c t + \phi_c^i)dt = \frac{\omega_c L_c I_c^2}{T_m}\int_0^{T_m}\sin(2\omega_c t + 2\phi_c^i)dt. \quad (3.14)$$

Using the same arguments presented previously, the integrals in both Eq. 3.13 and Eq. 3.14 also approach zero if $T_m \gg \frac{2\pi}{\omega_c}$. We are thus left with the following simple result

$$\frac{1}{T_m}\int_0^{T_m} v_m(t)\,i_c(t)dt \approx \frac{1}{2}R_cI_c^2.$$
(3.15)

Equation 3.15 provides a means to estimate R_c. Via similar logic, one can show that L_c is estimated by mixing $v_m(t)$ with the a signal in quadrature with $i_c(t)$, i.e.

$$\frac{1}{T_m}\int_0^{T_m} v_m(t)\,I_c\cos\left(\omega_c t + \phi_c^i\right)dt \approx \frac{1}{2}\omega_c L_c I_c^2.$$
(3.16)

Both of these results clearly rely on appropriately-sized measurement windows. A careful analysis shows that T_m should be much longer than the period of the lowest frequency signal to be integrated in Eq. 3.9. As a result of the mixer in Figure 3.3 this frequency is the one whose frequency is nearest to ω_c. Spectral analysis may thus be required to determine either the appropriate measurement window or the need to select a different measuring signal. In practice, three second measurement windows have been used to estimate the impedance at

or near the fundamental and several harmonics. No problems have been observed when applied in an actual distribution system.

Computation of the terms in Eqs. 3.15 and 3.16 is relatively straightforward if $i_c(t)$ is known exactly. Using either analog or digital techniques, one would mix $i_c(t)$ with $v_m(t)$ and integrate. Recall, however, that we are interested in using a signal whose amplitude, phase, and frequency are all outside of our control and are thus, in general, unknown. One solution is to simply measure $i_c(t)$. As with any coherent measurement problem, however, precise knowledge of the phase angle is critical to the distinct resolution of the real and imaginary parts [80]. Synchronization is not an option here since $i_c(t)$ is deliberately several orders of magnitude smaller than the fundamental. In fact, we typically have focused on signals with amplitudes nearing the accuracy of the employed sensors ($\tilde{1}$0mA), which is 3 to 4 orders of magnitude smaller than the fundamental. The parameters of $i_c(t)$ must thus be estimated and used to generate a test signal. Various parameter estimation approaches can be used, and the most typical employ the FFT or the periodogram [81, 82]. In general, these approaches have been found to yield modestly accurate estimates of the magnitude and frequency, but have failed to provide adequate estimates of the phase. This sensitivity to phase estimates is explored in a later section. To determine the parameters of $i_c(t)$ with sufficient accuracy, we thus turn to a different approach based on maximum likelihood estimation (MLE) [78]. This method is described in the next section.

3.3. Parameter Estimation for Small Sinusoidal Signals

To estimate the parameters of the small interharmonic signal $i_c(t)$, we turn again to a concept often applied in signal-detection theory. In this case, we view $i_c(t)$ as a signal that has been generated by the load and transmitted over a noisy communications channel, i.e. the power system. The received waveform is thus the signal measured by the current transducer. We consider the signal received over the time interval $(0, T_m)$. In general, this

signal can be written as

$$r(t) = i_i(t) + i_c(t) + n(t), \qquad (3.17)$$

where $i_c(t)$ is the signal of interest, $i_i(t)$ is a signal consisting of all of the other components of the current, and $n(t)$ is random measurement noise. Note that this noise is assumed to be zero-mean Gaussian with a variance $N_0/2$. As in signal-detection theory, we consider two possible conditions at the receiver. These are expressed mathematically as the hypotheses H_0 and H_1, which are

$$H_0 : r(t) = i_i(t) + n(t) \qquad (3.18)$$

$$H_1 : r(t) = i_i(t) + i_c(t) + n(t). \qquad (3.19)$$

Note that H_0 is the null condition and thus assumes that $i_c(t)$ has not been transmitted; hypothesis H_1 assumes that it has.

In detection theory, one seeks to determine which hypothesis is true given measurements of $r(t)$ over the interval $(0, T_m)$. In the simplest case, one develops a decision rule for a particular hypothesis using the probability densities $p_0(r)$ and $p_1(r)$ for the observations $r(t)$ [78, 83]. The subscripts in these expressions denote the fact that each is conditioned on either H_0 or H_1 being true. These densities are typically referred to as likelihood functions [78, 83]. In this case, the densities also depend upon unknown signal parameter values, which include the amplitudes, frequencies, and phases of all of the various sinusoidal components of the current. In general, we consider each parameter to be a random variable whose value is constant over the measurement window. Thus, we must define conditional likelihood functions for both hypotheses [78, 83]. These are

$$p_1(r|I_1, f_1, \varphi_1) = F \exp\{-(1/N_0) \int_0^{T_m} [r(t) - (i_i(t) + i_c(t))]^2 dt\} \qquad (3.20)$$

and

$$p_0(r|I_0, f_0, \varphi_0) = F \exp\{-(1/N_0) \int_0^{T_m} [r(t) - i_i(t)]^2 dt\}, \tag{3.21}$$

where F is an undetermined constant [78]. Note that these densities are conditioned on the values of the unknown parameters, which are expressed as the sets $I_1(I_c, I_0, I_1, ...)$, $I_0(I_0, I_1, ...)$, $f_1(f_c, f_0, f_1...)$, $f_0(f_0, f_1...)$, $\varphi_1(\phi_c, \phi_0, \phi_1, ...)$, and $\varphi_0(\phi_0, \phi_1, ...)$, respectively. For simplicity, the parameters associated with each hypothesis are aggregated and written as θ_0 for H_0 and θ_1 for H_1. The decision rule is to choose H_1 if

$$\frac{\int_{\theta_1} p_1(r|\theta_1) w_1(\theta_1) d\theta_1}{\int_{\theta_0} p_0(r|\theta_0) w_0(\theta_0) d\theta_0} \geq \lambda_0. \tag{3.22}$$

In Eq. 3.22, the functions $w_0(\theta_0)$ and $w_1(\theta_1)$ are the joint a priori probability density functions associated with θ_0 and θ_1, respectively. The integral in the numerator is an n-fold integration over the possible range of θ_1. A similar argument holds true for the denominator. In general, the constant λ_0 depends upon the available a priori knowledge.

In general, Eq. 3.22 is difficult to use as a decision rule because little is known about the distributions of the random parameters associated with each hypothesis. A typical solution is to use the maximum-likelihood principle. In that approach, one computes the generalized likelihood ratio (GLR), which is

$$\lambda(r) = \frac{\max_{\theta_1} \{p_1(r|\theta_1)\}}{\max_{\theta_0} \{p_0(r|\theta_0)\}}. \tag{3.23}$$

We then find the value of θ_1, call it $\hat{\theta}_1$, that maximizes $p_1(r|\theta_1)$, and similarly we find the value of θ_0, call it $\hat{\theta}_0$, which maximizes $p_0(r|\theta_0)$. The computation of parameter estimates under this approach is known as maximum-likelihood estimation. Ultimately, the estimates are used as if they were known, true values. We can thus rewrite the GLR as

$$\lambda(r) = \frac{p_1(r|\hat{\theta}_1)}{p_0(r|\hat{\theta}_0)}, \tag{3.24}$$

where both pdfs depend on the parameter estimates.

Using the result from Equation 3.24, we rewrite the GLR as

$$\lambda(r|\hat{I},\hat{f},\hat{\varphi}) = \frac{F\exp\{-(1/N_0)\int_0^{T_m}[r(t)-(\hat{i}_i(t)+\hat{i}_c(t))]^2 dt\}}{F\exp\{-(1/N_0)\int_0^{T_m}\left(r(t)-\hat{i}_i(t)\right)^2 dt\}} \qquad (3.25)$$

Note that this expression depends only upon the parameter estimates, which are considered to be known. After expanding and cancelling terms, this result becomes

$$\lambda(r|I,f,\varphi) = \exp\left\{-(1/N_0)\int_0^{T_m}[-2r(t)\hat{i}_c(t)+2\hat{i}_i(t)\hat{i}_c(t)+\hat{i}_c^2(t)]dt\right\}. \qquad (3.26)$$

Using the same arguments presented in Section 3.2, we know that the integral of $\hat{i}_i(t)\hat{i}_c(t)$ cancels over the interval $(0,T_m)$. Similarly, with $\hat{i}_c(t)$ of the form

$$\hat{i}_c(t) = \hat{I}_c\sin(2\pi\hat{f}_c t + \hat{\varphi}_c^i), \qquad (3.27)$$

we know that the integral of $\hat{i}_c^2(t)$ over the same window is $\hat{I}_c^2 T_m/2$. The GLR thus simplifies to

$$\lambda(r|\hat{I},\hat{f},\hat{\varphi}) \quad \approx \quad \exp\left(-\frac{\hat{I}_c^2 T_m}{2N_0}\right) \quad \times \quad \exp\left\{\frac{\hat{I}_c}{N_0}\int_0^{T_m} 2r(t)\sin\left(2\pi\hat{f}_c t + \hat{\varphi}_c^i\right)dt\right\}. \qquad (3.28)$$

Estimates for $\hat{I}_c$, $\hat{f}_c$, and $\hat{\varphi}_c$ are obtained by maximizing Eq. 3.28. For a given $\hat{I}_c$, Eq. 3.28 maximizes when the integral term maximizes. We thus analyze this term separately. This process simplifies if we use the definition

$$\int_0^{T_m} r(t)\sin\left(2\pi\hat{f}_c t + \hat{\varphi}_c\right)dt = s(\hat{f}_c). \qquad (3.29)$$

Note that $s(\hat{f}_c)$ can be rewritten as

$$s^2(\hat{f}_c) = p^2(\hat{f}_c) + q^2(\hat{f}_c) = \left[\int_0^{T_m} r(t)\sin 2\pi\hat{f}_c t\, dt\right]^2 + \left[\int_0^{T_m} r(t)\cos 2\pi\hat{f}_c t\, dt\right]^2 \quad (3.30)$$

where we have used the definitions

$$p(\hat{f}_c) = s(\hat{f}_c)\cos\hat{\varphi}_c = \int_0^{T_m} r(t)\sin 2\pi\hat{f}_c t\, dt \quad (3.31)$$

and

$$q(\hat{f}_c) = s(\hat{f}_c)\sin\hat{\varphi}_c = \int_0^{T_m} r(t)\cos 2\pi\hat{f}_c t\, dt. \quad (3.32)$$

A simple and efficient algorithm for maximizing Eq. 3.30 with respect to the frequency $\hat{f}_c$ is shown in the next section.

Estimation of the remaining parameters becomes trivial once $\hat{f}_c$ is known. The maximum likelihood estimate of $\hat{I}_c$ solves the equation

$$\frac{\partial\lambda(r|\hat{I},\hat{f},\hat{\varphi})}{\partial\hat{I}_c} = 0. \quad (3.33)$$

Using $\hat{f}_c$, this result is simply

$$\hat{I}_c = (2/T_m)\int_0^{T_m} r(t)\sin\left(2\pi\hat{f}_c t + \hat{\varphi}_c\right)dt = (2/T_m)\,s(\hat{f}_c). \quad (3.34)$$

Similarly, the maximum likelihood estimate of the phase $\hat{\varphi}_c$ solves the equation

$$\frac{\partial\lambda(r|\hat{I},\hat{f},\hat{\varphi})}{\partial\hat{\varphi}_c} = 0. \quad (3.35)$$

This result is

$$\hat{\phi}_c = \tan^{-1}\left\{\frac{\int\limits_0^{T_m} r(t)\cos 2\pi \hat{f}_c t\, dt}{\int\limits_0^{T_m} r(t)\sin 2\pi \hat{f}_c t\, dt}\right\} = \tan^{-1}\left\{\frac{q(\hat{f}_c)}{p(\hat{f}_c)}\right\}. \tag{3.36}$$

3.3.1. An Algorithm for the MLE Method

The parameter estimation method outlined above relies heavily on the value of $\hat{f}_c$ that maximizes Eq. 3.30. In communications theory, this value is traditionally determined using either brute-force methods or matched filter banks [78, 79]. Note that both the Newton-Raphson algorithm and the Quasi-Newton method are commonly used to reduce the calculation burden [84]. These methods, however, can still be computationally burdensome because the accuracy of the final estimate depends heavily upon the step size. The choice of a smaller increment thus becomes a key trade-off.

Because time is of the essence when measuring grid impedance, an efficient algorithm was developed to maximize Eq. 3.30. The motivation for this algorithm stems from the fact that one typically has a general sense of the the value of f_c based on certain a priori information about the load. In addition, it is clear that Eq. 3.30 is very similar in form to the evaluation of the continuous-time Fourier transform over a window T_m [80]. Equation 3.30 should thus take the form of a sinc function in the neighborhood of $\hat{f}_c$ and will have a single peak [80]. With this information, the search range can be narrowed significantly. Furthermore, it is true that any real number f can be represented in the form of a continued fraction using a power-series expansion [85]. For example, the frequency $f = 30.12345\text{Hz}$ can be expressed using the set of power-series coefficients $\{f_k\} = \{30, 1, 2, 3, 4, 5\}$. We use these facts to express $\hat{f}_c$ as

$$\hat{f}_c \approx f_0 + \sum_{k=1}^{N} f_k 10^{-k} \tag{3.37}$$

where N is an arbitrary integer number selected based on some desired level of accuracy and f_0 is a constant chosen based on a priori information about the load. Figure 3.4 shows

how one can use this equation to determine $\hat{f}_c$. When compared to a brute-force search, the proposed algorithm reduces the search space from 10^N to $2(10N)$. This represents a significant reduction in computation time.
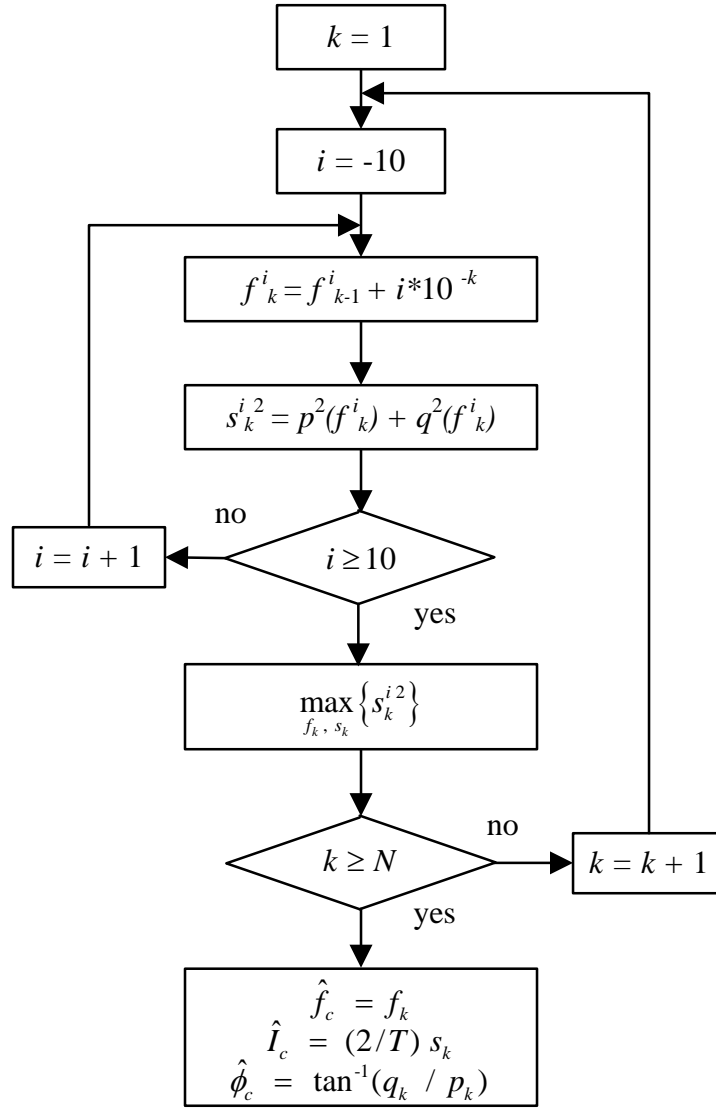
Figure 3.4: Algorithm for estimating $\hat{f}_c$, $\hat{I}_c$, and $\hat{\phi}_c$. Note that most of the effort is focused on estimating the k-th term in Eq. 3.37.

3.3.2. Overall Approach to Impedance Estimation

Figure 3.5 shows a partial implementation of the complete estimation algorithm for the resistance R_c. As shown, $v_m(t)$ is continually shifted and placed through the corre-

lator. Note that the output at the i-th time step is referred to as $p_{c,i}$. Ultimately, we compute the average of the set $\{p_{c,0}, p_{c,1}, p_{c,2}, ..., p_{c,M}\}$ as well as the average of the set $\{\hat{I}_{c,0}, \hat{I}_{c,1}, \hat{I}_{c,2}, ..., \hat{I}_{c,M}\}$. Denoting these averages as $\overline{p_c}$ and $\overline{I_c}$, respectively, we modify Eq. 3.15 to solve for R_c, i.e.

$$R_c = \frac{2\overline{p_c}}{\overline{I_c^2}}. \tag{3.38}$$

The inductance L_c is calculated in a similar manner. Note that averaging has been used to help reduce the effects of noise, and its use is common in such applications [86, 87, 88]. In general, the time step t_o can be much larger than the sampling interval and the averaging windows can be overlapped so that the calculation of the impedance at any specific time only requires the calculation of one new value of p_c.
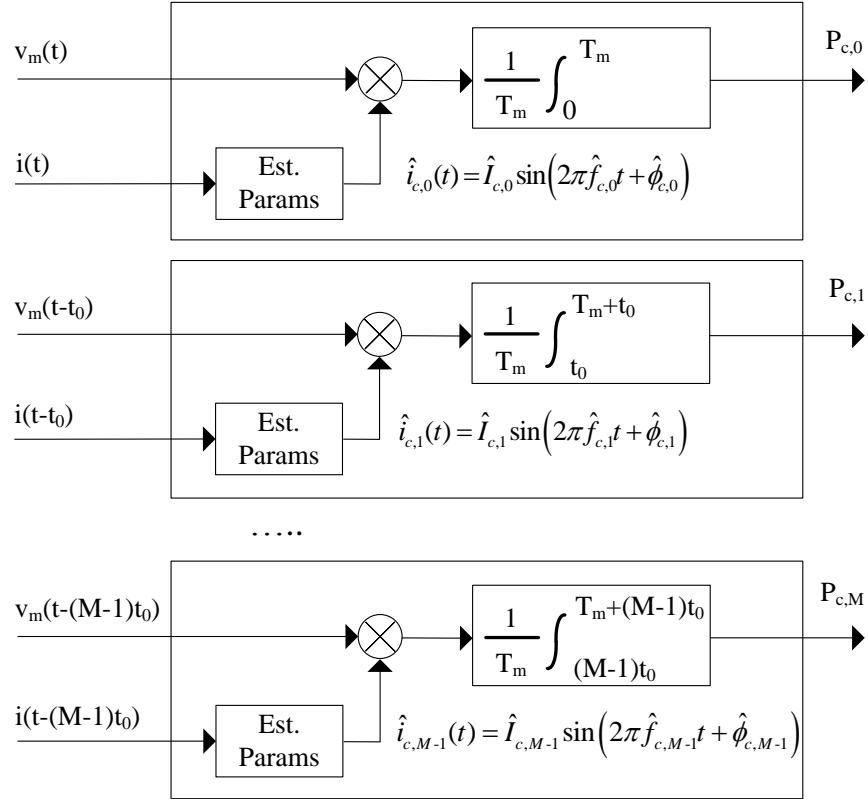
Figure 3.5: Partial implementation of the complete estimation algorithm for the resistance R_c. Each block represents the computations performed at each time step.

3.4. Simulation Results

A simulation model was built to demonstrate the performance of the proposed estima-
tion method. This model is based on the physical system shown in Figure 3.6, which was
constructed in the laboratory. Section 3.5 presents experimental results for the correspond-
ing test setup. The load in this system is a 1/4hp, 4-pole, single-phase induction machine.
This motor, like any other, injects various currents due to eccentricities and other effects.
To simulate these phenomena, the simulated machine was given a slightly imbalanced load
torque of the form

$$T(t) = T_0 + T_1 \cos(2\pi f_l t + \phi). \tag{3.39}$$

This torque produces interharmonic currents at the frequencies $f \pm f_l$, where f is the fun-
damental [89]. In the simulation model, the upper sideband in the current is placed at
89.87655Hz and the lower sideband is placed at 30.12345Hz. The constant T_1 is adjusted
so that the actual interharmonic currents have the same magnitudes relative to the funda-
mental as they do in the laboratory setup. The grid impedance is modeled by a resistance
R in series with an inductance L. A saturable transformer is mounted in parallel with the
voltage source. Simulation was performed using Simulink.
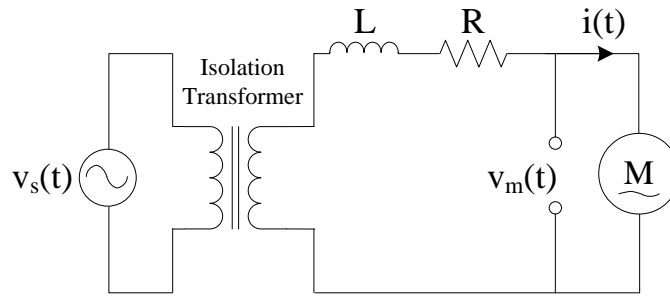
Figure 3.6: Schematic representation of the physical system used for
testing in the laboratory. This same system was modeled in Simulink.

Figure 3.7 shows the zoomed-in frequency spectra of both the terminal voltage and
current. Note that the injected interharmonics are considerably smaller than the fundamen-
tal and the principal harmonics. Table 3.1 lists several of the magnitudes. Note that the

Table 3.1: Harmonics data of the simulation circuit.

Frequency (Hz)	Voltage (V)	Current (A)
30.1	$7.12(10^{-3})$	$11.07(10^{-3})$
60.0	157. 25	6.06
89.9	$3.62(10^{-3})$	$5.41(10^{-3})$
180.0	6.86	0.56
300.0	1.06	0.06
420.0	0.72	0.03

injected signals are approximately 3 orders of magnitude smaller than the fundamental.
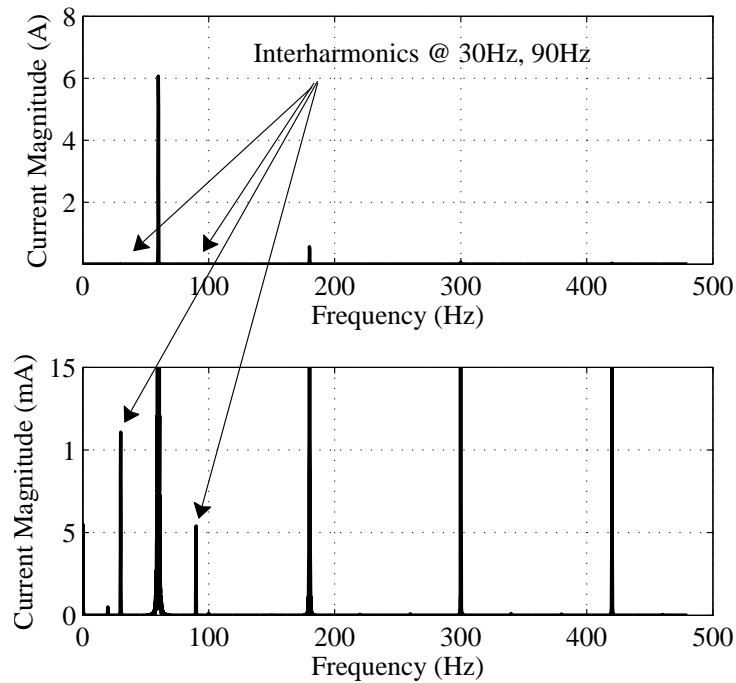
Figure 3.7: Top: Current spectral density. Bottom: Details of the
interharmonics used for impedance estimation.

Table 3.2 demonstrates the action of the MLE algorithm presented in Section 3.3. Note that each row shows the amplitude, phase, and frequency estimates as additional terms are added to the power series expressed in Eq. 3.37. With $N = 5$, i.e. 5 digits after the decimal, the error in the estimates of R_c and L_c are are extremely small.

The results presented in Table 3.2 show that estimates of R_c and L_c are highly depen-

Table 3.2: Simulation results as k is incremented from 1 to 5 in
Eq. 3.37 with $R = 0.65\Omega$ and $L = 0.25mH$.

k	$\hat{I}_c$ (mA)	$\hat{\phi}_c$ (rad)	$\hat{R}(\Omega)$	Error(%)	$\hat{L}$(mH)	Error(%)
1	11.08752	0.60568	0.0148	-97.71	3.4472	1278.89
2	11.18365	-0.06194	0.1601	-75.37	3.3403	1236.12
3	11.18581	0.94077	0.6415	-1.30	0.6178	147.12
4	11.18586	1.02608	0.6500	0.01	0.2728	9.15
5	11.18586	1.03290	0.6504	0.06	0.2489	-0.40

Table 3.3: Simulation Results as R is varied.

$\hat{R}(\Omega)$	$R(\Omega)$	Error(%)	$\hat{L}$(mH)	L(mH)	Error(%)
1.6517	1.65	0.10	0.4503	0.45	0.07
1.3994	1.40	-0.00	0.4485	0.45	-0.33
1.1610	1.15	0.96	0.4469	0.45	-0.69
0.9006	0.90	0.07	0.4476	0.45	-0.53
0.6502	0.65	0.03	0.4515	0.45	0.33

dent on an accurate measurement of $\hat{f}_c$. In practice, we have found that similarly accurate estimates cannot be obtained using the DFT or an interpolated DFT. Note that other researchers have reached similar conclusions [38]. The typical solution to this problem has been to increase the magnitude of the injected signal.

Table 3.3 presents results as R is varied. Note that the estimation errors are low in all cases.

3.5. Experimental Results

The proposed method has also been applied in two different experimental setups. In the first of these, an induction motor was connected to a test source through a transformer and a controllable resistance. In the latter, the same machine was connected to a standard electrical outlet and tests were performed as the actual line impedance varied throughout a typical summer day.

3.5.1. Controlled Test

Figure 3.6 shows the test arrangement for the first set of validation experiments. The source is an Agilent 6813B programmable power supply and the load is a 1/4hp, 4-pole, single-phase induction machine. The motor is connected to the supply through a 1 kVA, 1:1 isolation transformer, 16AWG cabling, and a high-power potentiometer. Following each experiment, the motor was disconnected and the impedance was measured using a high-accuracy impedance analyzer through a set of Kelvin probes. The transformer leakage inductance, which is 0.45mH, was found to dominate the reactance in all cases. The variable resistance was adjusted to demonstrate the effectiveness of the method. The voltage and current were sampled at 10kHz using a 16-bit A/D converter.

Impedance estimation was performed using an interharmonic signal produced by eccentricity in the rotor. The frequencies of such naturally-occurring signals are given by the expression [76, 89]

$$f_h = f\left[k\left(\frac{1-s}{p}\right)\pm s\right] \tag{3.40}$$

where $k/p = 1, 3, 5, 7, ...$, f is the supply frequency, s is the slip, and p is the number of pole pairs. For a four-pole machine, the two relevant signals exist at approximately 30Hz and 90Hz, respectively. Other terms in Eq. 3.40 can be used to estimate the impedance at higher frequencies. Note that the fundamental current was approximately 6A, and that the 30Hz interharmonic was approximately 11mA. Figure 3.8 shows the measured current spectrum.

Table 3.4 shows the results as the resistance was varied between 1.65Ω and 0.65Ω. Note that the errors were less than 5% in all cases.

3.5.2. Line-Connected Test

The proposed method has also been tested in the field. Measurements were performed at a standard 120V electrical outlet in a campus building. The load was the same motor de-
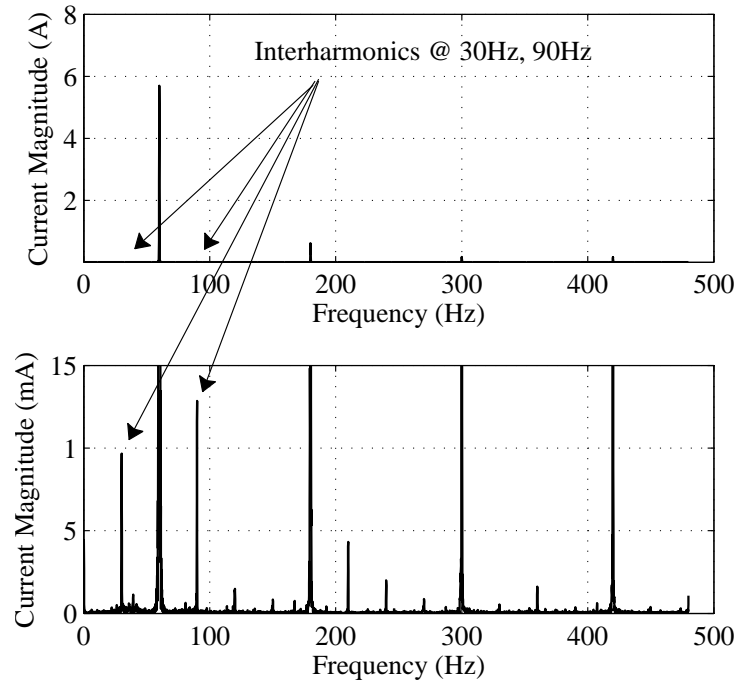
Figure 3.8: Top: Current spectral density for the test motor.
Bottom: Details of the interharmonics used for impedance estimation.

Table 3.4: Test results for Pure source - Transformer - Resistor - Motor Configuration.

$\hat{R}(\Omega)$	$R(\Omega)$	Error(%)	$\hat{L}$(mH)	L(mH)	Error(%)
1.6977	1.65	2.89	0.4586	0.45	1.92
1.4524	1.40	3.74	0.4343	0.45	-3.48
1.1729	1.15	1.99	0.4528	0.45	0.63
0.9160	0.90	1.78	0.4401	0.45	-2.18
0.6306	0.65	-3.08	0.4438	0.45	-1.38

scribed in Sec. 3.5.1. Measurements were performed at various times throughout a typical July day in Charlotte, North Carolina. Figure 3.9 shows the voltage recorded at the outlet during two different motor starts. Note that the voltage sag during the inrush period is significantly larger during the afternoon. This difference is the direct result of a higher line impedance during the afternoon, and it provides clear evidence of the need for measurements over time. Such variations are to be expected as line impedance increases as loading and temperature increase. Furthermore, it is expected that the impedance is impacted to some degree by voltage regulation at the feeder level.
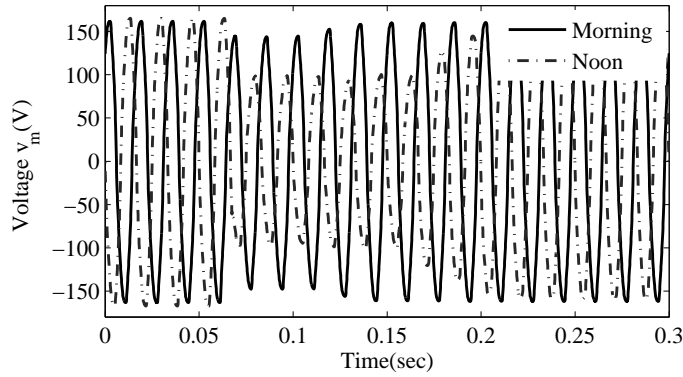
Figure 3.9: Line voltage during motor starting at two different times on a typical July day. The effect of the changing line impedance is clear.

The line impedance was estimated for both the morning and afternoon cases presented in Figure 3.9. In the morning, $\hat{R}_c$ was 0.60Ω and $\hat{L}_c$ was 0.16mH; in the afternoon, $\hat{R}_c$ was 3.55Ω and $\hat{L}_c$ was 0.57mH. To validate these results, a simulation was performed in Matlab. The measured current and impedance values were used to predict the voltage at the outlet both during and after the motor start. This prediction is given from the equation

$$\hat{v}(t) = \hat{v}_s(t) - \hat{R}_c i(t) - \hat{L}_c \frac{di(t)}{dt}. \tag{3.41}$$

The source voltage is, of course, difficult to access and thus difficult to measure. Its value was estimated using the same procedure presented in [42], which assumes that $v_s(t)$ is stiff
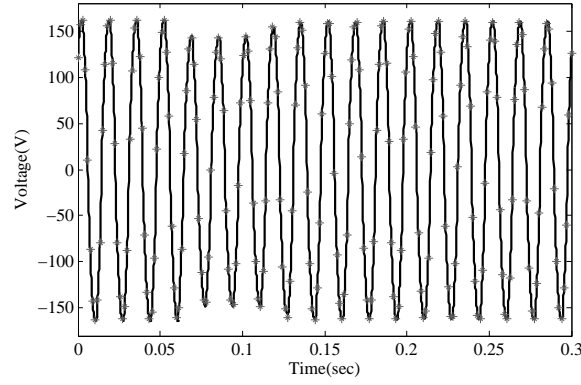
(a)
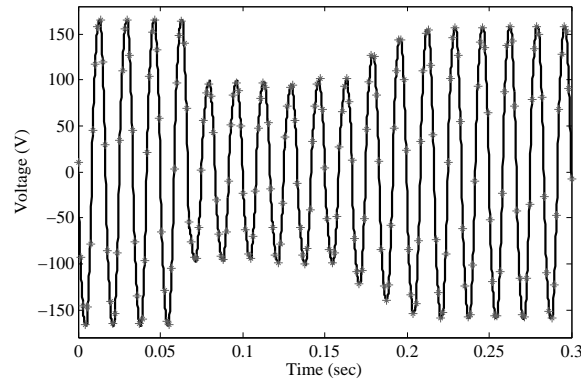
(b)

Figure 3.10: Predicted (+) and measured (solid line) voltages at the outlet during the two motor starts considered in Figure 3.9. (a) shows results from the morning, and (b) shows results from the afternoon.

and that :

$$v_s(t) \approx v_s(t - nT) \tag{3.42}$$

for small multiples n of the fundamental period T. Using this assumption, measurements of the outlet voltage prior to the connection of the load provide an estimate of the source voltage. Denote this estimate as $\hat{v}_s(t)$.

Figure 3.10 compares the measured and predicted outlet voltage in the morning and afternoon cases considered above. Note the close agreement in both cases.

3.6. Conclusion

This chapter proposes a new nonintrusive method to estimate online grid impedance using harmonic sources are available in the system. The method was experimentally verified on many configurations. In simulation, there exists a relatively good correspondence between the estimated and setting values. As can be observed in experiment case, there also have a good agreement between the measured voltage and the calculated voltage during transient. The method does not account for the cases that harmonics source varies to much during measurement, as well as the case of other loads generate harmonics close to the frequency of interest. Beyond these assumptions, the estimates using the proposed algorithm are quite match to expectations. The ease of installation, lower cost, and reasonable accuracy of the method are very valuable features from the utility perspective.

CHAPTER 4: A STABILITY ANALYSIS AND DESIGN FOR GRID-TIED
DIGITAL PFC CONVERTERS

A positive current feedforward compensator for a PFC converter is proposed and demonstrated. This compensator is applied to a converter with a boost topology operating in continuous conduction mode with average current control. The compensator adjusts the current reference in order to counteract the effects of the time-varying source impedance. Experimental measurements verify that the compensator improves the stability of a converter that is connected to a source with a time-varying impedance. The controller is modified to adapt with changes of working condition to assure stability of overall system.

4.1. Introduction

The boost topology is a popular choice for single-phase AC-DC preregulators with high power factor and low current harmonic distortion [25], [37], [23]. The most common implementation, particularly in high power applications, uses a two-loop control system with average current mode control [37]. The use of so-called active power factor correction (PFC) has become increasingly common in response to concerns over the harmonic currents produced by the many electronic devices now distributed throughout AC power systems.

The performance of a PFC converter depends heavily on the interaction between the converter and its source [23]. Problems arising from this interaction are common in power electronic systems. In the past, much attention has been given to the analysis and mitigation of such interactions in DC systems [26], [60], [28]. Problems can also occur, however, when PFC converters are placed in AC systems. High-frequency interactions well above the fundamental line frequency have been reported in several sources, including [23] and [32]; low frequency interactions resulting from the connection to sources such as small

generators and UPS devices are reported in [30], [31].

Several approaches have been proposed for mitigating the stability issues that can be caused by converter-source interactions. Reference [23], for instance, discusses the addition of an *RC* damping filter. The simplicity of this approach makes it attractive, but its effectiveness is limited because the bandwidth of the overall system depends on the output power, input voltage, and source impedance. If any of these parameters change, as they often do in practice, the degree-of-stability could still be compromised. Other approaches include various feedforward compensators [37], [23]. These methods tend to improve performance but do not necessarily guarantee stability if the source impedance is time-varying, which occurs frequently in practice [90], [91].

This paper demonstrates the effectiveness of a feedforward compensation approach that is based on input condition monitoring. In the proposed system, the reference current is modified based on measurements of the time-dependent source impedance. The approach is shown to prevent instabilities that can result when there are changes in system conditions or converter loading.

The paper begins by presenting the model for the interaction between the converter and its source. After analyzing the complete system model, Section III proposes and analyzes the new feedforward compensator. Section IV demonstrates the effectiveness of the new approach using several experimental measurements. Conclusions are presented in Section V.

4.2. Modeling the Source-Converter Interaction

Figure 4.1 shows the block diagram of a typical PFC converter as modified to include the proposed compensator. The converter itself has a boost topology and is operated using average current control. The design of the input compensator block is discussed in more detail in Section III. The focus is first placed on modeling the interaction between the system and the converter.
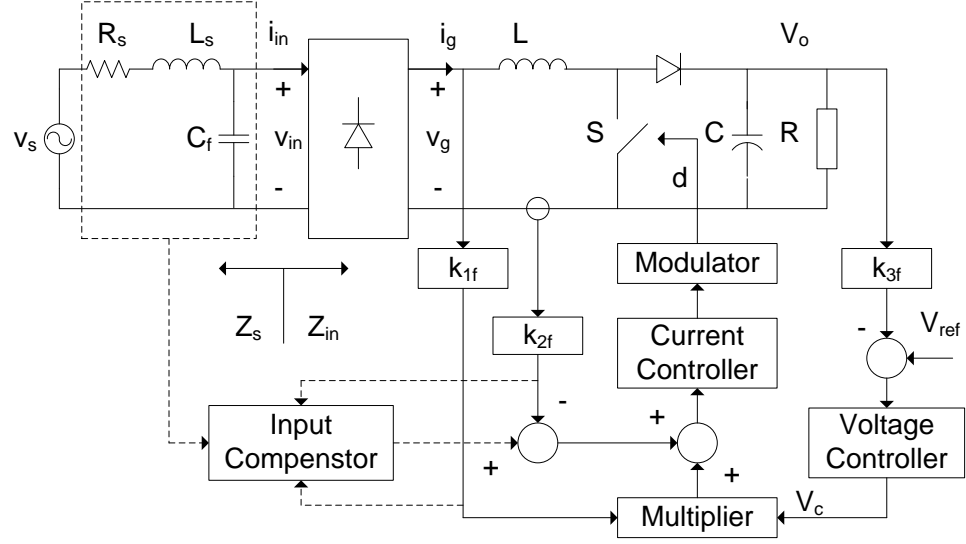
Figure 4.1: Block diagram of a PFC converter using a boost stage
with average current control and an input capacitor C_f. Both the source impedance and
the proposed compensator have been included. k_{1f}, k_{2f}, and k_{3f} represent scale factors for
the input voltage, input current, and output voltage, respectively.

4.3. PFC Converter Input Impedance

The PFC converter in Figure 4.1 utilizes a two-loop control structure with an outer
voltage-regulating loop providing a reference to an inner current-shaping loop. The aver-
aged state-space model for the input current is [92]

$$L\frac{d\bar{i}_g(t)}{dt} = \bar{v}_g(t) - (1 - d(t))\bar{v}_o(t), \tag{4.1}$$

where the overbars denote local averages and $d(t)$ is the continuous duty ratio. In a well
designed converter operating near periodic steady state, the output voltage exhibits only
small variations and can be treated as a nearly constant voltage source [25], i.e.

$$\bar{v}_o(t) = V_o + \hat{v}_o(t) \tag{4.2}$$

where

$$|\hat{v}_o(t)| \ll |V_o|. \tag{4.3}$$

Substituting Eq. 4.2 into Eq. 4.1 yields

$$L\frac{d\bar{i}_g(t)}{dt} = \bar{v}_g(t) - (1 - d(t))V_o - (1 - d(t))\hat{v}_o. \tag{4.4}$$

When Eq. 4.3 is satisfied, the nonlinear term $(1 - d(t))\hat{v}_o$ is much smaller in magnitude than the linear term $(1 - d(t))V_o$. Therefore, the nonlinear term can be discarded to obtain

$$L\frac{d\bar{i}_g(t)}{dt} = \bar{v}_g(t) - (1 - d(t))V_o. \tag{4.5}$$

The input current can be expressed in Laplace domain as follows

$$i_g(s) = G_{vi}(s)v_g(s) + G_{di}(s)d(s), \tag{4.6}$$

where the line-to-current transfer function $G_{vi}(s)$ is

$$G_{vi} = \left.\frac{i_g(s)}{v_g(s)}\right|_{d=0} = \frac{1}{Ls} \tag{4.7}$$

and the control-to-current transfer function $G_{di}(s)$ is

$$G_{di} = \left.\frac{i_g(s)}{d(s)}\right|_{\bar{v}_g=0} = \frac{V_o}{Ls} \tag{4.8}$$

Using the assumptions and results presented previously, the dynamic model of the converter can be simplified as shown in Figure 4.2. Note that the voltage-loop compensator output V_c has been assumed to be constant. This is a reasonable approximation since the output voltage has a very small ripple. Additionally, note that the proposed input compensator has been removed to simplify the initial analysis.

The simplified block diagram shown in Figure 4.2 can be used to determine the signal
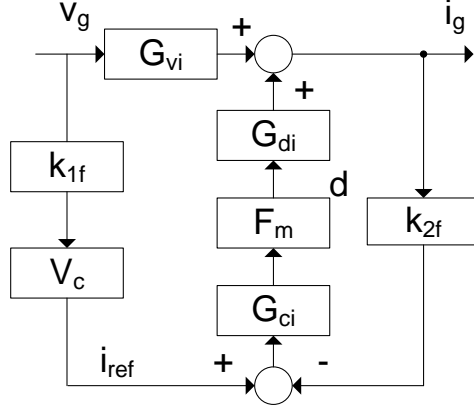
Figure 4.2: Block diagram for the analog implementation of the control of the PFC converter shown in Figure 4.1. $k_{1f}(s)$ and $k_{2f}(s)$ represent signal-conditioning filters for the input voltage and input current, respectively. $G_{di}(s)$ and $G_{vi}(s)$ are the control-to-current and the line-to-current transfer functions, respectively. $G_{ci}(s)$ is the compensator for the current loop and $F_m(s)$ is the transfer function for the pulse-width modulator, which is simply a scalar.

relationships inside the converter

$$i_{err}(s) = k_{1f}(s)V_c v_g(s) - k_{2f}(s)i_g(s) \tag{4.9}$$

and

$$i_g(s) = G_{ci}(s)F_m(s)G_{di}(s)i_{err}(s) + G_{vi}(s)v_g(s) \tag{4.10}$$

Substitute $i_{err}(s)$ from Eq. 4.9 into Eq. 4.10 and solve for input admittance of the converter. That admittance can be found as

$$Y_{in} = \frac{i_g(s)}{v_g(s)} = \frac{1}{1+T_i(s)}\left(G_{vi}(s) + \frac{k_{1f}(s)}{k_{2f}(s)}V_c T_i(s)\right), \tag{4.11}$$

where the open loop transfer function $T_i(s)$ of current loop controller is

$$T_i(s) = k_{2f}(s)G_{ci}(s)F_m(s)G_{di}(s). \tag{4.12}$$

To reduce noises in the feedback paths, two first-order filters k_{1f} and k_{2f} are applied to the

measured input voltage and inductor. They are of the forms

$$k_{1f}(s) = \frac{k_1}{\tau_{fv}s+1}, \quad k_{2f}(s) = \frac{k_2}{\tau_{fi}s+1} \tag{4.13}$$

The compensator for the inner current loop G_{ci} is

$$G_{ci}(s) = K_{pi}\left(1 + \frac{1}{\tau_{ii}s}\right) \tag{4.14}$$

It is important to note that the figure depicts an analog implementation of the control system. In practice, however, control is often implemented using a digital signal processor. In those cases, the required bandwidth of the current control loop is comparable to the Nyquist frequency [90]. This implies that relevant poles and zeros are introduced by both the computational delays and the discretization caused by the digital pulse-width modulator. In this case, we use continuous-time models of the sample-and-hold at the output of the discrete controller and the computational delays inside the microcontroller. These models are then treated as part of the plant model. The zero-order hold at the output of the controller is modeled by the transfer function

$$G_{ZOH}(s) = \frac{\left(1 - e^{-sT_s}\right)}{sT_s} \approx \frac{1}{(1 + sT_s/2)}, \tag{4.15}$$

where T_s is the time between samples [90]. Although the delay between the sampling of the feedback signals and the application of the resulting reference signal takes less than a single sampling period, it is difficult to determine how much time is actually required. As a conservative estimate, we assume that computation requires an entire sampling period. This is modeled as a time delay of T_s. In the frequency domain, we approximate this using a first-order Pade approximation[90], i.e.

$$G_{delay}(s) = e^{-sT_s} \approx \frac{(1 - sT_s/2)}{(1 + sT_s/2)}. \tag{4.16}$$

Adding these components, the open-loop transfer function $T_i(s)$ becomes

$$T_i(s) = k_{2f}(s)G_{ci}(s)F_m(s)G_{di}(s)G_{ZOH}(s)G_{delay}(s), \tag{4.17}$$

and the input admittance is modified accordingly.

4.3.1. Source Model

The system to which the converter is connected is modeled as an ideal source behind a resistance R_s and an inductance L_s. Typically, a filter capacitor C_f is also placed on the input side of the rectifier. The equivalent impedance of this combination is

$$Z_s = \frac{L_s s + R_s}{L_s C_f s^2 + R_s C_f s + 1}. \tag{4.18}$$

4.3.2. Model for the Complete System

Although the PFC is designed to work over a large range of input voltages, its performance may become degraded or even unstable when it is connected to the power source. This problem is caused by the interaction with the source impedance, Z_s. To model this interaction, we need to know the admittance looking into the input side of the rectifier. This impedance is defined as $v_{in}(s)/i_{in}(s)$, where $v_{in}(s)$ and $i_{in}(s)$ are the Laplace transforms of the voltage and current on the input side of rectifier, respectively. Assuming minimal distortion at the input, this voltage will be of the form

$$v_{in}(t) = V \sin(\omega t). \tag{4.19}$$

If the converter is operating properly, there should be minimal phase shift between $v_{in}(t)$ and $i_{in}(t)$ and minimal current harmonic distortion; thus,

$$i_{in}(t) = I\sin(\omega t). \tag{4.20}$$

Under these conditions, the average voltage and current at the output side of the rectifier will be

$$\bar{v}_g(t) = \text{sgn}(v_{in}(t))V\sin(\omega t) \tag{4.21}$$

and

$$\bar{i}_g(t) = \text{sgn}(v_{in}(t))I\sin(\omega t). \tag{4.22}$$

To determine the input admittance, we can take the ratio of the Laplace transforms of Eqs. 4.21 and 4.22. Regardless of the sign of $v_{in}(t)$, this ratio will be

$$\frac{i_{in}(s)}{v_{in}(s)} = \frac{i_g(s)}{v_g(s)}. \tag{4.23}$$

According to this result, Eq. 4.11 can be used to represent the overall input admittance of the converter. Other researchers have made similar assumptions [30],[23].

If we include the source impedance Z_s, the system can be modeled as shown in Figure 4.3. The input signal in that model is the source voltage v_s and the output signal is the current i_g. The overall source-converter interaction transfer function is thus

$$Y(s) = \frac{i_{in}(s)}{v_s(s)} = \frac{Y_{in}(s)}{1 + Z_s(s)Y_{in}(s)} = \frac{Y_{in}(s)}{1 + T_m(s)}, \tag{4.24}$$

where $T_m(s)$ is

$$T_m(s) = \frac{Z_s}{1 + T_i}\left(G_{vi}(s) + \frac{k_{1f}}{k_{2f}}V_c T_i\right). \tag{4.25}$$

These equations show that the interactions with the source impedance can reduce the degree-of-stability of the overall system. The Nyquist criterion shows that stability is con-
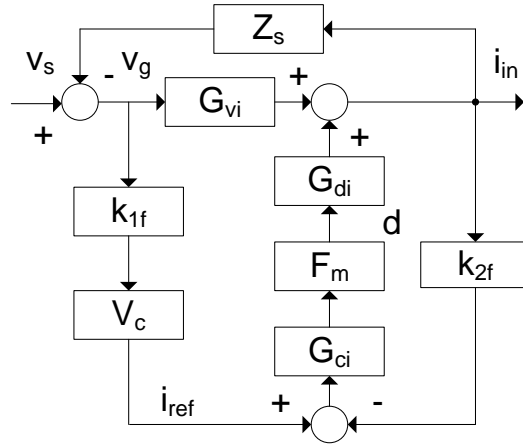
Figure 4.3: Analog block diagram of the complete system including
the source impedance Z_s.

trolled by the the transfer function $T_m(s)$. Because this function depends on V_c, the overall
degree-of-stability is affected if there is a change in either the power demand or the input
voltage level. In addition, $T_m(s)$ also depends on the source impedance, which is often
unknown. Changes in this quantity, which often occur in practice, can thus impact the
degree-of-stability as well [30], [23]. To demonstrate the impact, we simulated a 350W
converter connected to a single-phase 60Hz source. Figure 4.4 describes the impact of
changes in the source impedance and the input voltage. Frequency responses are shown for
the four different sets of input conditions outlined Table 4.1.

Table 4.1 shows that under normal conditions (i.e. Case 1), the simulated converter
is stable but has a limited phase margin. The worst case scenario is one in which both the
impedance and the voltage are low (i.e. Case 3). Given measurements of the system voltage
and input impedance, the bandwidth of the system can be adapted and such instability can
be prevented. If $|Z_{in}(s)| \gg |Z_s(s)|$ for all frequencies, then the overall system should be
stable and the effect of the source impedance becomes negligible. In practice, it is difficult
for this to be true in all cases, as one does not often typically know the system impedance in
advance. If one designs so that $|Z_s(s)|$ is smaller than the magnitude of the input impedance
at all interfaces, then it can become difficult to meet all of the other relevant performance
specifications for the converter. In cases where $|Z_s(s)|$ is larger than $|Z_{in}(s)|$, the Nyquist
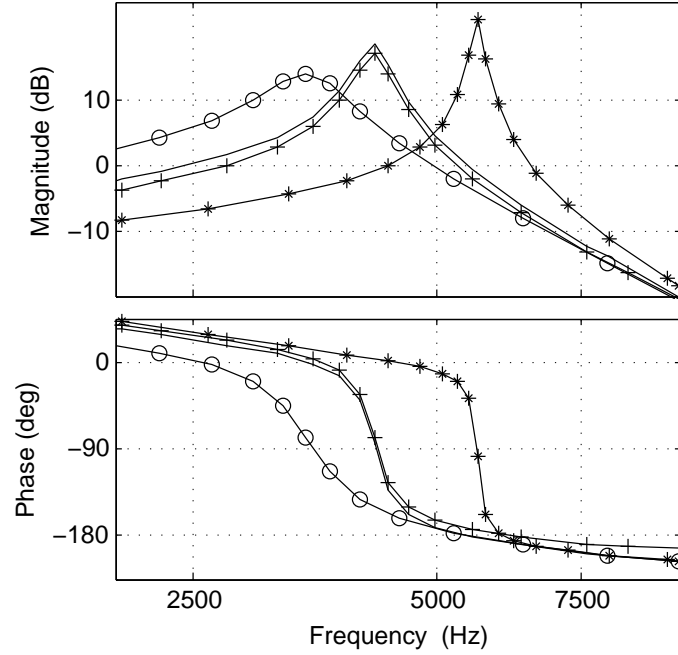
Figure 4.4: Frequency response of T_m as a function of input voltage and line impedance. Case 1 is indicated with +, Case 2 is a solid line, Case 3 is indicated with asterisks, and Case 4 is indicated with circles.

Table 4.1: Simulation cases for different input of the PFC converter.

Case #	V_{in} (VAC)	R_s (Ω)	L_s (mH)	PM (deg)
1	120	1.0	0.45	10.2
2	90	1.0	0.45	0.4
3	90	0.25	0.25	-9.5
4	90	3.0	0.65	8.2

criterion must be carefully applied to determine if stability is a problem.

In practice, issues tend to arise because of the nature of Z_s. As seen in Eq. 4.18, this impedance is resonant at a particular frequency. In the neighborhood of this resonant peak, the magnitude of Z_s may rise above the magnitude of Z_{in}. When this happens, instability can result. Knowing the source impedance, one can use the Nyquist criterion to prevent such instability. One issue that can arise, however, is that the source impedance is time-dependent. A method for overcoming this problem is proposed in the next section.

4.4. Compensator Design

To reduce the effect of the input impedance, one could refer the input voltage feedforward loop to the voltage source v_s as shown in Figure 4.5. The difficulty of measuring v_s is an obstacle, but it can be overcome. To do so, we modify the control system in figure. 4.5 to include the feedforward compensator $G_c(s)$ as shown in Fig. 4.6. The transfer function v_g/v_s is the same for both systems as long as the feedforward compensator $G_c(s)$ is of the form

$$G_c(s) = k_c Z_s(s), \tag{4.26}$$

where k_c is a fixed scale factor whose value is given by

$$k_c = \frac{I_{gRMS,nominal}}{V_{gRMS,nominal}}. \tag{4.27}$$

With this compensator, the system shown in Figure 4.5 modifies the reference current to counteract the effects of the source impedance. The difficulty, however, is that this new component requires periodic measurements of the source impedance. The authors measure this quantity using the method demonstrated in [93]. In that approach, the source impedance is determined using small interharmonic currents that are injected by the converter.

With the new compensator, the overall converter input admittance becomes

$$Y_{inFF}(s) = \frac{i_g(s)}{v_g(s)} = \frac{1}{1 + T_i - G_c T_i} \left(G_{vi} + \frac{k_{1f}}{k_{2f}} V_c T_i \right). \tag{4.28}$$

Adding the feedforward term in Eq. 4.28 modifies both the magnitude and the phase of the admittance in the vicinity of the resonance in Z_s. At frequencies well above and below the resonance, the effect of the term $G_c(s)T_i(s)$ becomes relatively negligible. In those frequency ranges, the magnitude of $G_c(s)$ is relatively small because it depends on the magnitude of Z_s, which is also also small in those same regions. In the neighborhood of
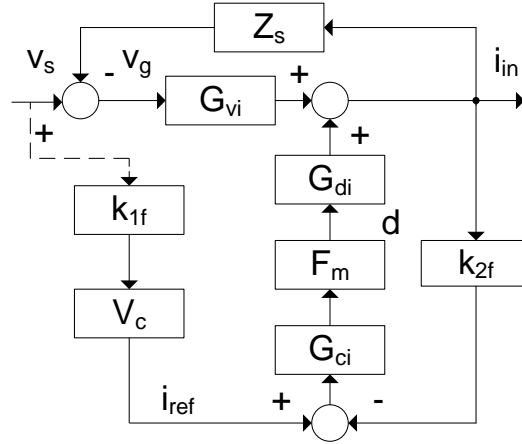
Figure 4.5: Analog block diagram of the complete system with the input voltage feedforward referred to the ideal source v_s.
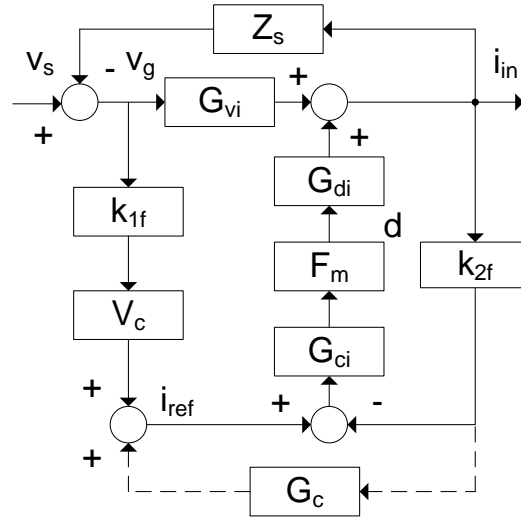
Figure 4.6: Analog block diagram of the complete system with the proposed new feedforward compensator.

the resonance, however, the effect of the compensator becomes more significant and both the magnitude and the phase of the input impedance are changed accordingly. This effect is observed in Figure 4.7, which shows the magnitude and phase of $Z_{inFF}(s)$, $Z_{in}(s)$, and $Z_s(s)$ for an example converter with the specifications presented in Table 4.2. Note that for frequencies well above and below the the resonant peak in Z_s, $Z_{inFF} \approx Z_{in}$.

Although it is clear that the compensator modifies the converter input impedance in the vicinity of the resonance in the source impedance, stability is best analyzed using the
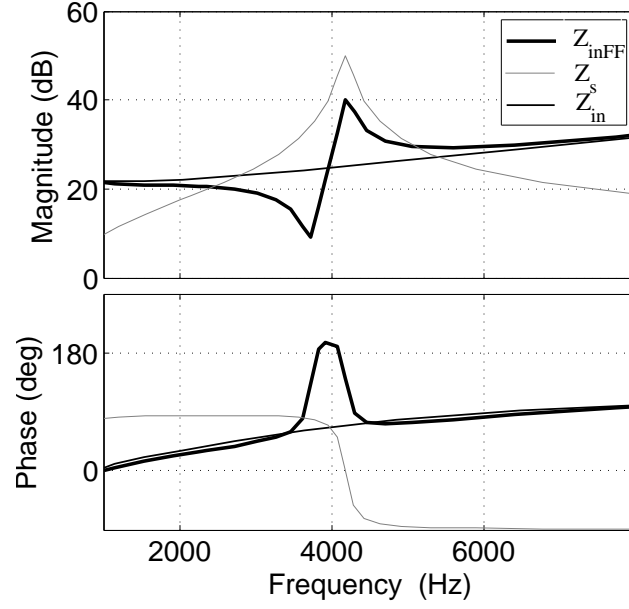
Figure 4.7: Magnitude and phase of $Z_{inFF}(s)$, $Z_{in}(s)$, and $Z_s(s)$ for the example converter with the specifications presented in Table 4.2.

Table 4.2: Parameters for the Experimental Converter.

Parameter	Value
Nominal Input Voltage, V_{in}	120VRMS
Nominal Output Power, P_o	350W
Output Voltage, V_o	380V
Switching Frequency, f_{SW}	80kHz
Sampling Frequency, f_S	40kHz
Inductance, L	1.2mH
Output Capacitance, C	1000μF
Input Filter Capacitor, C_f	3.2μF
Source Inductance, L_s	0.75mH
Source Resistance, R_s	0.45Ω

Nyquist criterion. With the compensator, the closed-loop transfer function becomes

$$Y(s) = \frac{i_{in}(s)}{v_s(s)} = \frac{Y_{inFF}}{1 + Z_s Y_{inFF}} = \frac{Y_{inFF}}{1 + T_{mFF}}, \tag{4.29}$$

where

$$T_{mFF}(s) = \frac{Z_s}{1 + T_i - G_c T_i} \left(G_{vi} + \frac{k_{1f}}{k_{2f}} V_c T_i \right). \tag{4.30}$$

Figures 4.8 and 4.9 present Nyquist plots for the same converter considered in Figure 4.7. In the first of these plots, results are shown for a converter without a compensator. In the latter, the results are shown for the condition in which a compensator has been added. Clearly, both the phase margin and the gain margin have increased.
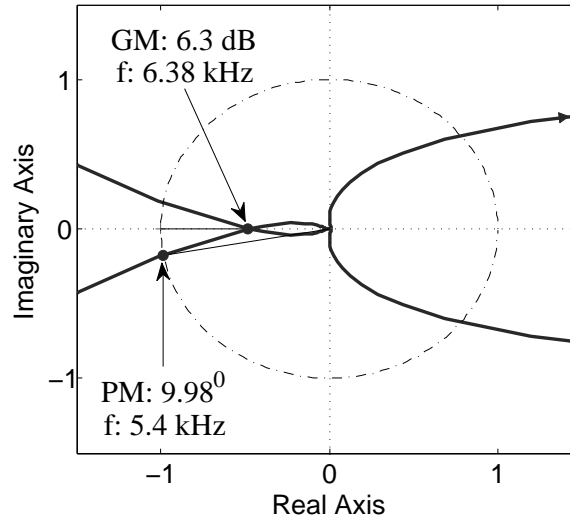
Figure 4.8: Nyquist plot analysis of $T_m(s)$ for the example converter without the compensator.
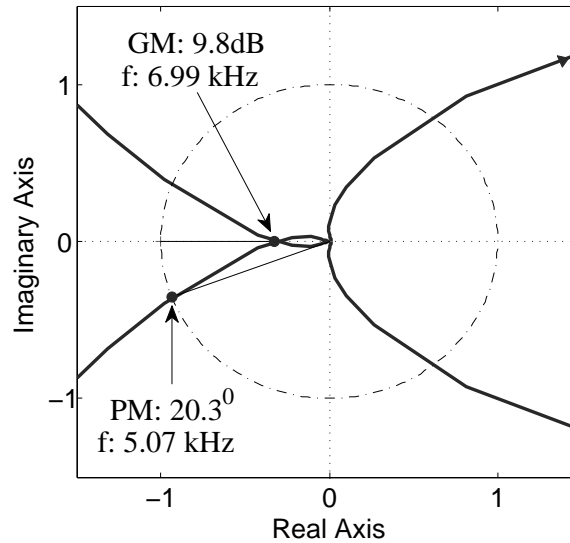
Figure 4.9: Nyquist plot analysis of $T_{mFF}(s)$ for the example converter with the compensator.

The primary benefit of the proposed approach is that it improves the stability of the

source-converter interaction without sacrificing the stability of the converter itself. For instance, it would be possible to modify $Z_{in}(s)$ to prevent instabilities due the source-converter interaction at all frequencies. The result, however, could likely be a degradation of the converter's individual performance. Furthermore, any controller designed to prevent instability for a known source impedance is not necessarily robust enough to compensate for changes in the impedance over time. The proposed compensator is able to respond to such changes.

4.5. Voltage Compensator Design

The outer voltage loop is needed to maintain the output voltage at the desired level. Because the output voltage contains inevitable second harmonic distortion in single-phase system [25], bandwidth of voltage loop must be sufficiently lower than line frequency. In this case it is around 10Hz. Without this, the second harmonics distortion would combine with the line frequency to create harmonics at the input reference of the current control loop. The result would be harmonic distortion input current. By restricting the voltage loop bandwidth, however, the output voltage will respond very slowly to the load changes. Sags or overvoltages at the output may thus occur. Voltage drops below the maximum input voltage, controllability may be lost. If the overvoltage on the other hand can overstress the power components.

To reduce harmonic distortion in the input current and improve dynamic response of output voltage, several methods were developed. One technique samples the output voltage at twice line frequency, where output voltage ripple is zero and DC output voltage is extracted [94] [95]. The other common method uses a notch filter to attenuate the second harmonic distortion in the voltage loop [96]. In the lab, a digital notch filter was used to reduce the second harmonic ripple before the voltage error amplifier input. Because of the

quantization errors in its coefficients, the digital notch filter is chosen as

$$H(z) = \frac{1 - 1.8596z^{-1} + z^{-2}}{1 - 1.7576z^{-1} + 0.8934z^{-2}}, \tag{4.31}$$

where voltage sampling frequency is 2 kHz. This frequency was below the switching frequency because the bandwidth of the voltage loop is much lower than the bandwidth of the current loop controller. With this filter, the voltage loop bandwidth is expanded to 80Hz. Detailed analysis of the notch filter design is shown in [96]. Experimental results show dynamic response of the PFC converter is much faster than the 10Hz bandwidth of the voltage loop.

4.6. Experimental Results
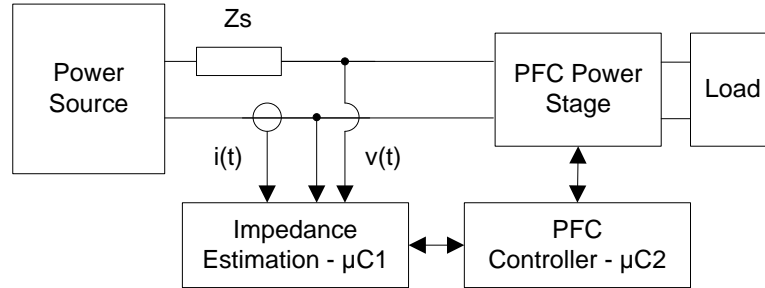
Figure 4.10: Digitally controlled PFC converter with line impedance measurement.

An experimental prototype was constructed in the laboratory. Specifications for this converter were presented in Table 4.2. Control was performed using the dsPIC30f6010a microcontroller. The input power source was a Model 6813B single-phase supply from Agilent. This source was placed behind an adjustable impedance consisting of an inductance and resistance. To demonstrate the effectiveness of proposed PFC system, we initially designed the current loop bandwidth to be 4kHz, and the voltage loop bandwidth to be 10Hz. A softstart procedure was implemented to gradually raise the output capacitor voltage from its precharged level to its final level to limit the current surge. In this example, and line impedance is estimated during softstart. Estimation of the line impedance is performed by

injecting a small current at 75 Hz. Figure 4.11 shows the waveforms of PFC converter at startup. From the figure, it is clear that the converter is stable at the low output levels used during the early stages of the soft start period (region 1 in the Figure 4.11). For Figure 4.11, the line inductance was 0.75mH, the line resistance was 0.45Ω, and the input voltage was 120 V. As the output power increased during region 2 in the Figure 4.11, PFC became unstable because of the interaction between line impedance and the converter. After several seconds, the line impedance was known and ready to be used for the feedforward compensator. In region 3, PFC was stable again.

Figure 4.11 shows FFT data for input current and voltage during the soft start . Note that the input voltage contains signal spectral content, one must be careful to inject current at a frequency at which v_{in} has negligible content. This can be verified prior to injection using FFT.
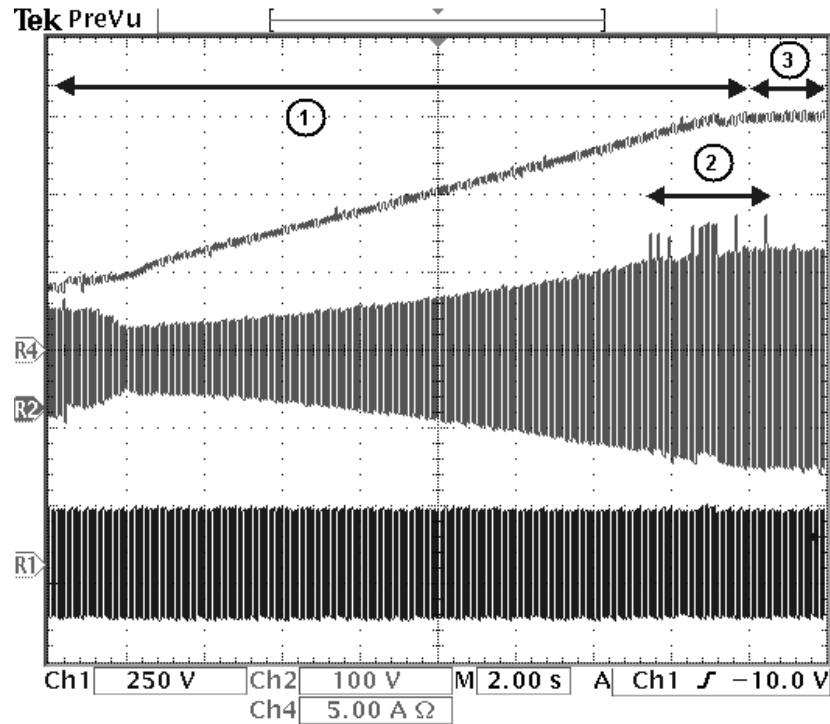
Figure 4.11: Voltage and current waveforms during soft start.

Various experiments were conducted to demonstrate the effectiveness of the proposed compensator. Figures 4.13 and 4.14 show how the system responded following a step
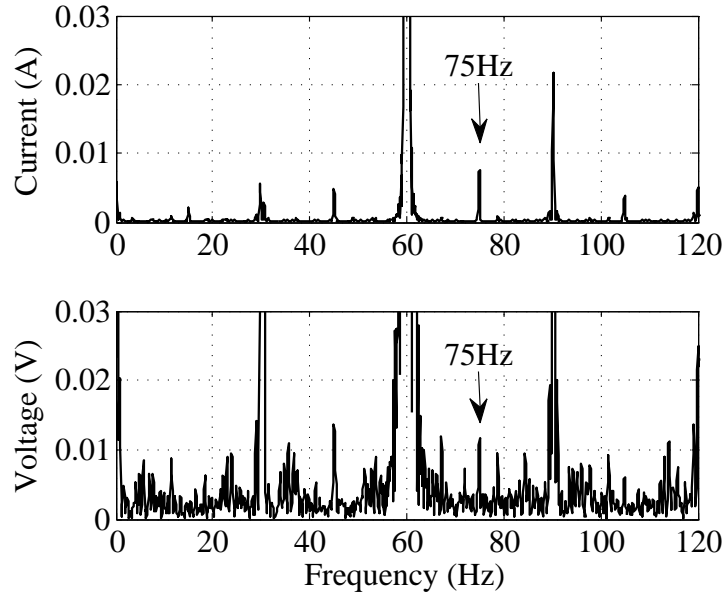
Figure 4.12: FFT data of voltage and current during soft start.

change in load from 440Ω to 280Ω without the compensator. Instability is apparent in both figures. Details of the input voltage, input current, and output voltage following the transient are presented in Figure 4.14. A similar step change in load was applied when the compensator was in use. The results are presented in Figures 4.15 and 4.16. Clearly, stability was maintained using the proposed approach. Figure 4.17 shows results for both a drop in load and a step in load. These were recorded without the notch filter. Current and voltage waveforms recorded with the notch filter are shown in Figure 4.18. Note that the output dynamic response is much faster with the notch filter.

4.7. Conclusion

The proposed method cannot cancel all of the effects of the source-converter interaction because the input impedance has effectively become a part of the power stage. It is clear, however, that this adaptive method significantly increases the overall degree-of-stability.

The proposed analysis and control method is general and can be implemented in many other grid-tied converter and inverter topologies, such as Cuk, SEPTIC, and Buck-Boost. The proposed method is also unlimited by input filter stage, as long as the bandwidth
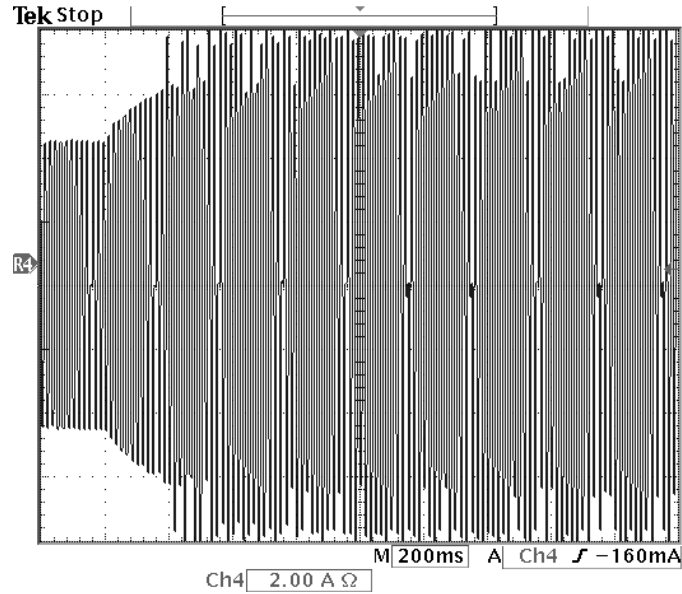
Figure 4.13: Input current in response to a step change in load
without the proposed compensator. The load was changed from 440Ω to 280Ω.
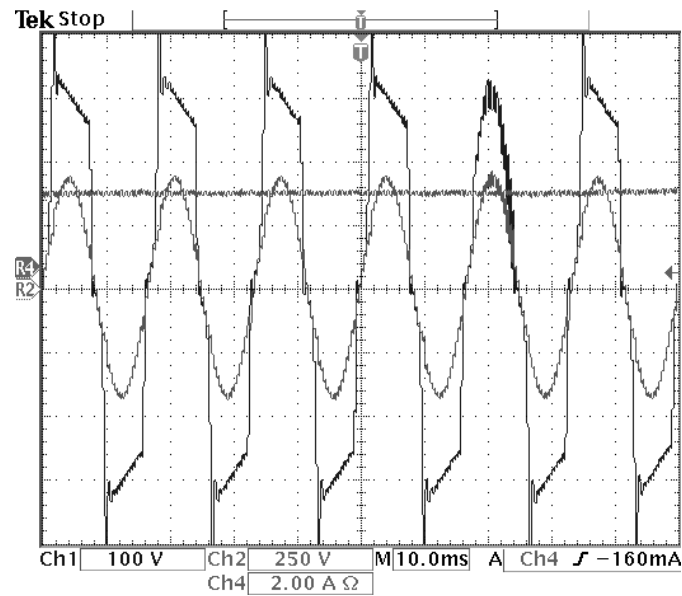
Figure 4.14: Input voltage, input current, and output voltage following
the step change shown in Figure 4.13. The input current displays clear instability.

changes due to computational requirements of the current feedforward loop during real-time operation do not affect the stability of the overall system. This means that the input filter can be designed as expected to suppress inrush current, and EMI in the grid.
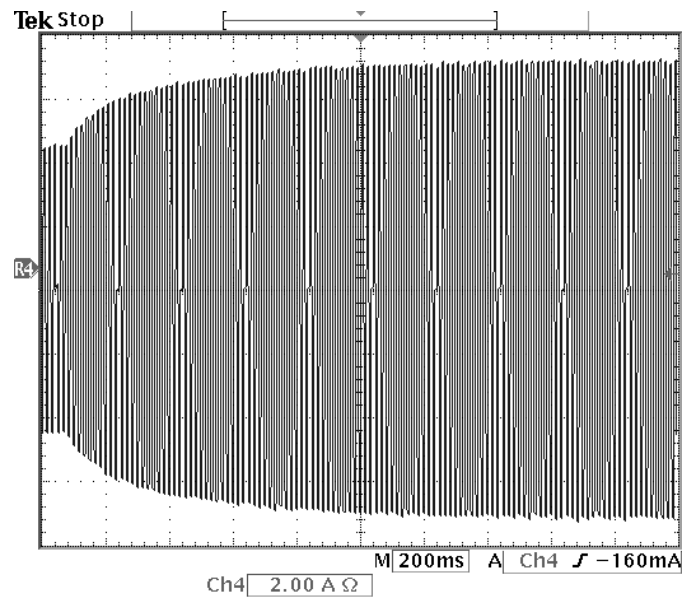
Figure 4.15: Input current in response to a step change in load with the proposed compensator. The load was changed from 440Ω to 280Ω.
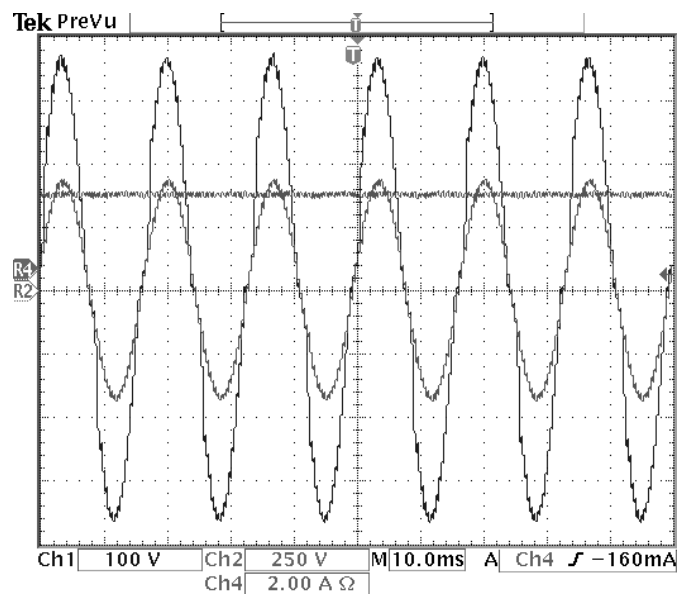
Figure 4.16: Input voltage, input current, and output voltage following the step change shown in Figure 4.15. The input current, which is the larger AC waveform in the figure, is clearly stable.
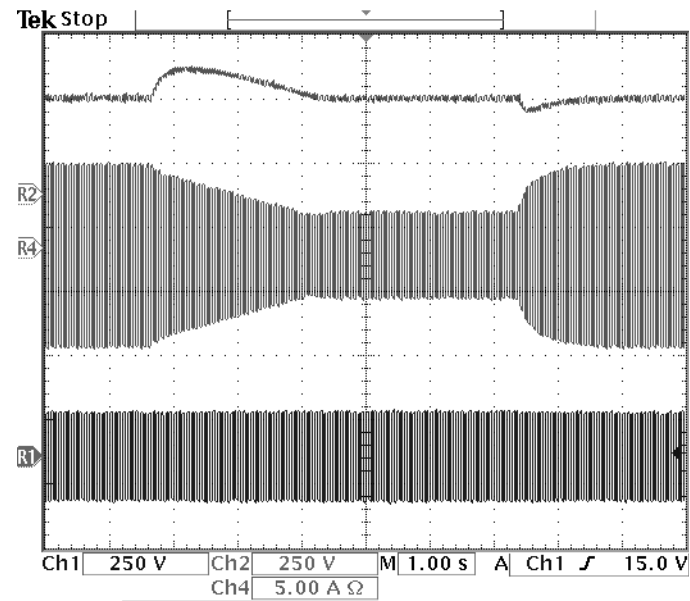
Figure 4.17: Current and voltage waveforms when step load changes up and down.
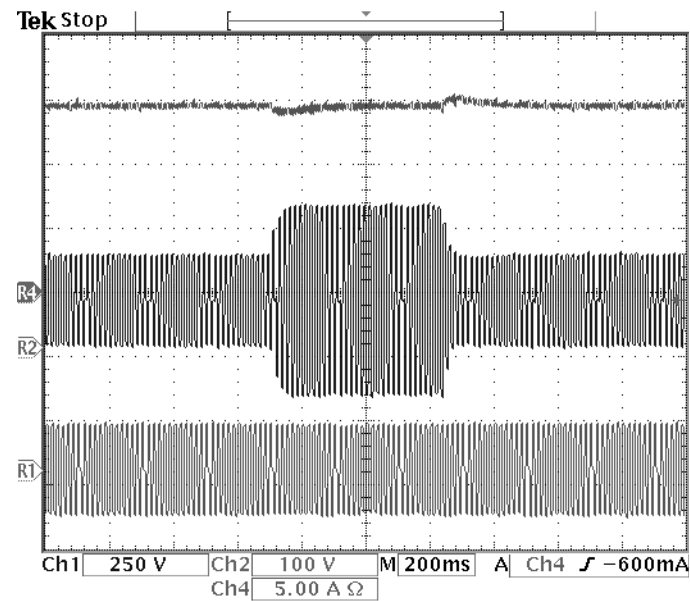
Figure 4.18: Current and voltage waveforms when step load changes up and down with new voltage loop controller.

CHAPTER 5: DETERMINATION OF HARMONIC SOURCES USING
ONLINE IMPEDANCE MEASUREMENT

5.1. Introduction

Pure sinusoidal waveforms are expected at customer sites. As nonlinear loads have become more prevalent in the power system, the voltage at the Point of Common Coupling (PCC) is no longer sinusoidal. Harmonic related problems continue to increase due to the continued growth of power electronics at the point-of-load. These power electronics include diode rectifiers, and adjustable speed drives that tend to draw harmonic and interharmonic currents at many different frequencies. Harmonic currents injected by nonlinear loads flow through the network impedance to cause voltage distortion at the PCC. This voltage distortion affects various locally-connected loads. Figure 5.1, for example, shows N customers connected to a single PCC. The kth load is connected through impedance Z_k, which represents the equivalent impedances of cables, transformers, circuit breakers, and other elements. Clearly, a harmonic injected by customer one would impact the current drawn by the other N-1 loads because of the harmonic voltage drops in the network impedance.

Utilities desire to charge customers that cause harmonic distortion. If utilities simply charge for harmonic distortion, even customers with linear loads will be charged because of the resulting voltage distortion produced by nearby nonlinear loads. In commercial buildings and industrial sites, utilities will charge based on the amount of reactive power which includes harmonics generated in the line [97, 98, 99]. To do so fairly, the true sources of harmonic currents need to be determined. Without such information, the cause of harmonic problems cannot be identified, and mitigation schemes cannot be designed until

the source of harmonics has been identified. Practical and reliable methods for identifying the polluters are needed to accelerate the mitigation process.
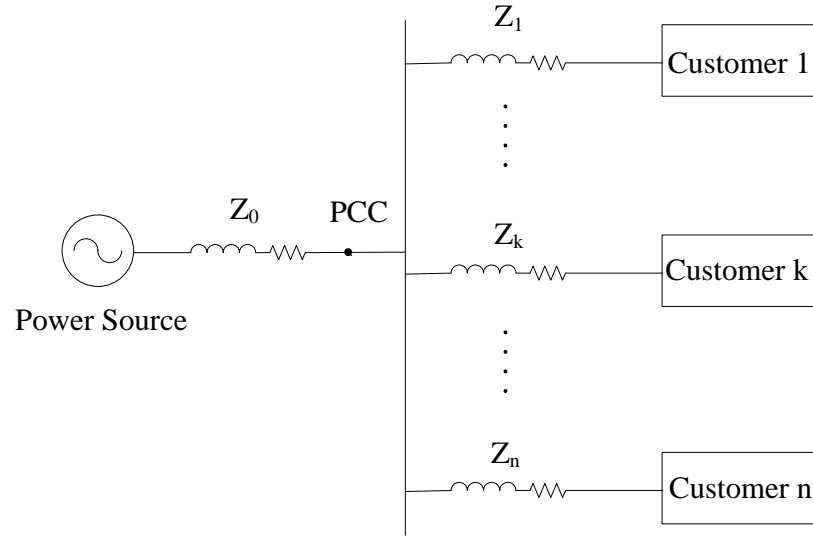
Figure 5.1: An example of a distribution power system feeding N customers at the PCC.

The problem with identification is that most customers are using linear loads together with non-linear loads. The harmonics injected by the nonlinear loads can thus even cancelled out under these circumstances. Therefore, it is not easy to share the responsibility for power quality degradation. This problem has been the subject of many publications, several of which are reviewed below.

5.2. Overview of the Existing Methods

There are several methods designed to determine the source of harmonics in power systems. This section describes some of the most common.

5.2.1. Active Power Direction Based Method

The most common method to identify harmonic sources is the active power direction-based method [100],[101],[102]. This is described using the instantaneous power at the

PCC of a given customer site, which is [1].

$$p(t) = v(t)i(t). \tag{5.1}$$

Instantaneous voltage and current at the PCC contain the fundamental component and all other harmonic components, which are presented as:

$$v(t) = \sum_{h=1}^{\infty} \sqrt{(2)}V_h \cos(h\omega_1 t + \varphi_h^v), \tag{5.2}$$

and

$$i(t) = \sum_{h=1}^{\infty} \sqrt{(2)}I_h \cos(h\omega_1 t + \varphi_h^i), \tag{5.3}$$

where ω_1 is the fundamental angular frequency of the supply, V_h and I_h are the respective rms values of the voltage and current at harmonic frequency $h\omega_1$, and φ_h^v and φ_h^i are the respective phase shifts of the hth harmonic with respect to a common reference.

The active power at the customer's PCC is thus

$$P_{PCC} = \frac{1}{T} \int_0^T p(t)dt \tag{5.4}$$

where T is the period of the supply voltage in seconds. If we substitute $v(t)$ and $i(t)$ into this equation, we obtain

$$P_{PCC} = \sum_{h=1}^{\infty} V_h I_h \cos\left(\varphi_h^v - \varphi_h^i\right) \tag{5.5}$$

This active power can be divided into active power at the fundamental frequency (P_1) and the active power at all other harmonics (P_H); i.e.

$$P_{PCC} = P_1 + P_H = V_1 I_1 \cos\left(\varphi_1^v - \varphi_1^i\right) + \sum_{h \neq 1}^{\infty} V_h I_h \cos\left(\varphi_h^v - \varphi_h^i\right). \tag{5.6}$$

---

[1]This section assumes that each customer has several loads at their own internal PCC. The aggregate current is $i(t)$ and the customer's PCC voltage is $v(t)$

To determine the source of the harmonics, once examines the sign of P_H. If P_H is positive, then harmonics flow from upstream to the load side, and thus the utility is the source. If P_H is negative, then harmonics flow upstream and the load is responsible. P_H is zero if linear loads are supplied from ideal sources, where harmonic components are zero. This method is intuitive and is very common in power quality devices. It has also been criticized, however, by some researchers. P_H depends on the phase shift between voltage and current at each harmonic. In general, some components will have a positive sign and some components have negative sign. It follows that the resulting active power P_H can be positive or negative and it can also be zero if the positive and negative components of the power are equal to each other. For example, an induction machine generates positive harmonics orders at 3rd, 7th, 11th ..., and negative sign harmonics orders at 5th, 9th, 11th .... The total harmonic power P_H could be negative, positive, or zero depending on the values of these harmonics. It follows that P_H cannot exactly resolve if an induction machine is the source of harmonics [98].

To avoid cancellation problems, the harmonic phasor index (HPI) was proposed [98]. The harmonic phasor index is defined as

$$\xi_{HPI} = \frac{\sqrt{\sum\limits_{h|P_h<0} I_h^2}}{\sqrt{I_1^2 + \sum\limits_{h\neq 1|P_h>0} I_h^2}} = \frac{I_{THD_L}}{\sqrt{1 + I_{THD_s}^2}}, \tag{5.7}$$

where I_{THD_L} denotes the norm of harmonic orders h for which harmonic active power is negative ($P_h < 0$) and I_{THD_S} denotes the norm of harmonic orders for which harmonic active power is positive ($P_h > 0$). If the loads generate harmonics and the supply system has background distortion, the harmonic phase index is generally greater than zero. The greater the index, the greater the responsibility of the customer; conversely, the lower the index, the greater the responsibility of the utility. This method refers only to currents, and the separation of terms in the numerator and the denominator depends on the sign of the

active power components. If the components contain errors, the final conclusion could be far from the correct answer as a result of the ratio effect.

If the contribution of harmonic distortion at the *h*-th harmonic frequency is a concern, then one could attempt to use a variation on the active power direction method [103] to measure the magnitude of the harmonic voltage V_{uh} at the utility side and the magnitude of the voltage V_{ch} at the customer side. This is done in [103]. If V_{uh} is large, the utility is the primary pollutant; otherwise it is the customer. the active power method is not an indicator of the main harmonic source [103]. This method can fail because active power depends on the phase angle between two harmonic sources, rather than the magnitude of the contribution. The equation for the simple case of a power system with only significant reactive impedance is

$$P = V_{uh}I_h\cos\theta = \frac{V_{uh}V_{ch}}{X}\sin\delta \tag{5.8}$$

where V_{uh} and V_{ch} are the harmonic voltages contributed by the utility and the customer at the PCC, respectively, and δ is the phase angle between the two voltages at the h-th harmonic frequency. From this equation, it is clear that this variant of the active power direction-based harmonic source detection method is incorrect theoretically, as it cannot reveal the difference between the magnitudes of the two sources.

A new single-point method based on harmonic powers different from the active power was published recently. This proposal has the aim of identifying the harmonic source by comparing some non-active powers, i.e. the fundamental reactive power, Fryze's reactive power, and the quadrature reactive power proposed by Sharon [104]. Mazumda proposed a method to determine current THD and harmonics sources based on neural network theory [45].

5.2.2. Critical Impedance based method

The critical impedance based method has been proposed to determine whether the utility or the customer is the main source of current harmonics. Rather than evaluating the

active power direction, this method estimates reactive power at each harmonic order.

In the Thevenin equivalent circuit shown in the Figure 5.2, the problem of determining the dominant harmonic source is equivalent to the investigation of the relationship between magnitude of harmonic voltages V_{ch} and V_{uh}. In this circuit, the phase angle of V_{uh} is defined to be zero and that of V_{ch} is denoted as δ. The total impedance Z_h is the sum of the customer side impedance Z_{ch} and the utility side impedance Z_{uh} referred to the PCC. In order to calculate the Critical Impedance index, the utility impedance Z_{uh} and the customer impedance Z_{ch} should be approximately known.
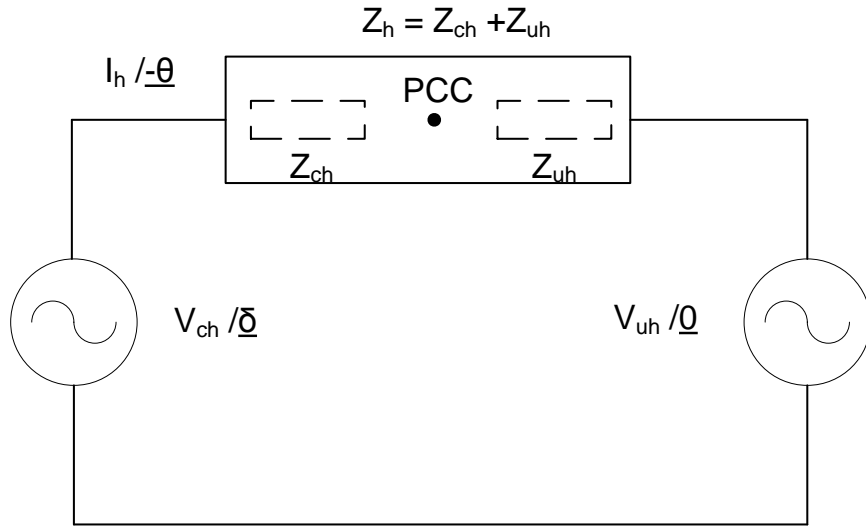
Figure 5.2: Thevenin equivalent circuit for utility and load system.

Consider the simplified case in which the impedances are purely reactive, that is $|Z_{ch}|$ = X_{ch}, $|Z_{uh}| = X_{uh}$. Reactive power exchanged in the power system mainly depends on the magnitude of the voltage sources and is calculated as [47]

$$Q_{uh} = \text{Im}(\bar{V}_{uh}\bar{I}_h^*) = \frac{V_{uh}}{X_{uh} + X_{uh}}\left(V_{ch}\cos\delta - V_{uh}\right). \tag{5.9}$$

From this equation, reactive power can be used to determine the direction of harmonic voltage and therefore, harmonic current between the utility and the customer. For example, if the utility absorbs reactive power $Q_{uh} > 0$, V_{uh} must be smaller than V_{ch}. In other

words, one can conclude that the customer side has a larger contribution to the harmonic current distortion I_h at the PCC. If $Q_{uh} < 0$, the reactive power from the utility may not reach the customer because the total reactive impedance $X_{uh}+X_{ch}$ absorbs reactive power. Thus, additional investigation must be performed to determine which source of harmonics is dominant in the power system.

This method presumes the total impedance $Z_h = jX_h$ defined as 'line impedance' is uniformly distributed between the sources V_{ch} and V_{uh}. The amount of impedance in this line which absorbs all of reactive power Q_{uh} from the utility is:

$$x = -\frac{Q_{uh}}{I_h^2} \tag{5.10}$$

The necessary and sufficient condition for $Q_{uh} < 0$ is proven as [105]:

- If x is located closer to the customer side ($x > X_h/2$), the utility source is expected to have a larger magnitude ($V_{uh} > V_{ch}$) since the source can 'push' its reactive power output beyond half ($X_h/2$) of the 'line impedance'.

- If $x < X_h/2$ or x is located closer to the utility side, the customer source is expected to have a large magnitude ($V_{ch} > V_{uh}$).

A method to determine the relative magnitude of the two sources can, therefore, be established on the basis of comparing the magnitudes of x and $X_h/2$. The Critical Impedance index is defined as:

$$CI = -2x = 2\frac{Q_{uh}}{I_h^2} \tag{5.11}$$

Knowledge of the utility impedance Z_{uh} and customer impedance Z_{ch} is required, though these values change unpredictably in the power system. Thus, the method assumes that

these values lie in a known range, in this case $[X_{hmin}, X_{hmax}]$. In order to determine whether the utility or customer is mainly responsible for the harmonic current distortion, the following procedure is proposed:

1. If $CI > 0$ ($Q_{uh} > 0$), the customer side is the dominant harmonic current source at the PCC.

2. If $CI < 0$ ($Q_{uh} < 0$), the following cases are considered:

(a) if $|CI| > X_{hmax}$, then $x > X_{hmax}/2$, and the utility side is the dominant harmonic current source at the PCC;

(b) if $|CI| < X_{hmin}$, then $x < X_{hmin}/2$, and the customer side is the dominant harmonic current source at the PCC;

(c) if $X_{hmin} < |CI| < X_{hmax}$, it is not possible to conclude which entity is the dominant harmonic current source at the PCC.

In general, the resistance of the power line is not negligible, and the impedance has the form of $Z = R + jX$. The Critical Impedance index derived above can be generalized by taking into account the total harmonic impedance Z_h and its phase angle β. A transformed reactive power Q_{uh}^t will replace Q_{uh} to investigate the dominant harmonic source. The generalized Critical Impedance index becomes:

$$CI = 2\frac{Q_{uh}^t}{I_h^2} = 2\frac{V_{uh}}{I_h}\sin(\delta + \beta) \qquad (5.12)$$

Once the approximate range of the total impedance Z_h is known, the CI index value can be obtained and the above procedure can be applied by substituting the impedances for the reactances.

The Critical Impedance (CI) index can be used to determine the responsibility of harmonic current at the PCC. To determine which harmonic voltage source is the dominant harmonic source at the PCC, the similar Critical Admittance (CA) index can be used.

As previously shown, the relationships defining the indices require knowledge of the measured voltage and current waveforms at the PCC, as well as the harmonic impedances

of both the utility supply system and the customer installation as seen from the PCC. While the two former quantities are measured easily, for example, using Fourier analysis, the harmonic impedances of the utility and the customer are time varying and difficult to measure. This chapter utilizes the online impedance measurement method proposed in Chapter 3 to determine whether the utility or the customer is the dominant harmonic source in the power system.

5.3. Proposed Method for Determination of the Main Harmonics Sources

This section presents a method for determining the main harmonic source using the 'critical impedance' based method. The Thevenin equivalent circuit seen by the k-th customer is shown in the Figure 5.3(a) where V_{ks} is the equivalent source voltage at the k-th customer, Z_{ks} is the equivalent grid impedance at k-th customer, Z_{kl} is the load impedance of the k-th customer, and I_{kl} is the harmonic current injected by the k-th customer.
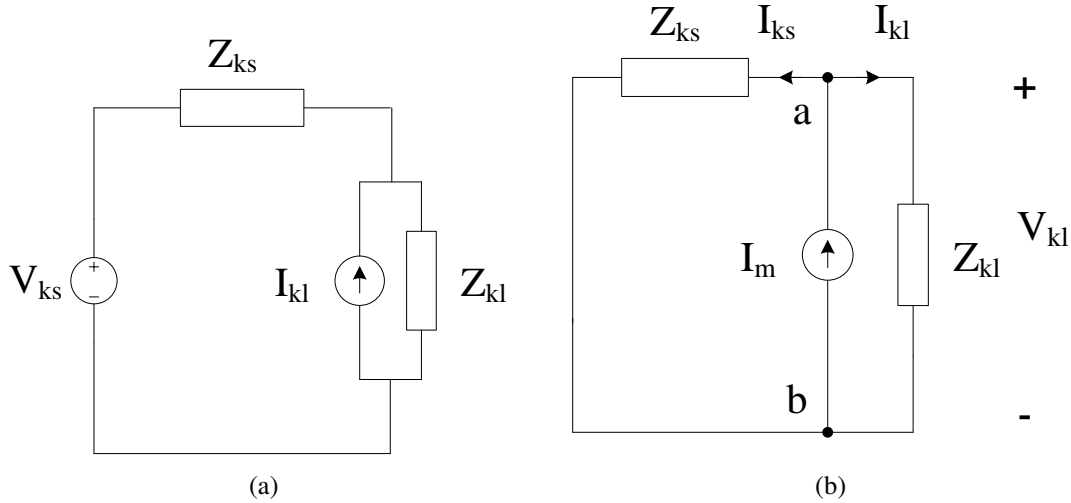
Figure 5.3: (a) Equivalent circuit at k-th load
(b) The impedance measurement architecture.

The original paper about this method assumed that impedances of the source side and load side are known. This assumption may be reasonable in some cases, but not always. As loads and sources are connected/disconnected at any time, the value of impedances also

vary unpredictably. Consequently, the need to assume impedances in the source side and load side limit the 'critical impedance' based method.

5.3.1. Load and source impedance measurement

One of the main advantages of the method discussed in this section is the ability to determine harmonic sources at any point in the power system. For instance, the utility can install a device at the PCC to determine whether customers inject harmonics into the grid or if the distortion is preexisting. On the other hand, a customer who wants to avoid extra charges for the amount of harmonics they do not consume can integrate the measuring unit at its power entry module.

Figure 5.3(b) shows the architecture for measuring both the utility and load side impedances at the same time. A small alternating current I_m is injected between point a and point b. A current I_{kl} flow to the load and an current I_{ks} flows to the utility. These currents are monitored along with the voltage v_{kl} to estimate Z_{ks} and Z_{kl}. It is wroth noting that to estimate the impedance at certain harmonics, the frequency of the injected current should be close to the harmonic frequency. In the example considered below, the 3rd harmonic component is monitored and the injected frequency is at 175 Hz.

In general, the load impedance is much larger than the source impedance, so that the current flowing to the load is much smaller than the current flowing to the source, making the measurement an obstacle. This difficulty can be overcome by using the MLE impedance measurement method presented in Chapter 3.

5.3.2. Application of 'critical impedance' based method

Using the 'critical impedance' based method requires calculation of the equivalent parameters at the appropriate harmonic frequency. Figure 5.4(a) shows an equivalent circuit for h-th harmonic at the k-th consumer load.

The phasor diagram shown in Figure 5.4(b) indicates that the voltage drop on the grid
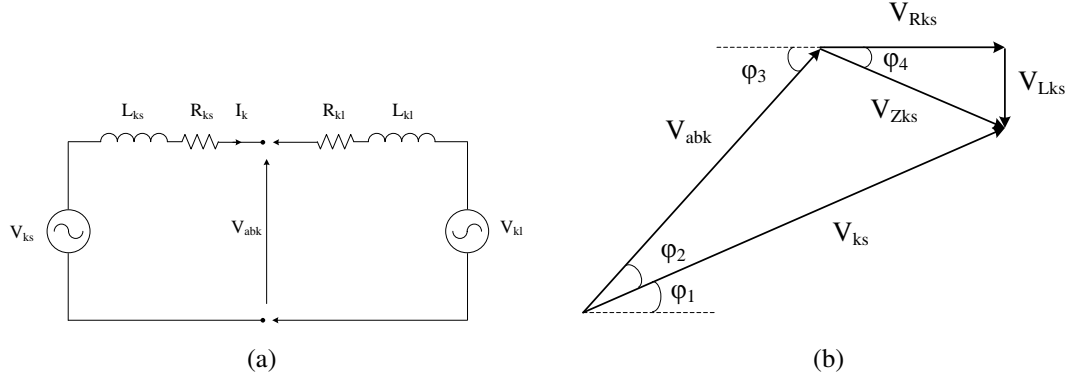
Figure 5.4: (a) Equivalent circuit for h-th harmonic at the k-th customer. (b) Phasor analysis of the circuit.

impedance Z_{ks} is calculated as

$$V_{Zks} = \sqrt{V_{Lks}^2 + V_{Rks}^2}.$$ (5.13)

The magnitude of the equivalent voltage source is

$$V_{ks} = \sqrt{V_{Zks}^2 + V_{abk}^2 - 2V_{Zks}V_{abk}\cos(\pi - \varphi_3 - \varphi_4)}.$$ (5.14)

The phase shift between the source voltage and v_{abk} is determined trigonometrically as

$$\sin(\varphi_2) = \frac{V_{Zks}}{V_{abk}} \sin(\pi - \varphi_3 - \varphi_4).$$ (5.15)

The phase angle of the equivalent voltage source is

$$\varphi_1 = \varphi_3 - \varphi_2,$$ (5.16)

so that the equivalent voltage source at the hth harmonic will be in the form of

$$v_{ks} = V_{ks}\cos(h\omega t + \varphi_1).$$ (5.17)

where ω is the angular velocity of the fundamental frequency. The 'critical impedance' based method determines the sources of harmonics by comparing the critical impedance (CI) index with the magnitude of system impedance $|Z_{total}|$. The CI is calculated from:

$$CI = 2\frac{V_{abk}}{I_k}\sin(\varphi_1 + \beta).\tag{5.18}$$

where

$$\beta = \tan^{-1}\left(\frac{X_{kl} + X_{ks}}{R_{kl} + R_{ks}}\right).\tag{5.19}$$

The magnitude of the total system impedance is:

$$|Z| = \sqrt{(X_{kl} + X_{ks})^2 + (R_{kl} + R_{ks})^2}.\tag{5.20}$$

The conclusions are thus:

- If CI > $|Z|$, then the utility side is the main source at the h-th harmonic.

- If CI < $|Z|$, then the load side is the main source at the h-th harmonic.

In addition of measuring impedances, this proposed method has other advantages over the method in the original paper [105]. Most importantly, the accuracy and online nature of the proposed measurement scheme are highly beneficial. The error in determining the source of harmonics can thus be reduced.

5.3.3. Simulation Results

In order to verify the proposed method, a simulation circuit was built using Matlab/Simulink as shown in the Figure 5.5. In this example, three types of loads were connected to the PCC and supplied by the pure sinusoidal source. One load is purely resistive load (i.e. lamp load), one load is a DC motor connected through a full bridge rectifier; the other load is an AC induction machine connected through an AC/AC converter. The

Table 5.1: Simulation results for determining of harmonic sources.

Load	V_1	I_1	$\phi 1R$	V1S	$\phi 1$	β	**CI**	**|Z|**
Lamp	11.39	0.12	0.0	11.39	0.0	1.56	**−194.30**	**97.16**
Rectifier	12.38	3.02	0.58	14.56	0.32	0.72	**−8.29**	**17.12**
Drive	11.72	2.64	1.13	11.79	0.75	1.34	**−7.71**	**6.08**

impedances take into account all cables, transformers, and circuit breakers. A non-interrupt meter measures current, voltage, and estimates equivalent load and source impedances. The simulation results for determining the source of 3rd harmonic at 3 different loads measured are shown in the Table 5.1.
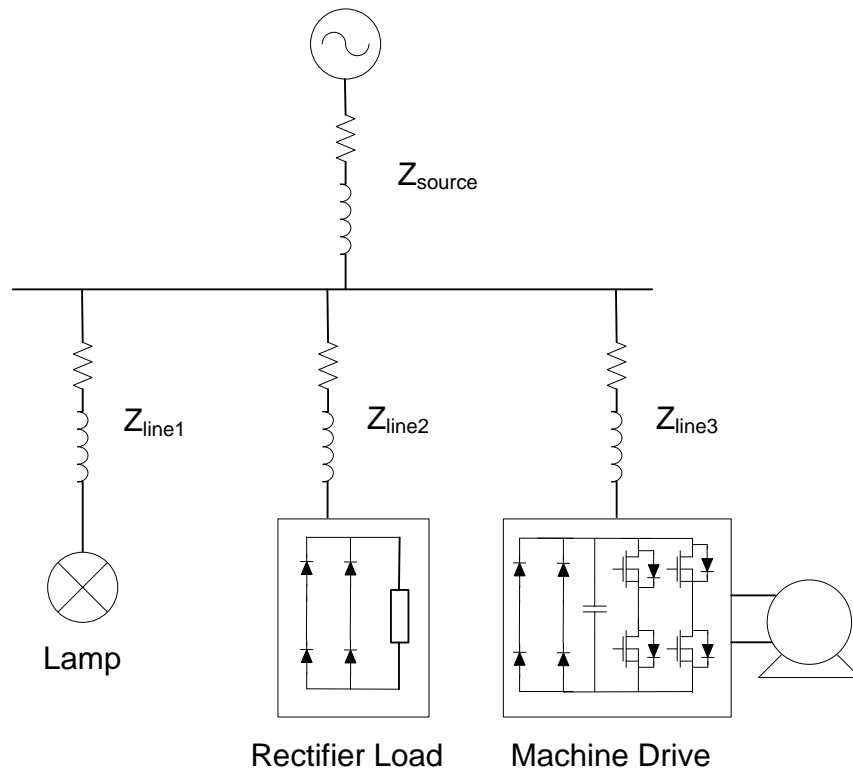
Figure 5.5: Simulation circuit for determination of harmonics sources.

Several conclusions about harmonic sources can be drawn from the Table 5.1

- Load 1 absorbs 3rd harmonic power from the utility (because |CI| > |Z|).

- Load 2 is the main 3rd harmonic source (because |CI| < |Z|).

- Load 3 absorbs 3rd harmonic power from the utility, but also generate harmonics to grid (because |CI|≈|Z|). This conclusion can not be drawn by previous Critical Index method [105], because the method shown in this section has be able to measure absolute value of impedance and does not need to assume range of impedances.

CHAPTER 6: CONCLUSIONS AND FUTURE WORKS

6.1. Conclusions

The sustainability and reliability of modern power systems has necessitated the use of switched-mode converters and power electronics based distributed systems. Despite the many advantages of the PEBDS, they have also presented challenges for system designers in guaranteeing reliable operations, stability and performance of the systems in terms of different design issues and impedance interactions that must be considered. The interaction of impedances within the systems may compromise the stability and performance of the individual converters and systems. Previous work on this topic focused relied heavily on the a priori information of impedances to proposed conservative requirements of power electronics designs. As the modern power systems are highly dynamic, the systems can be changed unpredictably; any change thus leads to instability of the power electronics and the instabilities can propagate throughout the network. Moreover, conventional impedance measurement schemes require complex, expensive devices and large disturbances signals. These have been limiting factors in many applications. This thesis presents a possible solution for the incorporation of high levels of power electronics in power systems.

The first contribution of this thesis is a practical and systematic technique to determine one of the key harmonic parameters in power systems, network impedance. The method is practical, efficient and experimental results shown better accuracy than other popular methods. The implementation cost is not significant, and can be implemented with hand-held clip-on devices. Additional scientific contribution on this topic can be summarized as follows:

- Network impedance is measured under energized conditions without any requirement of external disturbances. The signals used to estimate of network impedance already existed in a network with high levels of power electronics.

- Only input current is needed, so the error of the measurement process is much reduced in compared with the traditional FFT method, which calculates ratios of FFT for both input voltage and current.

- The proposed method for detection of small signals is benefited from a technique common in non-coherent receivers, a so-called Maximum Likelihood Estimation (MLE). The power line is the communications channel, a small interharmonic signal is circulated on this channel between the nonlinear load and the network. The interharmonic signals that needs to be detected is several orders of magnitude smaller than the fundamental and other harmonics components.

- A new MLE algorithm is proposed to increase the accuracy of estimation of the small signal and to avoid burdensome calculations. Compared to a brute-force search, the proposed algorithm for the detection of small signal reduces significant search space, e.g., hundred thousand times for $1\mu Hz$ frequency resolution.

The second contribution of the thesis is to improving the stability of a grid-connected Power Factor Converting (PFC) converter in the modern power systems. This work demonstrates common interaction problems and provides a solution which can be applied for stability of many power converters connected in the highly dynamic power systems. With this method, the power converter controller can be autotuned adaptively on-line with few additional resources and minimum interfering with the current system, paving the way to successful commercial application. The main scientific contribution on this topic can be summarized as follows:

- Modeling input impedance of the boost PFC converter is block-based method. The

model explains the structure of the converter input admittance, and set a groundwork for development of stability analysis for power converters.

- A new adaptive compensator is proposed for stabilization of the PFC converter, when the input voltage, output power or network impedance are change. The method benefits from online impedance information which is measured in the previous work, and an adaptive compensator contains that information as a reflection of network dynamic.

- A digitally controlled PFC converter is built in laboratory which embedded new adaptive compensator. This digital power converter provides a flexible ability, and can be applied for different network impedance models and also different input filter stages. This method is straightforward, can be implemented in many other power converter topologies.

- This method is useful in applications of high level of power electronics such as all electric ship, vehicle, and aircraft power system. The adaptive converter is load-invariant and line-voltage-invariant.

The third contribution of this thesis is the determination of source harmonics in the power systems. Standards like IEEE 519 provide guidelines for controlling harmonic distortion levels that divide the responsibility between the utility and the customer. The utility has to maintain voltage distortion at the PCC below the specified limits and the customer has to limit the amount of harmonic current injection onto the utility system. However, disputes may arise between utilities and customers regarding who is responsible for the harmonic distortions due to the lack of a reliable single index which can precisely point out the source of the harmonic pollution. The information about the source of harmonics using a 'Critical impedance'-based method could be used to penalize the offending customer. The measurement of load impedance and source impedance proposed in this research avoids disconnecting or disrupting the operation of any loads from the system. On a

practical system the determination of network disturbance sources could be carried out on a DSP. A suitable A/D interface is required for acquiring the measured values of voltages and currents. Such a system could be installed permanently or be portable from one customer to another in order to simply monitor pollution levels at a particular PCC in the network.

6.2. Future Works

The accurate estimation of network impedance is fundamental in characterizing frequency responses, power flow analysis, and stability analysis of power systems. The on-line impedance measurement method can be extended to unbalanced three phase systems. Working with real measurements significantly increases the difficulty level of power system parameter estimation. Implementation issues such as the energy of the disturbance, phase shift, channel synchronization and load variation have an important influence on the reliability of the results.

Network impedance studies are important stepping stone for developing potential applications such as harmonics propagations, and assessing harmonic limits, harmonic sources determination, which has been explored in the thesis. Future research could focus on quantifying the relative impact of each source. After the harmonic sources contained in both the customer and utility systems have been determined, the harmonic contributions due to a customer and its supply system could be the next step in the harmonic analysis.

Microgrid systems can operate in grid-connected mode or isolated mode. Some transient problems occur during the transition between stand-alone mode and grid-tied mode. Islanding detection and resynchronization methods could be a good research topic for the future. Improving the stability of other power electronics in grid-tied applications such as FACTS (STATCOM, UPFC, etc.) could also be looked at in the future. These devices are designed assuming a strong source, and the dynamics of the grid are ignored. However, in many cases, the grid is not stiff, and the dynamics will affect the control performance as well. Impedance, capacitance and resistance are the fundamental components of all power

systems and power electronics. Knowledge about these components will have numerous applications in practice. These components are dependent upon time, frequency, temperature, power level and so on; more powerful methods taking account to these factors could be a future research topic.

REFERENCES

[1] A. Ipakchi and F. Albuyeh, "Grid of the future," *IEEE power & energy magazine*, vol. 9, pp. 52–62, 2009.

[2] N. G. Hingorani and M. F. Burbery, "Simulation of ac system impedance in hvdc system studies," *IEEE Trans. Power App. Syst.*, no. 5, pp. 820–828, 1970.

[3] B. K. Bose, *Power Electronics and Motor Drives Advances and Trends*. Academic Press, 2006.

[4] N. Mohan, T. M. Undeland, and W. Robbins, *Power Electronics: Converters, Applications and Design*. Wiley & Sons, 2003.

[5] S. H. Horowitz, A. G. Phadke, and B. A. Renz, "The future of power transmission," *IEEE Power & Energy*, pp. 34–41, 2010.

[6] P. K. Steimer, "Enabled by high power electronics - energy efficiency, renewables and smart grids," pp. 11–15, 2010.

[7] D. G. Fink and H. W. Beaty, *Standard Handbook for Electrical Engineers*. McGraw-Hill Professional, 2006.

[8] J. Arai, K. Iba, T. Funabashi, Y. Nakanishi, K. Koyanagi, and R. Yokoyama, "Power electronics and its application to renewable in japan," *IEEE Circuit and System Magazine*, pp. 52–66, 2008.

[9] DOE, "The smart grid introduction," 2008.

[10] R. Strzelecki and G. Benysek, *Power Electronics in Smart Electrical Energy Networks*. Springer, 2008.

[11] M. Rashid, *Power electronics handbook*. Academic Press, 2006.

[12] P. d. Mello, "Share your thoughts," *IEEE Power & Energy*, vol. 8, no. 5, 2010.

[13] *IEEE Recommended Practices and Requirements for Harmonic Control in Electrical Power Systems, ANSI/IEEE Std. 519-1992*, Std.

[14] C. Calwell and T. Reeder, "Power supplies: A hidden opportunity for energy savings," Natural Resources Defense Council, Tech. Rep., 2002.

[15] J. Pyrhonen, T. Jokinen, and V. Hrabovcova, *Design of Rotating Electrical Machines*. Wiley, 2009.

[16] A. Hughes, *Electric Motors and Drives: Fundamentals, Types and Applications*, 2005.

[17] B. Drury, *The Control Techniques Drives and Controls Handbook*. Institution of Engineering and Technology, 2009.

[18] M. Barnes, *Practical Variable Speed Drives and Power Electronics*. Newnes, 2003.

[19] E. Fuchs, *Power Quality in Power Systems and Electrical Machines*. Academic Press, 2008.

[20] M. H. Bollen, *Signal Processing of Power Quality Disturbances*. Wiley-IEEE Press, 2006.

[21] J. Arrillaga and N. R. Watson, *Power system harmonics*. Wiley, 2003.

[22] M. Eissa, S. Leeb, G. Verghese, and A. Stankovic, "Fast controller for a unity-power-factor pwm rectifier," *IEEE Transaction on power electronics*, vol. 11, no. 1, pp. 1–6, 1996.

[23] J. Sun, "AC power electronic systems: stability and power quality," in *11th Workshop on Control and Modeling for Power Electronics*, 2008.

[24] P. Todd, "Uc3854 controlled power factor correction circuit design," 1995.

[25] R. W. Erickson and D. Maksimovic, *Fundamentals of Power Electronics*, 2, Ed. Springer, 2001.

[26] R. D. Middlebrook, "Input filter consideratlons in design and application of switching regulators," in *IEEE Industry Applications Society Annual Meeting*, 1976, pp. 366–382.

[27] H. Y. Cho and E. Santi, "Modeling and stability analysis in multi-converter systems including positive feedforward control," *34th Annual Conference of IEEE Industrial Electronics*, pp. 839 – 844, 2008.

[28] D. Mitchell, "Power line filter design considerations for dc-dc converters," *IEEE Industry Applications Magazine*, vol. 5, no. 6, pp. 16–26, 1999.

[29] L. Corradini, P. Mattavelli, M. Corradin, and F. Polo, "Analysis of parallel operation of uninterruptible power supplies loaded through long wiring cables," *IEEE Transaction on Power Electronics*, vol. 25, no. 4, pp. 1046–1054, 2010.

[30] C. D. Davidson and R. Szasz, "Compatibility of switchmode rectifiers with engine generators," in *Proc. INTELEC Telecommunications Energy Conf. Twenty-second Int*, 2000, pp. 626–631.

[31] C. M. Hoff and S. Mulukutla, "Analysis of the instability of "pfc" power supplies with various "ac " sources," in *Proc. 1994. Ninth Annual Applied Power Electronics Conf and Exposition APEC '94*, 1994, pp. 696–702.

[32] G. Spiazzi, L. Rossetto, and J. A. Pomilio, "Analysis of emi filter induced instabilities in boost power factor preregulators," in *Proc. PESC 98 Record Power Electronics Specialists Conf. 29th Annual IEEE*, vol. 2, 1998, pp. 1048–1053.

[33] M. Li, D. Dai, and X. Ma, "Effects of the input filter on the stability of a voltage-mode controlled buck converter," *International journal of circuit theory and applications*, pp. 367–373, 2008.

[34] Y. Panov and M. Jovanovic, "Practical issues of input/output impedance measurements in switching power supplies and application of measured data to stability analysis," in *Proc. Twentieth Annual IEEE Applied Power Electronics Conf. and Exposition APEC 2005*, vol. 2, 2005, pp. 1339–1345.

[35] V. Vlatkovic, D. Borojevic, and F. C. Lee, "Input filter design for power factor correction circuits," *IEEE Transaction on power electronics*, vol. 11, no. 1, pp. 199–206, 1996.

[36] C. H. Rivetta, A. Emadi, G. A. Williamson, R. Jayabalan, and B. Fahimi, "Analysis and control of a buck dc-dc converter operating with constant power load in sea and undersea vehicles," *IEEE Trans. Ind. Appl.*, vol. 42, no. 2, pp. 559–572, 2006.

[37] K. P. Louganski and J. S. Lai, "Current phase lead compensation in single-phase "pfc" boost converters with a reduced switching frequency to line frequency ratio," *IEEE Trans. Power Electron.*, vol. 22, no. 1, pp. 113–119, 2007.

[38] L. Asiminoaei, R. Teodorescu, F. Blaabjerg, and U. Borup, "A digital controlled PV-inverter with grid impedance estimation for ENS detection," *IEEE Trans. Power Electron.*, vol. 20, no. 6, pp. 1480–1490, Nov. 2005.

[39] T. L. Baldwin, M. J. Hittel, L. F. Saunders, and J. Renovich, F., "Using a microprocessor-based instrument to predict the incident energy from arc-flash hazards," *IEEE Trans. Ind. Appl.*, vol. 40, no. 3, pp. 877–886, May 2004.

[40] A. Robert and T. Deflandre, "Guide for assessing the network harmonic impedance," in *Proc. Electricity Distribution. Part 1: Contributions. CIRED. 14th International Conference and Exhibition on (IEE Conf. Publ. No. 438)*, vol. 1, 1997, pp. 3/1–310.

[41] M. Sumner, B. Palethorpe, and D. Thomas, "Impedance measurement for improved power quality. Part 1: The measurement technique," *IEEE Trans. Power Del.*, vol. 19, pp. 1442–1448, JULY 2004.

[42] S. R. Shaw, C. R. Laughman, S. B. Leeb, and R. F. Lepard, "A power quality prediction system," *IEEE Trans. Ind. Electron.*, vol. 47, no. 3, pp. 511–517, Jun. 2000.

[43] J. P. Rhode, A. W. Kelley, and M. E. Baran, "Complete characterization of utilization-voltage power system impedance using wideband measurement," *IEEE Trans. Ind. Appl.*, vol. 33, no. 6, pp. 1472–1479, Nov. 1997.

[44] A. A. Girgis, W. H. Quaintance, J. Qiu, and E. B. Makram, "A time-domain three-phase power system impedance modeling approach for harmonic filter analysis abstract |full text: Pdf (576kb)," *IEEE Trans. Power Del.*, vol. 8, no. 2, pp. 504–510, Apr 1993.

[45] J. Mazumdar, R. G. Harley, and F. Lambert, "System and method for determining harmonic contributions from non-linear loads using recurrent neural networks," in *Proc. IEEE Int. Joint Conf. Neural Networks IJCNN '05*, vol. 1, 2005, pp. 366–371.

[46] K. H. LaCommare and J. H. Eto, "Understanding the cost of power interruptions to u.s. electricity consumers," Lawrence Berkeley National Laboratory, Tech. Rep., 2004.

[47] J. Grainger and W. S. Jr., *Power System Analysis*. McGraw-Hill Science/Engineering/Math, 1994.

[48] W. H. Kersting, *Distribution system modeling and analysis*. CRC Press, 2002.

[49] J. D. Glover, M. S. Sarma, and T. Overbye, *Power Systems Analysis and Design*. CL-Engineering, 2007.

[50] T. Short, *Electric Power Distribution Handbook*. CRC Press, 2007.

[51] J. R. Carson, "Wave propagation in overhead wires with ground return," *Bell Systems Technical Journal*, vol. 5, pp. 539–554, 1926.

[52] A. S. Morched and P. Kundur, "Identification and modelling of load characteristics at high frequencies," *IEEE Trans. Power Syst.*, vol. 2, no. 1, pp. 153–159, 1987.

[53] J. G. Kassakian, *Principles of Power Electronics*. Prentice Hall, 1991.

[54] X. Feng, J. Liu, and F. C. Lee, "Impedance specifications for stable dc distributed power systems," *IEEE Transaction on power electronics*, vol. 17, no. 2, pp. 157–163, 2002.

[55] K. L. F. R. J. P. Y. M. B. Gholdston, E.W.; Karimi, "Stability of large dc power systems using switching converters, with application to the international space station," *Proceedings of the 31st Intersociety Energy Conversion Engineering Conference*, pp. 166 – 171, 1996.

[56] A. Emadi, , M. Ehsani, and J. M. Miller, *Vehicular Electric Power Systems: Land, Sea, Air, and Space Vehicles*. CRC Press, 2003.

[57] S. D. Sudhoff, S. F. Glover, P. T. Lamm, D. H. Schmucker, and D. E. Delisle, "Admittance space stability analysis of power electronic systems," *IEEE Trans. Aerosp. Electron. Syst.*, vol. 36, no. 3, pp. 965–973, 2000.

[58] F. Z. Peng, Y. W. Li, and L. M. Tolbert, "Control and protection of power electronics interfaced distributed generation systems in a customer-driven microgrid," in *Proc. IEEE Power & Energy Society General Meeting PES '09*, 2009, pp. 1–8.

[59] A. Emadi, A. Khaligh, C. H. Rivetta, and G. A. Williamson, "Constant power loads and negative impedance instability in automotive systems: Definition, modeling, stability, and control of power electronic converters and motor drives," *IEEE Transactions on vehicular technology*, vol. 55, no. 4, pp. 1112–1126, 2006.

[60] C. M. Wildrick, F. C. Lee, B. H. Cho, and B. Choi, "A method of defining the load impedance specification for a stable distributed power system," *IEEE Trans. Power Electron.*, vol. 10, no. 3, pp. 280–285, 1995.

[61] M. H. J. Bollen, *Understanding power quality problems: voltage sags and interruptions*.   IEEE Press, 2002.

[62] *IEEE Guide for Performing Arc-Flash Hazard Calculations*, IEEE Std. 1584-2002.

[63] J. Sun, "Input impedance analysis of single-phase pfc converters," *IEEE Transaction on power electronics*, vol. 20, no. 2, pp. 308–315, 2005.

[64] A. Baggini, *Handbook of power quality*.   Wiley, 2008.

[65] M. Liserre, R. Teodorescu, and F. Blaabjerg, "Stability of grid-connected PV inverters with large grid impedance variation," in *Proc. IEEE 35th Annual Power Electronics Specialists Conference PESC 04*, vol. 6, 2004, pp. 4773–4779.

[66] F. T. R. Liserre, M. Blaabjerg, "Grid impedance estimation via excitation of LCL-filter resonance," *IEEE Trans. Ind. Appl.*, vol. 43, pp. 1401–1407, 2007.

[67] A. Tarkiainen, R. Pollanen, M. Niemela, and J. Pyrhonen, "Identification of grid impedance for purposes of voltage feedback active filtering," *IEEE Power Elecron. Lett.*, vol. 2, no. 1, pp. 6–10, Mar. 2004.

[68] S. Cobreces, E. J. Bueno, D. Pizarro, F. J. Rodriguez, and F. Huerta, "Grid impedance monitoring system for distributed power generation electronic interfaces," *IEEE Trans. Instrum. Meas.*, vol. 58, no. 9, pp. 3112–3121, Sep. 2009.

[69] J. Huang, K. A. Corzine, and M. Belkhayat, "Small-signal impedance measurement of power-electronics-based AC power systems using line-to-line current injection," *IEEE Trans. Power Electron.*, vol. 24, no. 2, pp. 445–455, Feb. 2009.

[70] M. Tsukamoto, S. Ogawa, Y. Natsuda, Y. Minowa, and S. Nishimura, "Advanced technology to identify harmonics characteristics and results of measuring," in *Proc. 9th Int. Conf. on Harmonics and Quality of Power*, vol. 1, Orlando, FL, 2000, pp. 341–346.

[71] M. Sumner, B. Palethorpe, D. W. P. Thomas, P. Zanchetta, and M. C. D. Piazza, "A technique for power supply harmonic impedance estimation using a controlled voltage disturbance," *IEEE Trans. Power Electron.*, vol. 17, no. 2, pp. 207–215, Mar 2002.

[72] W. C. Beattie and S. R. Matthews, "Impedance measurement on distribution networks," in *Proc. 29th Universities Power Engineering Conf.*, Sep 1994, pp. 117–120.

[73] A. A. Girgis and R. B. McManis, "Frequency domain techniques for modeling distribution or transmission networks using capacitor switching induced transients," *IEEE Trans. Power Del.*, vol. 4, no. 3, pp. 1882–1890, Jul. 1989.

[74] M. Ciobotaru, R. Teodorescu, and F. Blaabjerg, "On-line grid impedance estimation based on harmonic injection for grid-connected PV inverter," in *Proc. IEEE International Symposium on Industrial Electronics ISIE 2007*, 2007, pp. 2437–2442.

[75] K. Pedersen, A. Nielsen, and N. Poulsen, "Short-circuit impedance measurement," *Proc. Inst. Elect. Eng. - Gener., Transm., Distrib.*, vol. 150, no. w, pp. 169–174, Mar 2003.

[76] S. Nandi, H. A. Toliyat, and X. Li, "Condition monitoring and fault diagnosis of electrical motors - A review," *IEEE Trans. Energy Convers.*, vol. 20, no. 4, pp. 719–729, Dec. 2005.

[77] D. Lee, B. Choi, J. Sun, and B. H. Cho, "Interpretation and prediction of loop gain characteristics for switching power converters loaded with general load subsystem," in *Proc. IEEE 36th Power Electronics Specialists Conf. PESC '05*, 2005, pp. 1024–1029.

[78] A. D. Whalen, *Detection of signals in noise*.   Academic Press, 1971.

[79] A. J. Viterbi, *Principles of coherent communication*.   McGraw Hill, 1966.

[80] W. M. Siebert, *Circuits, signals, and systems*.   McGraw Hill, 1986.

[81] L. Asiminoaei, R. Teodorescu, F. Blaabjerg, and U. Borup, "A new method of on-line grid impedance estimation for PV inverter," in *Proc. Nineteenth Annual IEEE Applied Power Electronics Conference and Exposition APEC '04*, vol. 3, 2004, pp. 1527–1533.

[82] S. M. Kay, *Modern Spectral Estimation: Theory and Application*.   Prentice Hall, 1999.

[83] H. L. V. Trees, *Detection, estimation, and modulation theory, part I*.   Wiley, 2001.

[84] W. Gould, J. Pitblado, and S. William, *Maximum Likelihood Estimation with Stata*. Stata Press, 2007.

[85] T. Apostol, *Mathematical analysis*.   Addison-Wesley, 1974.

[86] M. S. Puckette and J. C. Brown, "Accuracy of frequency estimates using the phase vocoder," *IEEE Trans. Speech Audio Process.*, vol. 6, no. 2, pp. 166–176, Mar. 1998.

[87] S. V. Vaseghi, *Advanced digital signal processing and noise reduction*. Wiley, 2000.

[88] M. Jabloun, F. Leonard, M. Vieira, and N. Martin, "A new flexible approach to estimate the IA and IF of nonstationary signals of long-time duration," *IEEE Trans. Signal Process.*, vol. 55, no. 7, pp. 3633–3644, Jul. 2007.

[89] C. Kral, T. G. Habetler, and R. G. Harley, "Detection of mechanical imbalances of induction machines without spectral analysis of time-domain signals," *IEEE Trans. Ind. Appl.*, vol. 40, no. 4, pp. 1101–1106, Jul/Aug 2004.

[90] V. M. Rao, A. K. Jain, K. K. Reddy, and A. Behal, "Experimental comparison of digital implementations of single-phase pfc controllers," *IEEE Trans. Ind. Electron.*, vol. 55, no. 1, pp. 67–78, 2008.

[91] A. de Oliveira, J. C. de Oliveira, J. W. Resende, and M. S. Miskulin, "Practical approaches for "ac" system harmonic impedance measurements," *IEEE Trans. Power Del.*, vol. 6, no. 4, pp. 1721–1726, 1991.

[92] D. Maksimovic, A. M. Stankovic, V. J. Thottuvelil, and G. C. Verghese, "Modeling and simulation of power electronic converters," *Proc. IEEE*, vol. 89, no. 6, pp. 898–912, 2001.

[93] P. V. Tran and R. W. Cox, "Measuring line impedances using inter-harmonics generated by electrical loads," April 2010, submitted to IEEE Trans. on Power Delivery.

[94] J. Rajagopalan, J. G. Cho, B. H. Cho, and F. C. Lee, "High performance control of single-phase power factor correction circuits using a discrete time domain control method," in *Proc. 1995. Tenth Annual Applied Power Electronics Conf and Exposition APEC '95*, no. 0, 1995, pp. 647–653.

[95] K. De Gusseme, D. M. Van de Sype, and J. A. A. Melkebeek, "Design issues for digital control of boost power factor correction converters," in *Proc. IEEE Int. Symp. Industrial Electronics ISIE 2002*, vol. 3, 2002, pp. 731–736.

[96] A. Prodic, J. Chen, R. W. Erickson, and D. Maksimovic, "Digitally controlled low-harmonic rectifier having fast dynamic responses," in *Proc. Seventeenth Annual IEEE Applied Power Electronics Conf. and Exposition APEC 2002*, vol. 1, 2002, pp. 476–482.

[97] https://www.psoklahoma.com/info/news/reactivepowercharge.aspx. [Online]. Available: https://www.psoklahoma.com/info/news/ReactivePowerCharge.aspx

[98] C. Muscas, L. Peretto, S. Sulis, and R. Tinarelli, "Investigation on multipoint measurement techniques for pq monitoring," *IEEE Trans. Instrum. Meas.*, vol. 55, no. 5, pp. 1684–1690, 2006.

[99] E. J. Davis, A. E. Emanuel, and D. J. Pileggi, "Harmonic pollution metering: theoretical considerations," *IEEE Trans. Power Del.*, vol. 15, no. 1, pp. 19–23, 2000.

[100] P. H. Swart, J. D. van Wyk, and M. J. Case, "On techniques for localization of sources producing distortion in three-phase networks," *European Transactions on Electrical Power*, vol. 6, pp. 391–396, 1996.

[101] W. A. Omran, H. S. K. El-Goharey, M. Kazerani, and M. M. A. Salama, "Identification and measurement of harmonic pollution for radial and nonradial systems," *IEEE Trans. Power Del.*, vol. 24, no. 3, pp. 1642–1650, 2009.

[102] T. Tanaka and H. Akagi, "A new method of harmonic power detection based on the instantaneous active power in three-phase circuits," *IEEE Trans. Power Del.*, vol. 10, no. 4, pp. 1737–1742, 1995.

[103] W. Xu, X. Liu, and Y. Liu, "An investigation on the validity of power-direction method for harmonic source determination," *IEEE Trans. Power Del.*, vol. 18, no. 1, pp. 214–219, 2003.

[104] A. Cataliotti and V. Cosentino, "A new measurement method for the detection of harmonic sources in power systems based on the approach of the ieee std. 1459–2000," *IEEE Trans. Power Del.*, vol. 25, no. 1, pp. 332–340, 2010.

[105] C. Li, W. Xu, and T. Tayjasanant, "A "critical impedance"-based method for identifying harmonic sources," *IEEE Trans. Power Del.*, vol. 19, no. 2, pp. 671–678, Apr. 2004.

APPENDIX A: IMPEDANCE MEASUREMENT SYSTEM

A.1. Simulation Model for Impedance Measurement

A simulation model of in MATLAB/SIMULINK has been considered for the evaluation of the performance of the proposed estimation method, taking into account a complete circuit model which emulates the physical system available in the laboratory. The model consists of a 2 pole pairs single phase induction machine 1/4Hp in the type of Capacitor start - Capacitor run connected to grid. To simulate the current disturbances generated by the induction machine, a sinusoidal varying load is applied to the machine as described in the Chapter 3. A isolation transformer operating in the saturation mode to generate 3rd, 5th, 7th, ... harmonics as observed in the practical voltage and current at the PCC. Quantizers with step of 10ms are used for simulating of the ADC converters. Figure A.1 shows a simulink diagram.
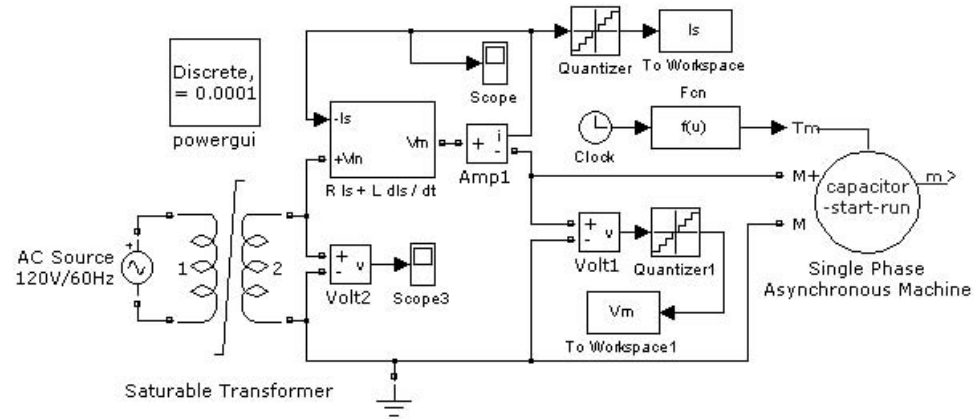
Figure A.1: Simulation model for impedance measurement system.

A.2. Laboratory Measurement Setup

The controlled-test for impedance measurement system was constructed in labratory with the same configuration as using in simulation. Figure A.2 represents this measurement

system. A power function generator Agilent 6813B supplies 120VAC to an induction machine Dayton 6K438BA 1/4Hp. The function generator provides abilities of programmable output impedance and programmable output voltage harmonics. Isotation transformer Stancor GIS-1000 115V/115V connects the induction machine and the the power function generator. A variable power transistor and inductor are also used in the controlled-test phase. Source impedance thus accounts for impedance of wire, transistor, inductor, transformer and programmable output impedance from the power suply. In controlled-test, this impedance is measured by a high accurate Ohm-meter. LEM sensors LV-20P and LA-55P collect voltage and current at the induction machine terminals. A 16 bits ADC converter ECON DT9816 sampled at 10kHz is used to convert these voltage and current signal and transfer to a PC. In the figure, R_c and R_v are the measurement resistors.
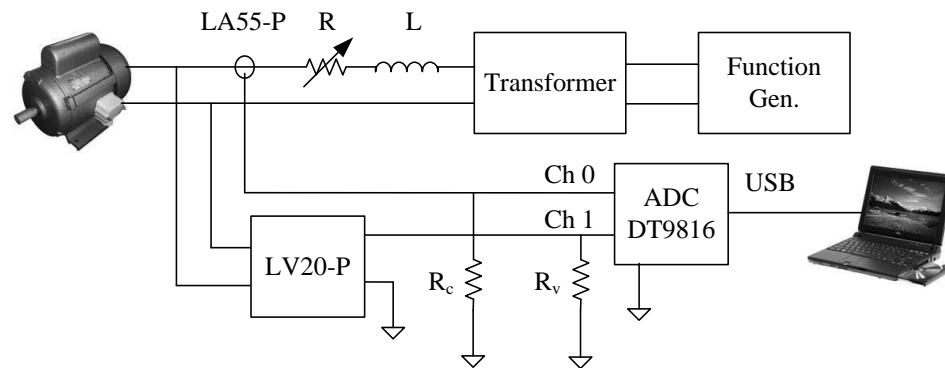
Figure A.2: Impedance measurement system in laboratory.

A.3. MATLAB Code for Grid Impedence Estimation

This section contains the variety of code needed to estimate the grid impedence.

```
% ===========================================================
% Grid Impedance Estimation Program
% Created by: Viet-Phong Tran
% Last edited: 2010 February, 12
% @Copyright@ reserved
```

```matlab
%=======================================================

function GridEstimation(filename)
x = load(filename);        % v-i
volt = x(:,1);
curr = x(:,2);
        Rm_v = 820;
        R_line = 33000;
        Rm_i = 2000;
        sf = 1000;
        u0 = rescale_v_data(volt, Rm_v, R_line);
        i0 = rescale_i_data(curr, Rm_i, sf);


%===================== Variables =====================
fs = 10000;
L = 30000;
if90 = 210.0;


for n = 0:25
    M90 = round(1/mean(if90)*fs*n*90+0.5);
    L90 = round(1/mean(if90)*fs*360);
    t90 = (0:1:L90)*1/fs;
        [i90(n+1), if90(n+1), ip90(n+1)] = ↘
        →FFT_iMag_iFreq_iPhase_Search(t90, 90.0, i0(M90 : 1↘
        →  : M90+L90));
        vc90(n+1) = Voltage_Correlation(t90, if90(n+1), ↘
        →ip90(n+1), u0(M90 : 1 : M90+L90));
```

```
                vs90(n+1) = Voltage_Correlation_Quadrature(t90, ↘
            →if90(n+1), ip90(n+1), u0(M90 : 1 : M90+L90));
                r90(n+1) = vs90(n+1)/i90(n+1);
                x90(n+1) = vc90(n+1)/i90(n+1);
            l90(n+1) = x90(n+1)/(2*pi*if90(n+1));

    end


R = mean(r90)
L = mean(l90)


clear all;


function [mag, freq, phase] = FFT_iMag_iFreq_iPhase_Search(↘
    →t, f_init, Data)
        [mag, freq, phase] = fine_search(t, Data, f_init);


function [mag, freq, phase] = fine_search(t, Ysearch, ↘
    →f_init)
f_midle = f_init;
for j = 1:5
    for i = -10:10
        f = f_midle + i*(0.1)^(j);
        iref_cos = 2*cos(2*pi*f*t);
        corr_cos = iref_cos'.*Ysearch;
        yn_cos = 2*corr_cos;
        aver_yn_cos = mean(yn_cos);
        iref_sin = 2*sin(2*pi*f*t);
```

```
        corr_sin = iref_sin '.* Ysearch;

        yn_sin = 2*corr_sin;

        aver_yn_sin = mean(yn_sin);

        q(i+11) = (aver_yn_cos^2 + aver_yn_sin^2);

    end

        [out, indx1] = max(q);  % search for maximum of q, ↘
        →return index of max(q)

        k = indx1 -11;             % true value of i

        f_midle = f_midle + k*(0.1)^(j);

end

        freq = f_midle;

        mag = sqrt(out);

        phase = atan(aver_yn_cos/aver_yn_sin);


function [vmag, vfreq, vphase] = FFT_vMag_vFreq_vPhase(t, ↘
→freq, voltage)

vs = 2*sin(2*pi*freq*t);

vcors = vs'.*voltage;

ycors = 2*vcors;

vsin = mean(ycors);

vc = 2*cos(2*pi*freq*t);

vcorc = vc'.*voltage;

ycorc = 2*vcorc;

vcos = mean(ycorc);

vphase = atan(vcos/vsin);

vmag = sqrt(vcos^2+vsin^2);

vfreq = freq;
```

```matlab
function vcos = Voltage_Correlation(t, freq, phase, voltage)
vref = 2*cos(2*pi*freq*t + phase);
vcor = vref'.*voltage;
ycor = 2*vcor;
vcos = mean(ycor);


function vsin = Voltage_Correlation_Quadrature(t, freq, phase, voltage)
vref = 2*sin(2*pi*freq*t + phase);
vcor = vref'.*voltage;
ycor = 2*vcor;
vsin = mean(ycor);
```

A.4. MATLAB Code to Rescale Current Data

```matlab
function iout = rescaleidata(iin, Rm, sf)
iout = iin/(Rm*(1/sf));    % This is the RMS value of the current
```

A.5. MATLAB Code to Rescale Voltage Data

```matlab
function vout = rescalevdata(vin, Rm, R_line)
vout = vin/Rm*(1/2.5)*R_line;    % This is the RMS value of the current
```

APPENDIX B: PROTOTYPE OF THE ADAPTIVE PFC CONVERTER

B.1. Simulation of Adaptive Control PFC Converter

The stability analysis is done first on MATLAB. Gain Margin, Phase Margin are received by Nyquist or Bode plot. This section shows the code to test the feasibility of the proposed adaptive control method.

```
function Stability_Analysis_Full
clear all


syms s Kv Tv Kcs C R L Dp Io Vo Fm Vc kso hso Po Ug wn Qn ↘
→Ts Tk k Tfi Tfv;


Gci = Kcs*Kv*(1+1/(Tv*s));


Gvi = (R*C*s+1)/(R*L*C*s^2 + L*s + R*Dp^2);
Gdi = Vo*(R*C*s+2)/(R*L*C*s^2 + L*s + R*Dp^2);
He = 1 + s/(Qn*wn) + s^2/wn^2;
GZOH = 1/(1+s*Ts/2);
eTsk = (12-6*s*Tk+(s*Tk)^2)/(12+6*s*Tk+(s*Tk)^2);
Hfi = 1/(Tfi*s + 1);
Hfv = 1/(Tfv*s + 1);


hs = hso*Hfi;
ks = kso*Hfv;
Ti = hs*Gci*Fm*Gdi*GZOH*k*eTsk;
```

```
Yin = Gvi/(1+Ti) + (ks/hs)*Vc*Ti/(1+Ti)
%
% =========================================================
clear all

global s Kv Tv Kcs C R L Dp Io Vo Fm Vc kso hso Po Ug wn Qn↘
→ Ts Tk k Tfi Tfv ;

Vo = 380;
Io = 0.9048;
Po = Vo*Io ;
R = 420;
L = 1.2e−3;
C = 1e−3;

hso = 1/9.6;
Fm = 1;
kso = 1/200;
Tfi = 1.232e−6;
Tfv = 5.6e−6;
k = 0.851;
fs = 40e+3;
Ts = 1/fs ;
Tk = 0.45*Ts ;  %calculation + photoisolation
Qn = −2/pi ;
wn = pi/Ts ;
```

```
Ug  =  120;
Ls  =  0.45e-3;
Rs  =  1.0;


Cs  =  3.22e-6;
Rc  =  470e+3;


Kv  =  0.45;
Tv  =  409.45e-6;
Kcs  =  1;


Vc  =  (hso/kso)*Po/Ug^2;
Ugt  =  115;
Dp  =  Ugt/Vo;


s  =  tf('s');


Yin  =  Tmx(Ug,  Kcs);


Zin  =  1/Yin;


Zs  =  Rc*(Ls*s+Rs)/(Rc*Ls*Cs*s^2  +  (Ls+Rs*Rc*Cs)*s  +  Rs  +  Rc↘
→);
Tm  =  Yin*Zs;


%=======================================================
Ug  =  90;
```

```
Kcs = 1;
Yin = Tmx(Ug, Kcs);


Ls = 0.45e-3;
Rs = 1.0;
Zs2 = Rc*(Ls*s+Rs)/(Rc*Ls*Cs*s^2 + (Ls+Rs*Rc*Cs)*s + Rs + ↘
→Rc);


Tm2 = Yin*Zs2;


% ==========================================================


Ug = 90;
Kcs = 1;
Yin = Tmx(Ug, Kcs);


Ls = 0.25e-3;
Rs = 0.25;
Zs3 = Rc*(Ls*s+Rs)/(Rc*Ls*Cs*s^2 + (Ls+Rs*Rc*Cs)*s + Rs + ↘
→Rc);


Tm3 = Yin*Zs3;


% ==========================================================
Ug = 90;
Kcs = 1;
Yin = Tmx(Ug, Kcs);
```

```
Ls = 0.65e-3;
Rs = 3.0;
Zs4 = Rc*(Ls*s+Rs)/(Rc*Ls*Cs*s^2 + (Ls+Rs*Rc*Cs)*s + Rs + ↘
→Rc);


Tm4 = Yin*Zs4;


%%%%%%%%%%%%%%%%%%%%%%%%%%%%%%%%%%%%%%%%%%%%%


p = bodeoptions;
p.MagUnits = 'dB';
p.FreqUnits ='Hz';
p.grid = 'on';
p.XLimMode = {'Manual'};
p.xlim = {[2e+3 1e+4]};


h2 = figure(2);
hold on
bodeplot(Tm, '-+k',Tm2, '-.k',Tm3, '-*k',Tm4, '-ok', p);


[Gm, Pm, Wg, Wp] = margin(Tm);
Phase1 = Pm
fci = Kv*1/9.6*380/(2*pi*1.2e-3)


[Gm, Pm, Wg, Wp] = margin(Tm2);
```

```
Phase2 = Pm


[Gm, Pm, Wg, Wp] = margin(Tm3);
Phase3 = Pm


[Gm, Pm, Wg, Wp] = margin(Tm4);
Phase4 = Pm



%=====================================================


Ug = 95;
Kcs = 1;
Yin = Tmx(Ug, Kcs);


Ls = 0.25e−3;
Rs = 0.45;
Zs3 = Rc*(Ls*s+Rs)/(Rc*Ls*Cs*s^2 + (Ls+Rs*Rc*Cs)*s + Rs + ↘
→Rc);
Tm3 = Yin*Zs3;


Kcs = 0.75;
Yin = Tmx(Ug, Kcs);
Tm31 = Yin*Zs3;


Kcs = 0.5;
Yin = Tmx(Ug, Kcs);
Tm32 = Yin*Zs3;
```

```
Kcs = 0.2;
Yin = Tmx(Ug, Kcs);
Tm33 = Yin*Zs3;
fci = Kcs*Kv*1/9.6*380/(2*pi*1.2e-3)


h2 = figure(3);
hold on
bodeplot(Tm3,'-y',Tm33, '-k', p);


[Gm, Pm, Wg, Wp] = margin(Tm3);
Phase3 = Pm
fci = Kv*1/9.6*380/(2*pi*1.2e-3)


[Gm, Pm, Wg, Wp] = margin(Tm31);
Phase31 = Pm


[Gm, Pm, Wg, Wp] = margin(Tm32);
Phase32 = Pm


[Gm, Pm, Wg, Wp] = margin(Tm33);
Phase33 = Pm



function out = Tmx(Ug, Kcs)
global s Kv Tv C R L Dp Vo Fm Vc kso hso Po Ts Tk k Tfi Tfv↘
→;
```

```
Vc = ( hso / kso ) ∗Po /Ug^2 ;
out = (R∗C∗s +1) /(R∗L∗C∗s^2+L∗s+R∗Dp^2) /(1+ hso /( Tfi ∗s +1) ∗Kcs↘
→∗Kv ∗(1+1/Tv/ s ) ∗Fm∗Vo ∗(R∗C∗s +2) /(R∗L∗C∗s^2+L∗s+R∗Dp^2)↘
→/(1+1/2∗ s ∗Ts ) ∗k ∗(12 −6∗ s ∗Tk+s^2∗Tk^2) /(12+6∗ s ∗Tk+s^2∗Tk^2) )↘
→+kso /( Tfv ∗s +1) ∗Vc∗Kcs∗Kv ∗(1+1/Tv/ s ) ∗Fm∗Vo ∗(R∗C∗s +2) /(R∗L∗C↘
→∗ s^2+L∗s+R∗Dp^2) /(1+1/2∗ s ∗Ts ) ∗k ∗(12 −6∗ s ∗Tk+s^2∗Tk^2)↘
→/(12+6∗ s ∗Tk+s^2∗Tk^2) /(1+ hso /( Tfi ∗s +1) ∗Kcs∗Kv ∗(1+1/Tv/ s ) ∗↘
→Fm∗Vo ∗(R∗C∗s +2) /(R∗L∗C∗s^2+L∗s+R∗Dp^2) /(1+1/2∗ s ∗Ts ) ∗k↘
→∗(12 −6∗ s ∗Tk+s^2∗Tk^2) /(12+6∗ s ∗Tk+s^2∗Tk^2) ) ;
```

B.2. Laboratory Measurement Setup

The PFC converter was constructed with the parameters shown in the Chapter 4. The schematic for PFC converter is shown in the Figure B.1. The components were placed on the printed circuit board (PCB). The controller features the dsPIC30F6010A chip, which is manufactured by Microchip. The boost rectifier circuit on the prototype PCB uses the topology and control strategy described in Chapter 4.

Figure B.1: Schematic of PFC converter.

B.3. Controller Code for PFC Converter

This section lists the code for control of PFC converter and the adaptive control.

B.4. PFC Project Main Code

```
// ************************************************ //

// Header files //

#include "General.h"


volatile unsigned int SampleCountMin = 300; // Mininum of ↘
→ frequency count SampleCount = 334 if f = 60 Hz
volatile unsigned int SampleCount = 333; // Initialize ↘
→ sample count
volatile unsigned int AverageVacMinimum = 0x1DCF; // Minimum ↘
→ value for ~100 Vpk: (2/ pi) *100 Vpk /410 Vpk *32767
volatile unsigned int AverageVac = 0x517C; // Initialize ↘
→ average Vac and Vpeak (0 x7FFF ) for start up


// ************************************************ //

// Main Function //

int main (void)
{
```

```
SetupPorts(); // Initialize all the GPIO ports
SetupBoard(); // Configure the board for Reset Condition
InitOutputCompare6(); // Configure and intialize the ↘
→ Output Compare Module
configADC(); // Configure the ADC Module


IFS0bits.ADIF = 0; // Clear ADC Interrupt Flag
IEC0bits.ADIE = 1; // Enable ADC Interrupts
OC6CONbits.OCM = 0b110; // Set the Output Compare Module↘
→  for PWM Mode
T3CONbits.TON = 1; // Start Timer-3 Module


while(1); // Loop Infinitely

}



// ***********************************************************//


// ADC Interrupt Service Routine //


// All Data are collected within 2 timer periods , after 2 ↘
→ timer periods , _ADCInterupt occurs.


void __attribute__((__interrupt__ , auto_psv)) ↘
→_ADCInterrupt(void)
```

```
{

        IFS0bits.ADIF = 0; // Clear ADC Interrupt Flag

        VoltagePIControl(); // Voltage Error Compensator

        calcIacRef(); // Calculation of Current Reference

        CurrentPIControl(); // Current Error Compensator

        pinLED1 = 1;

}


// **********************************************************//

// Setup the HV Power Module for Reset State

void SetupBoard(void)

{
    unsigned char b;
    IEC0bits.ADIE = 0; // Clear ADC Interrupt Flag
    pinFaultReset = 1; // Reset all fault states to default
    for(b=0;b<10;b++)
        Nop();
    pinFaultReset = 0; // Activate all faults
```

```
        pinPFCFire = 0; // Disable PFC MOSFET gate pulses
        pinBrakeFire = 0; // Disable Brake Chopper MOSFET gate ↘
        → pulses
}


// ************************************************************//


// Configure the A to D Converter


void configADC(void)


{


    ADCON1 = 0;
    ADCON1bits.FORM = 3; // Signed Fractional Results
    ADCON1bits.SSRC = 2; // GP Timer −3 to trigger ADC
    ADCON1bits.SIMSAM = 1; // Simultaneous Sampling enabled
    ADCON1bits.ASAM = 1; // Auto Sampling enabled


    ADCON2 = 0;
    ADCON2bits.CHPS = 3; // Convert CH0, CH1, CH2 and CH3
    ADCON2bits.SMPI = 1; // Interrupt on second sample /↘
    → convert sequence
    ADCON2bits.CSCNA = 1; // Channel Scanning enabled


    ADCON3bits.SAMC = 8; // Auto − Sample time = 8 ∗ Tad
    ADCON3bits.ADCS = 8; // AD Conversion time = 8 ∗ Tcy
```

```
ADCHS = 0;
ADCHSbits.CH123NA = 0; // Channels CH1, CH2 and CH3 ↘
    → negative reference is Vref−
ADCHSbits.CH0NA = 0; // Channel CH0 negative reference ↘
    → is Vref−
ADCHSbits.CH123SA = 0; // Convert AN0, AN1 and AN2


ADPCFG = 0xFFFF;
ADPCFGbits.PCFG2 = 0; // AN2(AN6) pin in analog mode
ADPCFGbits.PCFG9 = 0; // AN9  pin in analog mode
ADPCFGbits.PCFG11 = 0; // AN11  pin in analog mode


ADCSSL = 0;
ADCSSLbits.CSSL9 = 1; // Select AN9 for input scanning
ADCSSLbits.CSSL11 = 1; // Select AN11 for input scanning


ADCON1bits.ADON = 1; // Turn−ON the ADC Module


}


// ****************************************************//


// Configure the Output Compare 6 Module


; Output Compare 6 and Timer 3 Configuration
; OC6 configured for PWM mode
```

```
; Timer 3 used as counter
; PWM Period = (PRx + 1)*Tcy*(TMRx Prescaler)
; PWM Period = (PR3 + 1)*33ns*(1:1)
; OCxRS Updates PWM Duty Cycle
; PRx gives PWM period
; For a PWM frequency of 80KHz, set PRx = d#368


void InitOutputCompare6(void)
{

        OC6CON = 0; // Clear the config register
        OC6RS = 0; // Clear the initial duty cycle register
        OC6R = 0; // Clear the duty cycle register


        OC6CON = 0x0009; // Set the operating mode for the ↘
        →output compare module
        PR3 = 368; // Set the period value for the PWM ↘
        →pulses


        IFS0bits.T3IF = 0; // Clear the timer3 interrupt ↘
        →flag
        IFS2bits.OC6IF = 0; // Clear the OC6 interrupt flag


        IEC0bits.T3IE = 0; // Disable timer3 interrupt
        IEC2bits.OC6IE = 0; // Disable OC6 interrupt
```

```
}


// ************************************************************//


// T3 Interrupt Service Routine //


void __attribute__((__interrupt__ , auto_psv)) _T3Interrupt↘
→(void)
{


IFS0bits.T3IF = 0;// Clear timer3 interrupt flag


}


// ************************************************************//


// OC6 Interrupt Service Routine //


void __attribute__((__interrupt__ , auto_psv)) ↘
→_OC6Interrupt(void)
{


IFS2bits.OC6IF = 0;// Clear OC6 interrupt flag


}
```

```
//**************************************************//

//    Math  Error  Trap  ISR

void __attribute__((__interrupt__ , auto_psv)) _MathError(
    void)
{
    //    INTCON1bits.MATHERR = 0;
    while(1);
}



//**************************************************//

//    Address  Error  Trap  ISR

void __attribute__((__interrupt__ , auto_psv))
    _AddressError(void)

{
    //    INTCON1bits.ADDRERR = 0;
    while(1);
}



//**************************************************//

//    Stack  Error  Trap  ISR
```

```c
void __attribute__(( __interrupt__ , auto_psv)) _StackError(
→void)

{
    //    INTCON1bits.STKERR = 0;
    while(1);
}
```

```
// *******************************************************//
```

B.5. PFC Code

```
.include "general.inc"
.include "PI.inc"


; =========================================================
; Define bit values
.equiv flag1 , 0x0000
.equiv flag2 , 0x0001
.equiv flag3 , 0x0002 ; SoftStart
.equiv flag4 , 0x0003 ; switch current reading buffer (BUF7,
→ BUF3)
.equiv flag6 , 0x0005
.equiv flag7 , 0x0006


; =========================================================
; Declare Initialized local variables
```

```
        .data
flag:                           .word    0x0067   ;  0x0000  0000  0110 ↘
→0111
```

```
;  ==========================================================
;  Declare  Non  Initialized  local  variables
```

```
        .bss
VacByVpk:           .space 2
IacRef:             .space 2
Iac:                .space 2
Vdc:                .space 2
Ein:                .space 2
Evn:                .space 2
U0inH:              .space 2
U0inL:              .space 2
U0vnH:              .space 2
U0vnL:              .space 2
Usin:               .space 2
Uin:                .space 2
Usvn:               .space 2
Uvn:                .space 2
IPIH:               .space 2
TempSampleCount:    .space 2
TempSumVac:         .space 4
VdcSoftStart:       .space 2
```

```
VpiCount :            . space  2
ucn :                 . space  2
ucn1 :                . space  2
ucn2 :                . space  2
uks :                 . space  2
Iac1 :                . space  2
```

```
;  ========================================================
;  Declare  globals
. global          VacByVpk
. global          IacRef
. global          Iac
. global          Vdc
. global          Ein
. global          Evn
. global          U0inH
. global          U0inL
. global          U0vnH
. global          U0vnL
. global          Usin
. global          Uin
. global          Usvn
. global          Uvn
. global          VdcSoftStart
. global          VpiCount
. global          ucn
```

```
        .global              ucn1
        .global              ucn2
        .global              uks
        .global              Iac1


; ========================================================
; Declare constants
.equ AdcConvFactor,      0x8000 ; Factor for scaling the ADC↘
→ Results
.equ Kpi,                16383 ; Kp for current compensator
.equ Kii,                3476 ;  Ki for current compensator
.equ Kci,                4119 ;  Kc for current compensator
.equ Kpv,                32766 ; Kp for voltage compensator
.equ Kiv,                4 ; Ki for voltage compensator
.equ Uimax,              27850 ; after scaling by 100, ↘
→maximum output is pfcMaxDuty = 275 ~ 83%
.equ Uimin,              800 ; for Turn−off snubber
.equ pfcMaxDuty,         278 ; for Turn−on snubber
.equ VdcRef,             30369 ; 380V output reference
.equ NKio,               0
.equ NKvo,               0
.equ Nio,                1 ; Current scale to get maximum ↘
→ADC range
.equ DutyScalingFactor,  100
.equ PIby4,              0x6487 ; pi/4 will be scaled by 2 ↘
→for peak Vac
```

```
.equ voltMinRef,         0x2000 ; Corresponds to ~25V input
→reference = 25/410Vpk*32767

.equ VrefIncTime,        10000

.equ VRefIncrement,      0xFF

.equ VdcScale,           31250 ; KH = 0.946 Compensate for
→Vdc offset

.equ c1,                 25917 ; Ls = 7.5mH; Ls = 4.5mH

.equ c2,                 12862 ;

.equ c3,                 2420 ;

.equ c4,                 2384 ;


; ==========================================================
; Declare references to registers


.equ PfcPwm, OC6RS ; Output Compare Duty Cycle


; ==========================================================
.section   .text



; ==========================================================
; Calculate IacRef
; IacRef = (VPI * |Vac| / Vpk)


.global    _calcIacRef
.global    calcIacRef
```

```
_calcIacRef:
calcIacRef:


push.d w0
push.d w2
push.d w4



; Calculate Vac peak from measurement
                call      calcVavg
                mov.w     _AverageVac, w4


                mov.w     #PIby4, w5
                mpy                 w4*w5, A
                sftac     A, #−1
                sac.r     A, w3 ; w3 = Vpeak


; Set default is 5V or 0x7FFF for 110VRms AC input
                ;mov.w   #0x6BFF, w3 ; 160V
                ;mov.w   #0x67FF, w3 ; 154V


; Get the Vac in signed Q15 format: 0x8000 − 0x7FFF
                mov.w     ADCBUF0, w0
                mov.w     #AdcConvFactor, w1 ; covert it to ↘
                →the unsigned Q15 format: 0x0000 − 0x7FFF
                xor       w0, w1, w0
```

```
                              lsr        w0, #1, w4



; Calculate Vac/Vpk,
                              cp         w3, w4
                              bra        LE, IacRefLimit
                              bra         IacRefNormal
IacRefLimit:
                              ;mov.w    w3, w4
                              ;sub.w    w4, #0x02
                              mov.w     #0x7FFF, w0
                              bra         IacRefContinue
IacRefNormal:

                              repeat   #17
                              divf     w4, w3   ; signed fractional ↘
                              →division w0/w3, the result should be 0↘
                              →x0000 − 0x7FFF



IacRefContinue:
; (Vac/Vpk)∗Vpih, signed fractional multiplication
                              mov.w     w0, w4
                              mov.w     Uvn, w5
                              mpy       w4∗w5, A
                              sac.r    A, w0



; If SoftStart then jump to IacRefContinue
                              btsc      flag, #flag3
                              bra        IacRefOutput
```

```
; Else calculate IacrefCompensator

                        mov.w    w0, uks

                        call     CalDutyComp

                        mov.w    ucn, w1

                        mov.w    uks, w0

                        add.w    w0, w1, w0


IacRefOutput:

                        mov.w    w0, IacRef



pop.d w4

pop.d w2

pop.d w0


return




; ==========================================================

; Current loop PI Controller


.global   _CurrentPIControl

.global   CurrentPIControl


_CurrentPIControl:
```

```
CurrentPIControl :


push.d w0

push.d w2

push.d w4

push.d w6


; Measured value of Rectified AC Current
; ADC input from 0:5V, equivalent Iac = −9.6A:9.6A (LEM ↘
→sensor), SCALED ADC buffer is 0x8000:0x7FFF
                    btss      flag, #flag4

                    bra       first_period

                    mov.w    ADCBUF7, w0

                    bra       continue_reading
first_period :
                    mov.w    ADCBUF3, w0
continue_reading :
                    btg.b     flag, #flag4

                    mov.w    w0, Iac

                    nop


; Init PI
; If start program then reset current output and sum
                    btss      flag, #flag6

                    bra       IPI_Cal

                    clr       w1

                    mov.w    w1, U0inH
```

```
            mov.w    w1, U0inL

            mov.w    w1, Uin

            mov.w    w1, Ein

            mov.w    w1, ucn

            mov.w    w1, ucn1

            mov.w    w1, ucn2

            mov.w    w1, Iac1

            bclr     flag, #flag6


; Current PI Calculation
IPI_Cal:


        ; Recall Previous error, e(n-1) = old Ein
            mov.w    Ein, w0


    ; Calculate new error e(n) = InRef-InMeas
            mov.w    Iac, w5
            ; sl      w5, #Nio, w5 ; LTS 6NP range is ⬂
            →[-9.6, 9.6] ~ [-1, 1].
            mov.w    IacRef, w7 ; Iin max = 2*P0/Vmin = ⬂
            →2*400/170 = 4.7A ~ [-0.5, 0.5]. So for ⬂
            →full scale, multiply 2
            ; sl      w7, #Nio, w7 ; scale IacRef. See ⬂
            →PSIM

            sub.w    w7, w5, w4
            mov.w    w4, Ein   ; e(n) = Ein
```

```
; Calculate Differential Error: dEin = e(n) − e(n↘
→−1)
        sub.w    w4, w0, w6


; Load previous control u0(n−1) [−1, 1]
        mov.w    U0inH, w0
        lac              w0, B
        mov.w    U0inL, w1
        mov.w    w1, ACCBL


; Add u0(n−1) + dEin * Kp*2^NKio
        mov.w    #Kpi, w5
        ;lsr      w5, #Nio, w5 ; scale by 0.5 to ↘
        →compensate to Iac and Iref
        mpy      w5*w6, A
        sftac    A, #−NKio ; scale A if nessecery (↘
        →Q12−>Q15),       A = A*2^NKio


; Add u0i(n−1) + dEin*Kp
        add              A


; u0(n) = u0(n−1) + Kp*(e(n)−e(n−1)) + Ki * e(n)
        mov.w    #Kii, w5
        mac      w4*w5, A


sac              A, w6
```

```
                mov.w    w6, Usin ; store u0(n) before tests


        ; Compare u0(n) and Uimax
                mov.w    #Uimax, w0
                cp               w6, w0
                bra              GT, jPI5 ; u0(n) > Umax; u(↘
                →n) = Umax


                mov.w    #Uimin, w0
                cp               w6, w0
                bra              LE, jPI5 ; u0(n) < Umin; u(↘
                →n) = Umin


                mov.w    Usin, w0 ; u(n) = u0(n)
        jPI5:
                mov.w    w0, Uin ; u(n) = [Umax, u0(n), or ↘
                →Uin] This is the control output


        ; es(n) = u(n) − u0(n)
                sub.w    w0, w6, w4
                ;mov.w   w4, esin


        ; Adjust u0(n) = u0(n) + Kc ∗ es(n)
                mov.w    #Kci, w5
                mac              w4∗w5, A


        ; Store u0(n) for the next step
```

```
                sac                 A, w0

                mov.w    w0, U0inH

                mov.w    ACCAL, w0

                mov.w    w0, U0inL



    ; End of PI Calculation



    ; Output of IPI Controller

                mov.w    Uin, w0



    ; Scaling IPIH to match the duty cycle from [800, 32000] to↘
    → fit in PWM setting range [0, 368]

                mov.w    w0, w2

                mov.w    #DutyScalingFactor, w3

                repeat   #17

                div.u    w2, w3

                mov.w    w0, IPIH



    ; Compare IPI output to the Maximum Duty Cycle

                mov.w    #pfcMaxDuty, w1

                cp       w1, w0

                bra      LE, saturatePfc

                mov.w    IPIH, w0

                mov.w    w0, PfcPwm

                bra      goback



    saturatePfc:
```

```
                        mov.w  #pfcMaxDuty ,  w1

                        mov.w  w1 ,  PfcPwm




goback :


pop . d  w6

pop . d  w4

pop . d  w2

pop . d  w0




return




;  ========================================================

;  Compute  Duty  Ratio  Compesator


. global     _CalDutyComp

. global     CalDutyComp


_CalDutyComp :

CalDutyComp :


push . d  w0

push . d  w2

push . d  w4
```

```
; uc(n) = c1*uc(n−1) − c2*uc(n−2) + c3*i(n) − c4*i(n−1)


; uc(n) = c1*uc(n−1)
                mov.w     ucn1 , w4
                mov.w     #c1 , w5
                mpy       w4*w5 , A


; uc(n) = c1*uc(n−1) − c2*uc(n−2)
                mov.w     ucn2 , w4
                mov.w     #c2 , w5
                msc       w4*w5 , A


; uc(n) = c1*uc(n−1) − c2*uc(n−2) + c3*i(n)
                mov.w     Iac , w4
                mov.w     #c3 , w5
                mac       w4*w5 , A


; uc(n) = c1*uc(n−1) − c2*uc(n−2) + c3*i(n) − c4*i(n−1)
                mov.w     Iac1 , w4
                mov.w     #c4 , w5
                msc       w4*w5 , A


                sftac     A, #−1   ; coefficients by 2


                sac               A, w0
```

```
                    mov.w    w0, ucn


; store variables
                    mov.w    ucn1, w1
                    mov.w    w1, ucn2


                    mov.w    w0, ucn1


                    mov.w    Iac, w1
                    mov.w    w1, Iac1


pop.d w4
pop.d w2
pop.d w0


return




; ==========================================================
; Voltage loop PI Controller


.global    _VoltagePIControl
.global    VoltagePIControl


_VoltagePIControl:
VoltagePIControl:
```

```
        push.d  w0
        push.d  w2
        push.d  w4
        push.d  w6


; Measured value of DC Bus Voltage
                mov.w   ADCBUF4, w0
                mov.w   #AdcConvFactor, w1
                xor     w0, w1, w0
                lsr     w0, #1, w0


; Init PI
; If start program then: (1) reset current output and sum, ↘
→(2) load VdcReference, and (3) Load Delay
                btss    flag, #flag7
                bra     ContinueVPIControl
                clr     w1
                mov.w   w1, U0vnH
                mov.w   w1, U0vnL
                mov.w   w1, Uvn
                mov.w   w1, Evn
                mov.w   w0, VdcSoftStart
                mov.w   #VrefIncTime, w1
                mov.w   w1, VpiCount ; 50ms for each ↘
                →increment of VdcReference
                bclr    flag, #flag7
                bset    flag, #flag3
```

ContinueVPIControl :

; SoftStart calculation for raising the DC Bus Voltage ↘
→gradually upto the rated value of 400 volt

```
                mov.w    VdcSoftStart , w2
                mov.w    #VdcRef , w3
                cp       w2, w3
                bra      GE, VPI_Cal


                mov.w    VpiCount , w2
                cp       w2, #0x0000
                bra      GT, WaitCount ; if Less/Equal to ↘
                →Zero then SP = 340V ; else 380V
                bra      SoftStartVdc
WaitCount :
                dec      w2, w1
                mov.w    w1, VpiCount
                bra      VPI_Cal
SoftStartVdc :
                mov.w    #VrefIncTime , w1 ; Reset VpiCount
                mov.w    w1, VpiCount
                mov.w    VdcSoftStart , w1
                add      #VRefIncrement , w1 ; Increase ↘
                →VdcReference


                cp       w1, w3
```

```
                bra       GE,  VrefSteadyState
                mov.w     w1,  VdcSoftStart
                bra       VPI_Cal
VrefSteadyState:
                bclr      flag,  #flag3
                mov.w     w3,  VdcSoftStart


; Voltage PI Calculation
VPI_Cal:


                mov.w     #VdcScale,  w4 ;  calibrate  for  Vdc ↘
                →offset  to  have  380Vdc
                mov.w     w0,  w5
                mpy       w4*w5,  A
                sac.r     A,  w0



                mov.w     w0,  Vdc


        ; Recall  Previous  error ,  e(n−1) =  old  Ein
                mov.w     Evn,  w0


    ; Calculate  new  error  e(n) =  InRef−InMeas
                mov.w     Vdc,  w5
                mov.w      VdcSoftStart ,  w7


                sub.w     w7,  w5,  w4
                mov.w     w4,  Evn   ;  e(n) =  Evn
```

```
; Calculate Differential Error: dEvn = e(n) − e(n↘
→−1)
        sub.w    w4, w0, w6


; Load previous control u0(n−1) [0, 1]
        mov.w    U0vnH, w0
        lac              w0, B
        mov.w    U0vnL, w1
        mov.w    w1, ACCBL


; Add u0(n−1) + dEvn ∗ Kp∗2^NKvo
        mov.w    #Kpv, w5
        mpy      w5∗w6, A
        sftac    A, #−NKvo ; scale A if nessecery (↘
        →Q12−>Q15), A = A∗2^NKvo


; Add u0v(n−1) + dEvn∗Kp
        add      A


; u0(n) = u0(n−1) + Kp∗(e(n)−e(n−1)) + Ki ∗ e(n)
        mov.w    #Kiv, w5
        mac      w4∗w5, A


sac               A, w6
;sac.r  A, w6   w6 is added by 1, so U0vnH:U0vnL is↘
→ added 0x00010000, which is two much
```

```
                ; Store u0(n) for the next step
                        mov.w     w6, U0vnH
                        mov.w     ACCAL, w0
                        mov.w     w0, U0vnL


; End of PI Calculation


                ; Output of VPI Controller
                        mov.w     w6, Uvn


VPIback:


pop.d w6
pop.d w4
pop.d w2
pop.d w0



return



; ==========================================================
; Compute SUM(|Vac|) for 1 cycle, Frequency and Average Vac


.global   _calcVavg
.global   calcVavg
```

```
_calcVavg:
calcVavg:


push.d w0
push.d w2
push.d w4
push.d w6
push.d w8


; convert input Vac range
; Vac is collected in Q15 format (ACON1 = 0). Range: 0x8000↘
→(0V) : 0x7FC0 (5V) (see dsPIC30F Datasheet)
                mov.w    ADCBUF0, w0 ; Convert signed Q15 ↘
                →format to unsigned Q15 format for adding
                mov.w    #AdcConvFactor, w1 ; w0 range: 0↘
                →x0000(0V): 0x7FC0(5V)
                xor      w0, w1, w0
                lsr      w0, #1, w0


; Check Vac if it is bellow a threshold for calculating ↘
→start counting point
                mov.w    #voltMinRef, w2
                cp       w0, w2
                bra      N, tempsum ; if so, jump to tempsum↘
                →  to calculate lower part
```

```
; else if Vac > VREF
; Check status of flag1 and flag2 for clear condition
                btss      flag, #flag1 ; if flag[0] = 1, jump↘
                → to the case2
                btsc      flag, #flag2 ; else if flag[1] = 0,↘
                → go to the case1, update SampleCount and ↘
                →SumVac
                bra       case2


; Update if both flag1 and flag2 are clear
case1:
                mov.w     TempSampleCount, w4 ; Update ↘
                →SampleCount


; Check if SampleCount is smaller than threshold to avoid ↘
→divide by 0, this case is error counting
                mov.w     _SampleCountMin, w1
                cp        w4, w1
                bra       N, SaturateMinCount ; if so, set ↘
                →SampleCount = SampleCountMin
                bra       continueSumVac ; otherwise, keep ↘
                →going


SaturateMinCount:
                mov.w     _SampleCountMin, w4


continueSumVac:
```

```
                    mov.w    w4, _SampleCount


                    mov      #TempSumVac, w1
                    mov.d    [w1], w2 ; w2 = TempSumVac_L, w3 = ↘
→TempSumVac_H


                    repeat  #17
                    div.ud  w2, w4 ; w0 is AverageVacTemp


; Check if AverageVacTemp is smaller than threshold to ↘
→avoid divide by zero
                    mov.w    _AverageVacMinimum, w1
                    cp       w0, w1
                    bra      N, SaturateMinVavg ; if so, jump to↘
→ SaturateMinVavg
                    bra      continueLoop ; else keep going


SaturateMinVavg:
                    mov.w    _AverageVacMinimum, w0


continueLoop:
                    mov      w0, _AverageVac


; flag[0] = 1, flag[1] = 1
                    bset     flag, #flag1
                    bset     flag, #flag2
```

```
; TempSampleCount = 0
                    clr      w2
                    clr      w3
                    mov.w    w2, TempSampleCount


; TempSumVac = 0
                    mov.w    #TempSumVac, w4
                    mov.d    w2, [w4]


                    bra      outofloop


case2:
; Vac is collected in Q15 format (ACON1 = 0). Range: 0x8000↘
→(0V) : 0x7FC0 (5V) (see dsPIC30F Datasheet)
                    mov.w    ADCBUF0, w0
                    mov.w    #AdcConvFactor, w1
                    xor      w0, w1, w0
                    lsr      w0, #1, w0


; TempSumVac = TempSumVac + Vac
                    mov.w    w0, w8


                    mov      #TempSumVac, w0 ; TempSumpVac
                    mov.d    [w0], w2


                    add      w8, w2, w2 ; TempSumpVac + Vac
                    addc     #0, w3
```

```
                mov.w    #TempSumVac, w4 ; move address of
                →TempSumVac to register w4
                mov.d    w2, [w4] ; move content of register
                → w2 to the address of content of w4, which
                → is address of TempSumVac
```

```
; Increase SampleCount to 1
                mov.w    TempSampleCount, w6
                inc      w6, w6
                mov.w    w6, TempSampleCount
```

```
; flag[0] = 0
                bclr     flag, #flag1


                bra      outofloop
```

```
tempsum:
                btsc     flag, #flag1 ; if flag[0] = 1 then
                →exit
                bra      outofloop


                mov.w    ADCBUF0, w0
                mov.w    #AdcConvFactor, w1
                xor      w0, w1, w0 ; Convert signed Q15
                →format to unsigned Q15 format for adding
```

```
              lsr      w0, #1, w0 ; w0 range: 0x0000(0V): ↘
              →0x7FC0(5V)


; TempSumVac = TempSumVac + Vac
              mov.w    w0, w8


              mov      #TempSumVac, w0 ; TempSumpVac
              mov.d    [w0], w2


              add      w8, w2, w2
              addc     #0, w3


              mov.w    #TempSumVac, w4
              mov.d    w2, [w4]


; Increase SampleCount to 1
              mov.w    TempSampleCount, w6
              inc      w6, w6
              mov.w    w6, TempSampleCount


; flag[1] = 0
              bclr     flag, #flag2


outofloop:


pop.d w8
pop.d w6
```

```
pop.d w4

pop.d w2

pop.d w0


return
```

B.6. PI Code

```
; ===========================================================
; PI
;
; Description:   Calculate PI correction.
;
; ===========================================================
;
        .include "General.inc"


; External references
        .include "PI.inc"




; Register usage

        .equ BaseW0,    w0 ; Base of parm structure

        .equ OutW1,     w1 ; Output
```

```
        .equ  SumLW2,    w2 ; Integral sum
        .equ  SumHW3,    w3 ; Integral sum


        .equ  ErrW4,     w4 ; Error term: InRef-InMeas
        .equ  WorkW5,    w5 ; Working register
        .equ  UnlimitW6,w6 ; U: unlimited output
        .equ  WorkW7,    w7 ; Working register



;================== CODE ================================


        .section   .text


        .global    _InitPI
        .global    InitPI
_InitPI:
InitPI:
        mov.w      w1,[BaseW0+PI_qOut]
        return




        .global    _CalcPI
        .global    CalcPI


_CalcPI:
CalcPI:
    ;; Err  = InRef - InMeas
```

```
        mov.w          [BaseW0+PI_qInMeas],WorkW5

        mov.w          [BaseW0+PI_qInRef],WorkW7

        sub.w               WorkW7,WorkW5,ErrW4


;;  U  =  Sum  +  Kp * Err * 2^NKo

    lac            [++BaseW0],B  ;  AccB  =  Sum

    mov.w          [--BaseW0],WorkW5

    mov.w          WorkW5,ACCBLL


    mov.w          [BaseW0+PI_qKp],WorkW5

    mpy            ErrW4*WorkW5,A

    sftac          A,#-NKo  ;  AccA  =  Kp*Err*2^NKo

    add            A  ;  Sum  =  Sum  +  Kp*Err*2^NKo

    sac            A,UnlimitW6  ;  store  U  before  tests


    mov.w          [BaseW0+PI_qOutMax],OutW1

    cp             UnlimitW6,OutW1

    bra            GT,jPI5  ;  U > Outmax;  OutW1  =  Outmax


    mov.w          [BaseW0+PI_qOutMin],OutW1

    cp             UnlimitW6,OutW1

    bra            LE,jPI5  ;  U < Outmin;  OutW1  =  Outmin


    mov.w          UnlimitW6,OutW1  ;  OutW1  =  U

jPI5:

    mov.w          OutW1,[BaseW0+PI_qOut]
```

```
;; Ki * Err
    mov.w       [BaseW0+PI_qKi],WorkW5
    mpy         ErrW4*WorkW5,A
                ;mac        ErrW4*WorkW5,A


;; Exc = U - Out
    sub.w       UnlimitW6,OutW1,UnlimitW6


;; Ki * Err - Kc * Exc
    mov.w       [BaseW0+PI_qKc],WorkW5
    msc         WorkW5*UnlimitW6,A


;; Sum = Sum + Ki * Err - Kc * Exc
    add         A

    sac         A,[++BaseW0]  ; store Sum
    mov.w       ACCALL,WorkW5
    mov.w       WorkW5,[--BaseW0]
    return


.end
```